Effects of water absorption on the strain rate sensitive properties of glass fibre reinforced polymers

Gustavo Quino Quispe

Exeter College

University of Oxford

A thesis submitted for the degree of

Doctor of Philosophy

Hilary 2018

Effects of water absorption on the strain rate sensitive properties of glass fibre reinforced polymers

Gustavo Quino Quispe, Exeter College, University of Oxford
For the degree of D.Phil. in Engineering Science, Hilary 2018

The present thesis introduces, for the first time, a comprehensive numerical and experimental investigation of the combined effects of strain rate and water exposure on composite laminates and their constituents epoxy resin matrix and E-glass fibres. Long-term exposure to wet environments and the application of loads at various speeds are critical challenges for marine composites, as both strain rate and water absorption affect their mechanical behaviour. This thesis addresses the problem by investigating the influence of water absorption on the strain rate dependent behaviour of glass fibre reinforced polymers. Unlike previous studies focusing on the consequences of water on the properties of the composite or the resin matrix only, the strategy behind this investigation considers the experimental and numerical study of the effects of water on every constituent of the composite.

Specimens were immersed in water and salt-water baths at 50°C to accelerate water absorption, and subsequently tested at different strain rates. Experiments showed that all constituents and the composite are strain rate dependent regardless the water pre-conditioning. In addition, all tests suggested that wet environments have detrimental effects on the resin matrix, fibre bundles, and composite laminates. Water absorption affected their elastic modulus, tensile strength, short beam strength, and caused swelling of the matrix and damage to the matrix-fibre interface. Only E-glass single fibres were found to be indifferent to water pre-conditioning. For fibres, a novel experimental technique named Sound Measurements, based on sound acquisition, proved its applicability to gather information about the distribution of fibres strengths within a bundle.

Simulations of the constituents showed how water affects the parameters of the Arruda-Boyce model for polymers and the Weibull model for fibre bundles. The comparison of the experimentally measured properties of the composite with those obtained by homogenisation suggested that matrix-fibre interface must have suffered damage from water absorption. Finally, a numerical study of water-induced stresses due to matrix swelling and viscoelastic relaxation was conducted and determined the history of stresses arising during the water absorption process due to the expansion of the matrix.

Acknowledgements

My life as a student at the University of Oxford has been a truly incredible experience. I look back at these years, and I cannot believe I have met all those beautiful people, listened to those inspiring talks, or lived in the lovely town of Oxford. Impossible not to smile to such memories. This thesis marks the end of my time as a student and represents an achieved milestone that I cannot take all the credit for. There have been people, many people, who have supported me in many different ways. Without them, my experience at Oxford would not have been the same.

First, I thank my supervisors Nik Petrinic and Vito Tagarielli for their mentoring. Also, I would like to acknowledge my research group, the Impact Engineering Laboratory, where people make a delightful working environment.

As a student, I had the chance to start and take part of several projects. Special thanks to the Oxford Peruvian Society, which made me feel at home despite being 10000 km away from my country. I also want to acknowledge my music band The Oxford Latin Combo, who helped me to keep doing one of the things I love the most and made me look beyond the University walls to integrate me as part of the Oxford city community.

Friends, you are many and cannot mention you all. Thanks so much for those chats over coffee or over lunch in the market, for the jokes, for the smiles, for your time. Special thanks to Susan, for her company and her extremely valuable support during my last year of studies. Finally, I need to mention my family, who despite the distance gave me the motivation to keep going.

List of publications

Journal articles

[1]. 2018 G. Quino, A. Pellegrino, V.L. Tagarielli, N. Petrinic, Measurements of the effects of pure and salt water absorption on the rate-dependent response of an epoxy matrix, Compos. Part B Eng. (2018). doi:10.1016/j.compositesb.2018.03.044.

[2]. 2018 F. De Cola, G. Quino, K. Dragnevsky, N. Petrinic. An extended in-situ method to improve the understanding of fracture mechanics of granular materials using sound measurements. [Submitted to the European Journal of Mechanics - A/Solids]

[3]. 2018 G. Quino, V.L. Tagarielli, N. Petrinic, Effects of water absorption on the strain rate sensitive properties of glass fibre reinforced polymers. [In preparation]

Conferences

[4]. 2017 G. Quino, F. De Cola, K. Dragnevsky, N. Petrinic. Quartz grain mechanics: in-situ testing and sound measurements. Microscience Microscopy Congress. Manchester.

[5]. 2016 G. Quino, V. Tagarielli, N. Petrinic. Degradation of composite materials under extreme conditions. Sinapsis, Paris.

[6]. 2015 G. Quino, V. Tagarielli, N. Petrinic. Effects of strain rate and water ageing upon the properties of epoxy resin matrix for composites. ICCS 18, Lisbon.

Contents

List of Figures

Nomenclature

$\%\Delta w_{sat-comp}^{exp}$	Expected water content in saturated composite
$\%\Delta w_s$	Water content at saturation
$\%\Delta w_s^{comp}$	Water content in a saturated composite
$\%\Delta w_s^r$	Water content in saturated resin
$\%\Delta w_t$	Percent water content
α	Pressure dependence factor
β	Weibull shape factor
δ	Damping characteristic
$\Delta\psi$	Variation of water content
$\Delta\theta$	Variation of temperature
δ_{ij}	Delta kronecker
$\dot{\gamma}^p$	Plastic shear strain rate
ϵ_{ij}	Components of the strain field
ϵ_m	Strain at maximum stress
η	Water-induced expansion coefficient
λ	Lamé's first parameter
Λ^p	Plastic stretch
Λ_i^p	Principal values of the stretch tensor
ν	Poisson's ratio
ν_g	Poisson's ratio of E-glass
ν_r^{Dry}	Poisson's ratio of the dry resin

ν_r^{RD}	Poison's ratio of the resin after re-drying
ν_r^{Sat}	Poisson's ratio of the water saturated resin
ω	Rotation angle
ϕ	Concentration of solute
ρ_c	Density of composite
ρ_r	Density of the resin
ρ_g	Density of E-glass
σ_o	Weibull scale factor
σ_w	Weibull strength of a single fibre
σ_{max}	Maximum stress
σ_u	Tensile strength
σ_{vm}^{EH}	Von Misses stress in element EH
τ	Shear stress
Θ	Temperature
$\underline{\underline{\epsilon}}$	Strain tensor
$\underline{\underline{C}}$	Stiffness tensor
$\underline{J}$	Diffusion flux vector
ξ	Linear thermal expansion coefficient
A	Lumped parameter
a	Mean molecular radius
A_f^*	Equivalent area of the i^{th} fibre
A_m	Maximum amplitude
A_t	Amplitude threshold
A_i	Cross sectional area of the i^{th} fibre
b	Specimen width
B^e	Left Cauchy-Green strain tensor
C_R	Rubbery modulus

C_{ij}	Components of the homogenised stiffness tensor
D	Diffusion coefficient or diffusivity
d	Diameter
D_f^*	Equivalent diameter of the i^{th} fibre
D^i	Rate of deformation
D_f	Fibre diameter
D_{BW}	Diffusivity in boiling water
D_{PW}	Diffusivity in pure water
D_{SW}	Diffusivity in salt water
E^*	Complex Young's modulus
E''	Loss Young's modulus
E'	Storage Young's modulus
E_g	Modulus of E-glass
E_o	Apparent modulus at strain rate zero
E_r^{Dry}	Modulus of the dry resin
E_r^{RD}	Modulus of the resin after re-drying
E_r^{Sat}	Modulus of the water saturated resin
F	Applied load
F^e	Elastic deformation gradient
F^i	Inelastic deformation gradient
F^{sbs}	Short beam strength
G	Shear modulus or Lamé's second parameter
G^*	Complex shear modulus
g^*	Non-dimensional shear modulus
G''	Loss shear modulus
G'	Storage shear modulus
G_∞	Long term shear modulus

h	Slope of yield drop
k	Boltzmann constant
K^*	Complex bulk modulus
k^*	Non-dimensional bulk modulus
K''	Loss bulk modulus
K'	Storage bulk modulus
K_∞	Long term bulk modulus
m	Factor of strain rate dependency of the modulus
M_s	Mass of solute at saturation
M_t	Mass of solute at time t
n	Number of chains per volume
n_b	Number of broken fibres
n_f	Number of fibres in a bundle
N_l	Amount of statistical rigid links
p	Pressure
P_m	Maximum load
q	Thickness
R^2	Coefficient of determination
s_o	Athermal shear strength
s_{ss}	Shear stress in the preferred state
t	Time
T^e	Cauchy stress
T_b	Stress in the Langevin spring
T^{vp}_{dev}	Deviatoric part of T^{vp}
T_g	Glass transition temperature
T_{vp}	Stress in the viscoplastic element
tex	tex number

TS_i	Strength of the i^{th} fibre
V	Volume
V^i	Inelastic stretch tensor
V_f	Volume of fibres
v_f	Volume fraction
V_r	Volume of resin
w_c	Weight of the composite
w_{dry}	Weight of dry specimen
w_r	Weight of resin
w_t	Weight of specimen at time t
w_w	Weight of water
3PB	Three point bending
AE	Acoustic emmisions
DIC	Digital image correlation
EH	Element with highest Von Misses stress
FE	Finite element
GFRPs	Glass fibre reinforced polymers
HR	High strain rate
PSD	Power spectral density
QS	Quasi-static
RTM	Resin transfer moulding
SM	Sound measurements
TS	Tensile strength
UV	Ultra violet
YS	Yield stress

Chapter 1

Introduction

Composite materials constitute a promising and advantageous alternative to metals in various fields of application. However, designing structures with them can be challenging, particularly when degradation, caused by the working conditions, and strain rate dependent behaviour have to be considered. This thesis aims to provide engineers with tools to take into account the effects of both strain rate and water degradation upon the mechanical behaviour of fibre reinforced polymer composites, by approaching the problem in a simple manner: looking at the basic constituents.

1.1 Motivation and background

Metals have been dominating the marine industry for decades. Their main drawback, given the wet working environment, is corrosion. Recently, composite materials are standing as an advantageous alternative due to their multifunctionality, lightweight and resistance to corrosion. Nevertheless, the use of composite materials brings along some challenges.

Even when corrosion is not a problem for marine composites, there are other degradation mechanisms that arise from the service conditions. For instance, humidity [4, 5], water exposure [6, 7], ultraviolet (UV) radiation [8, 9, 10], and temperature

cycles [11, 12] can induce detrimental effects upon the mechanical performance of the structures in the long term. These effects, need to be taken into account during the design, in order to make structures safe and long lasting. Nonetheless, engineers lack of reliable tools to do that.

Water degradation is not the only issue when employing composites in marine applications, high speed loads also need special attention. They can occur when waves hit an offshore structure, underwater blasting in the proximity of a submarine, *etc.* Polymers, or more specifically resins which are widely used as the matrix in most of the industrially employed composites, are known to have a rate dependent behaviour. Consequently, resin based composites are also rate sensitive.

In the last few decades, engineering tends to increasingly rely on computer aided design, motivated by the advancement of computational technologies. In this regard, the finite element (FE) method is still the main technique in use, and is not dependent on the computational power and numerical formulations only, but also on accurate material models. These material models can be developed under two main approaches: (1) a phenomenological, and (2) a physically based one. The former is more pragmatic, while the later describes the behaviour in relation to the intrinsic physical response, but not necessarily in a simpler way. Sometimes a balance between the physically and phenomenologically based approaches is used for convenience. A trade-off between some physics in exchange of efficiency and pragmatism in a given application, usually stands as the best engineering approach. The resulting efficient, accurate and reliable material models able to capture the mechanical response at different conditions are key for engineering design.

The three challenges exposed above motivate the current thesis to seek the characterisation and modelling of strain rate dependent composites affected by water absorption.

1.2 Aim and objectives

This thesis aims to provide a reliable experimental data set and to build a modelling framework that account for the effects of strain rate and water uptake upon the mechanical properties of E-glass fibre reinforced composite unidirectional laminates and its constituents e.g. pure resin and E-glass fibres.

To reach this aims, specific objectives will be achieved:

- To experimentally characterise the resin at variuos wet states and strain rates (from quasi-static to high rate).
- To modify and fit a known constitutive model to the experimental data set, in order to observe which material parameters are affectted by water uptake.
- To characterise with micromechanical experiments the properties of single E-glass fibres in the dry state and after immersion in a water bath.
- To characterise E-glass fibres bundles at various strain rates (from quasi-static to high rate) at dry and wet states .
- To fit a Weibull model to the data set of the bundles of fibres.
- To introduce a non contact method named Sound Measurements, used to explore the strenght distribution of the fibres within a bundle.
- To experimentally characterise E-glass reinforced laminates at various strain rates (from quasi-static to high rate) and wet states.
- To compare the measured elastic properties of composites with those expected from a micromechanical model using periodic homogenisation.
- To explore numerically the influence of water asorption upon the stresses generated within the composite matrix.
- To develope specimen designs that provide consistent and repetitive results.

- To develop testing protocols that can capture the influence of both strain rate and water absorption upon the mechanical performance of fibre glass reinforced polymers and their constituents.

1.3 Research strategy and scope

In the reviewed literature, studies dealing with similar problems looked at degradation in composites or resin systems only, and neglected the contribution of the individual constituents. In addition, with very few exceptions, they did not explored the consequences of water exposure upon their strain rate dependent behaviour. In this thesis, the effects of water and strain rate upon the epoxy resin matrix, and the E-glass fibres are individually investigated. Furthermore, the effects in the composites are contrasted with the predicted values given the previously characterised constituents. Extensive experimental campaigns were performed to observe the influence of water upon the mechanical behaviour of the resin, fibres, and composite laminates. These enabled the possibility of creating a modelling framework that is able to account for the effects of water (Figure 1.1).

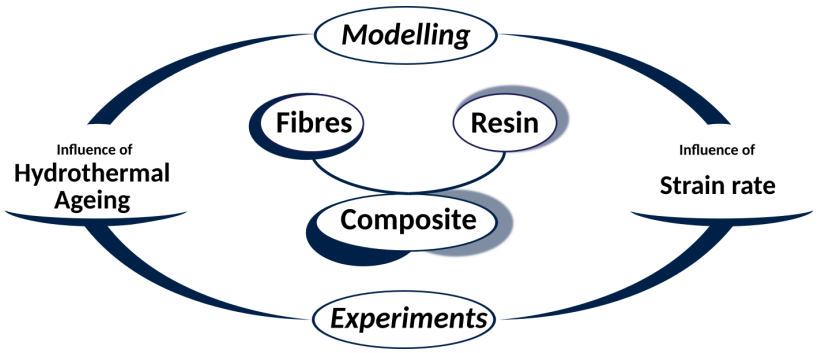

Figure 1.1: Research strategy.

In this work, the scope is focused on the water and strain rate effects upon fibres, resin and how it all has an impact upon the properties of the composites. Failure analysis, and damage evolution in the laminates are not discussed, but considered within the future research directions as data has been produced.

1.4 Thesis outline

This thesis is divided in eight chapters. Chapter 2 presents a thorough revision of the state of the art, to point the gap to be filled with the novelties presented in this research work. This includes previous studies on strain rate dependency and water uptake of the constituents (resin and E-glass fibres), and composites.

Chapter 3 is dedicated to the experimental study of the polymeric matrix. A protocol was defined to capture the effects of pure and salt water effects upon the mechanical properties of the resin. It was shown, for the first time, the influence water absorption upon the strain rate dependent behaviour of resin. In Chapter 4, the Arruda-Boyce model was tuned according to the experimental results, identifying which parameters are those affected by water exposure.

Chapter 5 experimentally explores the mechanics of single fibres and fibre yarns with micro and macro mechanical tests at quasi-static and high strain rate regime with a specially designed gripping system. Again, an experimental protocol was designed to observe the effects of both pure and salt water, showing the resistance of single fibres against the effects of water, but deterioration of fibre bundles. In addition, an alternative method to find the distribution of fibre strengths within the bundle, based on sound acquisition, was developed: sound measurements. The newly introduced method and the Weibull model of fibre bundles were implemented in a numerical experiment to study how well they fit the experimental observations.

Chapter 6 presents the experimental study of composite laminates, which were tested in the resin-dominated modes: tensile 90° and 45°, and short three point bending. A homogenisation framework is implemented to explore the prediction of properties of the composites based on the measurements of their constituents obtained in Chapters 3 and 5. In addition, the finite element (FE) simulations within unit cells revealed that hydroscopic stresses are the result of simultaneous expansion and relaxation mechanisms happening in the polymeric matrix.

Finally, the main conclusions of this thesis are summarised in Chapter 7. Chapter

8 discusses future directions of research based on the generated knowledge and capabilities.

1.5 Research contributions

The research contributions of this work are framed under the aims given above *i.e.* how water degrades the strain rate dependent properties of composite materials and its constituents. Nevertheless, as it will be explained below, on the way to reach this objectives, that by themselves represent novelties, additional contributions to the field have been made.

First, it was performed an extensive experimental campaign to understand how water and salt water absorption affect the mechanical performance of an epoxy resin in a wide range of strain rates (0.001-2000 s^{-1}). This shows, for the first time, how the strain rate dependent properties of the polymeric matrix change after being exposed to pure and salt water (Paper published in Composites Part B [13]).

In addition, the need of obtaining full field strain measurements during tests and the impediment of having specimens outside the preconditioning environment for long time prior testing (*e.g.* long time to paint a speckle pattern on specimens), led to the development of a technique to produce rapid high quality speckle patterns. This method can be used in a wide range of materials, and has been adopted by other colleagues in the Impact Engineering Laboratory of the University of Oxford.

Another contribution, achieved during the study of the "ingredients" of composite materials, has been the exploration of how water immersion affects the properties of single fibres and bundles of fibres, and the implications in the Weibull model. During the investigation of fibres, a novel experimental technique named Sound Measurements was developed. It made use of the sound emitted by the fibre breakage to assess survivability and strength distribution in the bundles. What is more, this technique proved its applicability in other fields. I was also applied to better under-

stand the physics behind the crashing of granular materials (Submitted paper to the European Journal of Mechanics A/Solids, and conference posters).

Whilst there have been previous studies on the influence of water upon composites, to the best of our knowledge, none of them has analysed the direct effect of every single constituent upon the overall degradation of the composite. Here it was performed for the first time, a comprehensive study on the effects of water upon each constituent. The homogenisation strategy followed, showed how the effects of water on the matrix and fibres reflect upon the degradation in the composite. Additionally, numerical simulations in the unit cells suggested that when relaxation and hydrothermal expansion occur simultaneously, the history of stresses up to full relaxation and complete expansion can be obtained.

Chapter 2

Literature review

Whilst there have been many reports in previous literature regarding hydrothermal aging or water-induced degradation of polymers and composites, little attention has been paid to the influence it has upon strain rate dependent properties. This chapter surveys the existing literature and points out the existing gaps in experimental and numerical research, which will be covered by this thesis.

2.1 Strain rate dependency

The different response of a material to a different rate of deformation is known as strain rate dependency. This type of behaviour can be found in a wide range of materials such metals, polymers, composites, and even ceramics.

The characterisation of rate dependent properties rely on the appropriate selection of the testing method at each strain rate. To observe the response of the material at strain rates in a range of several decades, different testing apparatus are needed. Figure 2.1 portrays part of a figure made by Lindholm [1], where the strain rates are classified according to their magnitude. The testing methods associated to every range of strain rates are also indicated.

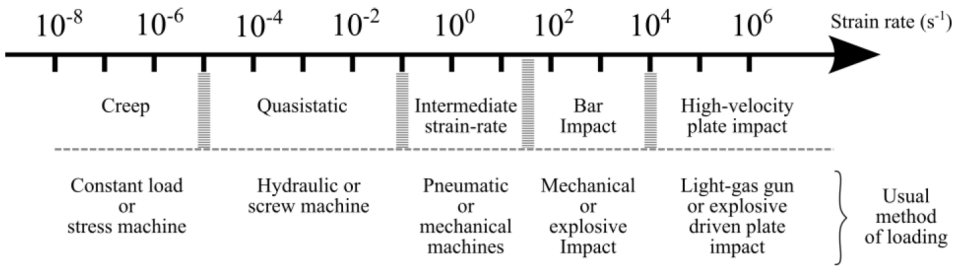

Figure 2.1: Dynamic regimes and testing techniques associated to them [1].

2.1.1 Strain rate dependency of polymers

The mechanical properties of polymers, due to their viscoelastic nature, can be highly dependent on the strain rate. The strain rate dependency of epoxy resins have been previously studied experimentally [14, 15, 16, 17, 18]. It was found that increasing the strain rate increases some mechanical properties such as the yield stress [14, 15, 18, 19], the elastic modulus [17, 18], and the compressive strength [17]. The ductile-brittle behaviour at tensile and shear can also be affected, with more brittle behaviour at higher strain rates and more ductile response exhibited at slower rates, as Gilat *et al.* [20] showed in experiments with epoxy resin at strain rates from $450 - 700\,\mathrm{s}^{-1}$. Fracture toughness seems, however, to decrease with the loading rate [21, 22].

Some other studies have included strategies to translate the strain rate sensitivity of polymers captured in the experiments into numerical models.

Chen and Zhou [23] studied the Epon 828/T-403. They suggested that the strain rate dependency of the yield stress is driven by the competition of strain rate hardening, which dominates at lower strain rates, and softening due to the adiabatic heating. Those two factors lead to a maximum yield stress at a certain high enough strain rate. They proposed a fully phenomenological modification of the Johnson-Cook model to capture the strain rate dependent behaviour of elastic deformation up to the yield point, without softening, in the strain rate range of $0.0001 - 5000\,\mathrm{s}^{-1}$.

Gerlach *et al.* [18] studied the thermoset resin RTM-6 experimentally and nu-

merically. The hydrostatic stress effects were studied with tests in compression and tension at strain rates from 0.001 to 5000 s^{-1}. They proposed the use of a specially designed pulse shaper to improve the homonegeneity of deformation within the specimen by entending the rising time of the stress wave. Their results showed an increase and a non linear dependency of the yield modulus and apparent modulus with respect to the strain rate. They also modified Goldberg model [20] to capture the non linear strain rate dependence of the yield modulus, the apparent modulus as well as the effects of pressure. In addition, a rate dependent strain to failure was implemented.

Boyce *et al.* [24, 25, 26] developed a physically based constitutive model for glassy polymers that captures the effects of strain rate and temperature. This model is capable of capturing strain softening (due to reorientation of molecules) after a local maximum stress was reached, followed by hardening driven by the entropic resistance. They showed the validity of their model at strain rates up to $1\,s^{-1}$ for polycarbonate [24] and Poly(methyl methacrylate) [26]. Mulliken and Boyce [27] expanded the model to account for strain rates within the range $0.0001 - 10000\,s^{-1}$.

2.1.2 Strain rate dependency of fibres

To measure the mechanical properties of fibre bundles at high rate, the split Hopkinson bar has been predominantly the preferred method. Even for single fibre, a miniaturised variation of the Kolsky bar was used to measure the high strain rate strength of Twaron and Kevlar single fibres [28]. Drodge *et al.* [29] employed a ballistic test to measure the mechanical behaviour of silk single fibres. The strength and modulus of bundles of fibres tend to increase with growing strain rate [30, 31, 32, 33].

For fibre bundles at any strain rate after a maximum load is reached, it follows a progressive failure of fibres. Some studies have found a Weibull distribution of strengths within a bundle to replicate their experimental observations [32, 34, 35, 36]. In addition, external effects such as temperature can be captured with this approach [35, 37].

To date, no study has explored the effects of water immersion upon the strain rate dependent behaviour of glass fibres, or the influence of water exposure upon the Weibull parameters.

2.1.3 Strain rate dependency of composites

With respect to the tensile properties of fibre reinforced composites, it has been mostly observed that the strength and modulus of glass-epoxy composites increase with higher strain rate [38, 39, 40, 41, 42, 43]. However, Hayes and Adams [44] reported no specific or clear trend in the influence of strain rate on the modulus and tensile strength of glass epoxy composites. Armenàkas and Sciammarella [45] actually reported a decrease in the strength of S-glass reinforced poxy with higher strain rates. Nevertheless, their results suggest that no equilibrium was attained in their tests. In addition, the non homogeneous strain field observed with Moiré interferometry, indicate some issues with their specimen manufacturing and mounting system. Lifshitz [46], in drop tower and quasi-static tests of angle ply balanced laminates, reported increase of strenght but no increase or decrease of the modulus with the strain rate. Gerlach *et al.* [42], who developed a special clamping system for tensile testing in the fibres direction, found an increase of tensile modulus and strength with higher strain rates in composites tested at various configurations (0°, 45°, 90°, ±45°).

Shear strength and modulus seem to increase linearly with respect to the logarithm of strain rate [43]. In case of compression behaviour, Cui *et al. [47]* reported increements of strength of up to 50% in the compression and tension yield stress of 45° oriented carbon fibre reinforced composites. Compression in the through thickness direction also appears to be strain rate dependent as Guden *et al.* reported [48]. They found both the compression strength and modulus of woven composites to increase with the strain rate. Gerlach *et al.* [42] found the average through thickness tensile strength of laminates to be independent of the strain rate, however scatter in the data prevented them from drawing a clear conclusion on this. Govender *et al.* [49],

studied the through thickness modulus and strength, and the spallation phenomenon in vinyl ester reinforced with E-glass fibres. For their compression tests at high strain rate, they designed a conical pulse shaper to minimise the variability in the strain rate during the Hopkinson bar experiments. Results showed the increment of the out of plane compression strength from 417 MPa at quasi-static regime to 462 Mpa at 510 s^{-1}.

2.2 Effects of wet aging upon mechanical properties

Aging is the deterioration of material properties due to external conditions. Depending on the nature of the phenomenon, they can be physical, chemical, *etc.* Hydrothermal, water, or wet aging is the deterioration caused by the influence of water. In the case of polymers and their composites, this type of degradation should be taken into account during the design of the structures, as they are meant to remain safe over time. In the subsections below, some mechanisms and effects of this phenomenon on composites and their constituents are reviewed.

2.2.1 Wet aging of epoxy resin

There are two main ways in which water absorption has been investigated experimentally: (1) by immersing specimens in water; and (2) by placing them in a climatic chamber with controlled humidity. Although it seems that there are differences in the physics of diffusion in those methods as shown by Fan *et al.* [50], the effects on the material are usually detrimental to the mechanical properties, regardless the technique of aging employed. Real structures are in service for times up to 20 years or longer. This exposure time is not practical to implement in the laboratory; hence, accelerated aging techniques must be employed. These techniques rely on placing specimens in hot water baths. The equivalence of the accelerated method with the real degradation in service may be challenged [51]; however, immersion in hot wa-

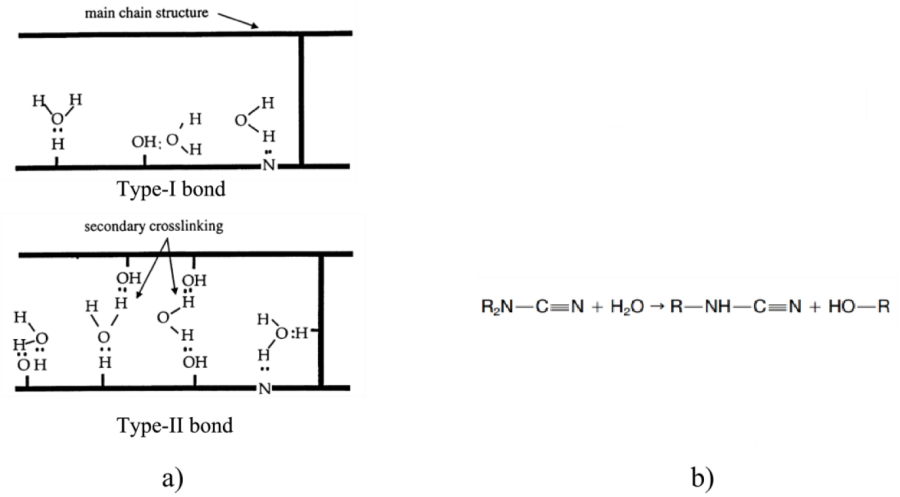

Figure 2.2: Chemical interactions between water and polymer: a) Two different types of bonding according to Zhou and Lucas [2], b) Chain scission according to Xiao *et al* [3].

ter is the generally accepted technique, with particular care to not exceed the glass transition temperature of the epoxy matrix.

Water absorption in polymers, at macro-scale observation seems to follow Fick's laws of diffusion [13, 52, 50, 53]. Nevertheless, depending on the type of polymer and the aging conditions, non-Fickian behaviour has been also observed [54]. This phenomenon responds to more complex mechanisms than just water molecules moving through the bulk. When water is absorbed, molecules can: (1) occupy free volumes in the polymer network [55, 56, 2, 57]; (2) dissolve the bulk [55]; (3) form chemical bonds with hydrophilic sites of the polymer [2, 55]; and (4) produce chain scission [3, 58]. When forming bonds, two main types of bonds can be found [2]: type-I, in which only one hydrogen of the water molecules binds to the network, and type-II, in which two hydrogen atoms of the water molecules are bounded to the network, creating a secondary crosslinking in the polymer structure. Figure 2.2 depicts the possible chemical interactions occurring in the polymer: bonding and chain scission.

To describe the diffusion phenomenon, two main parameters are considered: the diffusion coefficient D and the water content at saturation ($\%\Delta w_s$). Their calcula-

tion, in case of Fickian water absorption, can be evaluated experimentally according to the procedures described in references [59, 60]. It relies on the weight monitoring of samples that are in a conditioned environment absorbing water. The diffusion coefficient is a material property that increases its value with the temperature [61, 62], and indicates the speed of the diffusion phenomenon with respect to the concentration gradient. Generally, the water content at saturation is independent of the temperature [2, 61]. However, previous studies have found some dependency on the temperatures [58, 62], or at least higher values of $\%\Delta w_s$ for temperatures above T_g. Fan *et al.* [50] explored moisture absorption at temperatures above the glass transition temperature (T_g). They found greater values of $\%\Delta w_s$ due to the increase of free volumes above T_g. This is in contrast to their previous reports that water content at saturation is independent of temperature in general. The time to reach saturation varies widely depending on the material and conditioning techniques used. Saturation times of 1500-3000 hours [63], 1600 hours [64] have been reported, while in other cases, saturation was not reached even after 10000 hours [65].

In case of salt water diffusion, generally there is smaller $\%\Delta w_s$ with respect to the one found in pure water diffusion [66, 62]. The diffusion coefficient in a salty environment has been found to be sometimes higher or smaller to the diffusion coefficient in pure water [66].

2.2.2 Water effects on glass

Contrarily to what it would be expected from glasses given the inert character that they usually present, they can physically and chemically interact with water molecules. Chemical interaction with water in the environment can promote stress corrosion [67], leading to subcritical-crack growth and static fatigue [68]. Experiments in vacuum showed how medium with lower water content (lower humidity) correlated with an increase of the mean strength of E-glass fibres [69]. Similarly, Korwin-Edson *et al.* [70] reported decreasing strength of fibres with higher test humidity. Moreover,

Kurkjian *et al.* [71] found that distilled water immersion of fibres at 25°C for eleven days decreased the strength of fused silica fibres up to 40%.

Within the composites, fibres can be dissolved partially by the water [72], modifying the surface roughness [73], and adding electrolytes that may alter the activity of water in the composite [74].

2.2.3 Wet aging of composites

Absorption in composites is not always Fickian due to additional water interaction mechanisms in the composites with respect to the ones acting on the neat polymer, such as water allocation in the fibre-matrix interface. Diffusivity in composites has been found to be anisotropic, being faster in the direction of the fibres and higher than the theoretical expected value, showing the importance of the interface in the water absorption process [51]. A higher volume fraction can increase both diffusivity and the water content at saturation [7], but will be still lower than those of the pure polymer [7, 6]. Diffusivity in composites can be higher [75] or lower [76] in a pure water environment with respect to the saline one, similarly to what happens in polymers in which it also exists contradictory data [66]. Similarly to polymers, $\%\Delta w_s$ is higher in non-saline medium [75].

The damage occurring in the composite comes from: (1) damage the epoxy matrix takes, which was explained in Section 2.2.1; (2) damage in the fibres as described in Section 2.2.2; and (3) damage at the fibre - matrix interface (debonding) [77, 78, 79]. Changes in composites due to aging can be reversible (matrix swelling) or non-reversible (chemical modification of the matrix, micro- cracking, leaching). This means that sometimes properties can be partially recovered after re-drying [7]. The matrix-fibre interface plays an important role in the degradation of composites due to the water molecules that can be accommodated here which weakens the interface and promotes fibre debonding [4]. Leaching has been observed in some composites, for instance in the ones with polyester matrix [80], and even in DGEBA epoxy matrix

composites [51]. Microcracks can appear due to swelling or different thermal expansion coefficients between the matrix and fibre [51, 81].

Dewimille and Bunsell [51] observed little change in the damping characteristic (δ) of the composite when aging occurs at temperatures far below T_g , while increments above 400% were observed when the aging process was carried out above 80°C. Alawsi *et al.* [4] investigated the influence of humidity upon the flexural properties of symmetric and anti-symmetric glass fibre reinforced epoxy laminates placed in an environmental chamber, while Aldajah *et al.* [82] studied the influence of water immersion. In both cases they observed a decrease in the flexural strength after 2000 hours of exposure to humid conditions (over 50% in the case of symmetric laminates). Flexural modulus is also reduced after water immersion [80, 82]. Degradation of flexural properties were more severe in anti-symmetric than in symmetric ones [82]. Bian *et al.* [7] found dramatic decrease on the tensile strength, the flexural strength and the interlaminar shear strength of 13%, 43%, and 50% respectively after 42 days of water immersion.

Mouzakis *et al.* [81] studied the glass fibre isophtalic polyester composite under cyclic hygrothermal aging + UV radiation in a climatic chamber. They reported stiffening of the matrix possibly due to: post-curing of the matrix and leaching of light molecules. The fatigue behaviour was studied by Vauthier *et al.* [83], who observed a decrease in composite lifetimes after water immersion at different temperatures, and also noticed that environmental humidity has a negative effect in lifetime. Pauchard *et al.* [84] found the water uptake to strengthen the negative effects of static fatigue in glass fibre reinforced polymers (GFRPs) due to subcritical crack growth.

Evidence suggests that the degradation induced by non-salt and salty water is similar when comparing the decrease of flexural or tensile properties of aged with respect to non-aged samples [75, 4, 82]. However, Liao *et al.* [77] observed a slightly higher decrease of the properties of specimens after salt water aging.

2.3 Identified research gaps

The research to date has focused mainly on exploring the effects of water upon either polymers only or composites, rather than the composites and all their constituents. In addition, very little or no studies have explored both strain rate and water effects on the mechanical behaviour of such materials.

For polymers, no study has combined the effects of water and experiments at a wide range of strain rates in both compression and tension, to include pressure effects that play an important role in these type of materials. In addition, there is still no consensus about the difference between water absorption effects of pure and salt water. Finally, the available rate-dependent constitutive material models do not consider the effects of water.

Despite there are previous studies on fibres and their dynamic response, no one has determined the implications of wet environments upon the behaviour of single fibres, and bundle of fibres at a wide range of strain rates. Moreover, the application of acoustic techniques in the experimental study of fibres has been limited to the use of contact probes, disregarding the possibility of obtaining information from the acoustic waves travelling through the air.

The only study that has treated the problem of the effects of water uptake upon the dynamic properties of composites was performed by Wolsenbet and Gupta [85]. Through an experimental campaign with compression, they found an increase of strength and matrix-fibre interface damage with water saturation. They attributed this increase of the strength to the rate sensitivity of polymers. Nevertheless, their analysis does not take into account that in compression, the deterioration of the interface should not have a big effect upon the mechanical response, as fibre detachment will not prevent the fibres to carry or to distribute compressive loads. The higher dynamic strength of their water saturated specimens in comparison to their dry one, must be due to the strain rate sensitivity of the fibres, which they did not take into account. Finally, little attention has been paid to the role of the combined effects of

relaxation and matrix swelling to obtain an actual history of water-induced stresses within the composite under water exposure.

All these research gaps motivated each of the following chapters. A recapitulation of these gaps will be briefly described in the introduction of each of them.

Chapter 3

Effects of water absorption on the rate-dependent response of an epoxy matrix

The effects of water immersion upon an epoxy resin system was characterised after exposure to wet conditioning environments including pure water, salt-water solution, and pure water at boiling temperature. Vickers hardness and indentation creep tests were performed and the mechanical response of the material to uniaxial stress was also measured in both compression and tension, at imposed strain rates in the range 0.001–2500 s^{-1}. The Fickian absorption of both pure and salt water caused decrease of stiffness, yield stress and hardness, but only mildly affected the sensitivity of the response to the imposed strain rate and the tensile ductility. Mechanical testing after re-drying of the samples revealed the permanent effects of water absorption.

3.1 Introduction

To allow effective designs and detailed numerical simulations of the effects of water absorption on the response of GFRPs, it is necessary to measure the sensitivity of

the constituents to water absorption. This Chapter focuses on the neat epoxy resin, due to its widespread application as a matrix material in GFRPs. Several studies have been published on the effects of water absorption on different polymers *e.g.* [86, 55, 87, 65], but to the best of our knowledge little research has been published, to date, on the effect of water exposure on the strain rate sensitivity [88, 85, 89] of the resin. This study aims at filling this gap in the literature, while providing a comprehensive dataset to guide FRP material design and to calibrate constitutive models used in numerical simulations.

The strain rate dependency of epoxy resins has been studied mostly experimentally (*e.g.* [14, 15, 16, 18, 17]) and is widely accepted that high imposed strain rates tend to increase the yield stress [14, 15, 18, 19], the material stiffness [19, 17] and the compressive strength [17]; the ductility in tension and shear can in some cases be decreased [20], resulting in decreasing toughness [21].

Several studies have focused on the physical and chemical mechanisms governing water absorption in polymers. Apicella *et al.* [55] showed that absorbed water can dissolve the bulk polymer, make bonds with hydrophilic sites or occupy the material free volume. It is also accepted that chemical interaction (*e.g.* formation of both type-I and type-II bonds) plays a major role in the degradation of the mechanical response [58, 90, 50]. Zhou and Lucas [90] stress that such bonds may increase the overall molecules mobility, such that water acts as a plasticizer (Type I bonds) or induce secondary crosslinking (Type II bonds), which has the opposite effect to Type I bonds; which effect is prevalent depends on the details of the molecular structure, in ways that are difficult to predict in absence of detailed measurements. Xiao *et al.* [3] and De'Nève and Shanahan [58] also reported chain scission induced by water absorption. In some cases water molecules may remain free, causing only minor distortion of the microstructure [91]. Several authors studied the mechanisms of diffusion of water in different polymers; for some, diffusion has been observed to be in accordance to Fick's law [50, 2], while for others such law was not adequate [54, 63].

Water absorption can modify several properties of polymers, such as glass transition temperature (T_g) [90], stiffness [92, 93], tensile strength [92, 94] and fracture toughness [87, 95]. It also induces notable hygroscopic strains [96, 97, 50, 65]. Several authors examined the reversibility of the effects of water absorption; in some cases these were fully reversible [90], while other authors observed permanent changes [3, 93]. Zhou and Lucas [90] suggested that the change of T_g is not only a function of the amount of absorbed water, but also of the time and temperature of exposure, as the amount of type-II bonds may be affected by temperature and time.

The published literature clearly shows that the mechanisms of water absorption and its effects on the mechanical response are complex and very difficult to model at molecular level; rather, extensive measurements are needed in order to quantify the effects of water absorption on the mechanical response of polymers. In this Chapter we report, for an epoxy resin exposed to water, the diffusion properties, the Vickers micro-hardness, and the uniaxial tensile and compressive response for a wide range of imposed strain rates. We perform our measurement following exposure to pure water or a solution of salt (NaCl), at two different temperatures; we explore the effects of re-drying sample, to assess the reversibility of the microstructural changes induced by water absorption.

3.2 Material and sample design

All samples were machined from 20 mm thickness moulded plates of PRIME™ 20ULV, an ultra-low viscosity system provided by Gurit, which is a mix of Prime 20LV resin and a slow epoxy hardener. Resins with similar formulation, are widely used in the manufacture of GFRPs plates for marine applications. Epoxy plates were made by slowly pouring de-gassed resin between glass plates; the system was cured at room temperature for 24 hours and post-cured at 50°C for 16 hours, prior to slow cooling (over 24 hours) to room temperature. The glass transition temperature, according

Table 3.1: Specimen dimensions.

Tag	$D\ (mm)$	$H\ (mm)$
D4	4	1.73
D6	6	2.60
T	3	4

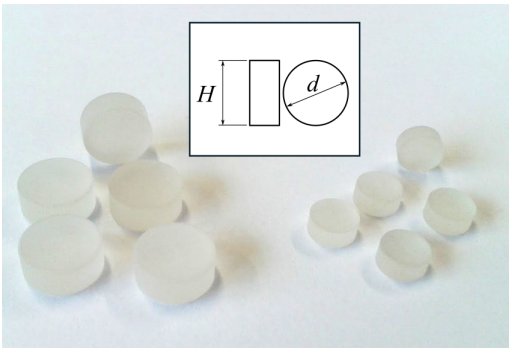

Figure 3.1: Compression specimens.

to the the technical information provided by the supplier in the data sheet of the material, was T_g =87°C.

Tensile and compression samples were designed with a minimal volume to obtain less heterogeneous water absorption across the bulk, and to reduce the times to achieve saturation. At the same time, since the specimens would be tested at high strain rate, they should satisfy some particular requirements. At high strain rate the specimens should not be too long as that would lead to inertia effects in the longitudinal direction and to a less uniform deformation accros the coupons as well as making equilibrium difficult to achieve. In addition, making a too short specimen would bring undesired inertia effects as the mass accelerating in the radial direction of the samples would create unwanted forces in such direction, making the not unidirectional.

In order to minimise the inertia effects, Gorham [98] found that the ideal height H to diameter d ratio was equal to $\sqrt{3}/4$. This low aspect ratio may result in a considerable hydrostatic stress component during test, but it was prevented using petrol gel as lubrication. For compression tests, two sample sizes were fabricated (D4 and D6 samples) with dimensions as shown in Table 3.1 and Figure 3.1.

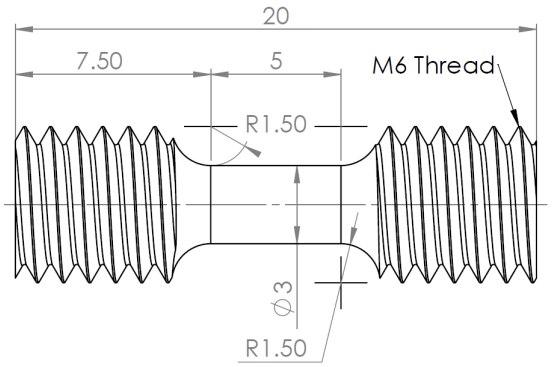

Figure 3.2: Tensile specimen geometry.

Tensile specimens were designed with dog-bone shape with threaded ends for easy mounting in the testing apparatus, with dimensions summarised in Figure 3.2. Previous studies performing high strain rate tensile testing on resins made use of metalic endcaps [18]. However, as specimens have to be immersed in water for months, the metallic endcaps would corrode. By making the threaded specimens, the challenge lies on making sure that failure happens within the gauge section. The dimmensions chosen were a result of trial and error until finding a set of dimmensions providing both force equilibrium and consistent failure in the gauge section.

3.3 Water absorption

Underwater structures can be submerged in water for periods of up to a couple of decades. For obvious reasons, an experimental campaign with the same time span is not practical. For that reason, water absorption was accelerated by immersing the samples in pure distilled water (PW) at 50°C, which is below T_g and is also a temperature that may be achieved in some marine applications (*e.g.* a boat under the sun in a tropical sea). To investigate the effects of salt water (SW), a second group of specimens were immersed in a saline solution (18 g of salt per 100 ml of water). A smaller third group of compression specimens were immersed in boiling

water (BW) to explore the consequences of water absorption at a temperature above T_g (only tested in quasi-static regime).

Before water immersion, samples were dried for up to 500 hours in a Binder FED series oven, at 50°C. A batch of samples, named "as manufactured" (AM), was not dried to assess the effects of the initial drying on the material properties. During drying, the mass was periodically monitored by weighing the specimens with a precision balance (OHAUS DV215, 0.01 mg resolution), determining the percent water content $\%\Delta w_t$ defined in Equation 3.1.

$$\%\Delta w_t = \frac{(w_t - w_{dry})}{w_{dry}} \times 100\%, \tag{3.1}$$

where w_t is the weight at the time t, and w_{dry} is the weight of the fully dry specimen ($\%\Delta w_t = 0$). Complete drying was identified with the stabilisation of the water content, which in case of compression specimens, was achieved after approximately 250 hours.

After drying, a group of specimens was placed in the PW bath, saturating after 1000 hours. A second group of dry samples was immersed in in the SW bath, stabilising after 600-1000 hours. To achieve a uniform diffusion, all faces of the specimens were in contact with water; this was ensured by placing the samples on top a fine mesh avoiding contact with the walls of the container.

A third group of dry D4 samples was placed in a container with boiling water for 8 hours, until saturation was observed.

The absorption of pure, salt, and boiling water was measured by weighing the samples, therefore determining the percent water content $\Delta w_t\%$ is defined in Equation 3.1. At saturation, when the weight is maximum, the corresponding water content is $\%\Delta w_s$. The time histories of water absorption are reported in Figure 3.3.

To track the degradation of properties, some samples were extracted from the aging bath and tested at different imposed strain rates (0.001s^{-1}–2500s^{-1}) for various aged states. At least three specimens were tested at each condition. The average and

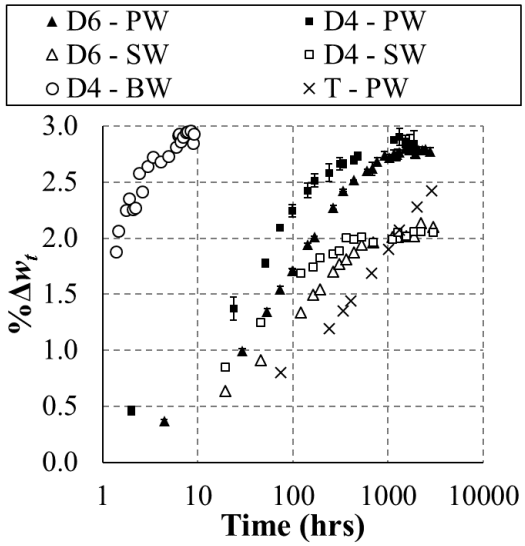

Figure 3.3: Time histories of water absorption for different compression and tensile specimens.

the standard deviation (error bars) of the three tests are reported for quasi-static tests. At high strain rate, as the strain rates are not the same in all tests, every single test result will be plotted.

To study the recoverability of properties after saturation, samples were re-dried in the oven at 50°C until no significant weight change was observed, and subsequently tested. These sets will be identified as PW-RD and SW-RD for specimens redried after pure water or salt water immersion respectively.

3.4 Diffusion response

To characterise the diffusion of pure water in the epoxy resin, a flat specimen of epoxy (PL) with dimensions $30 \times 50 \times 2.4\,\mathrm{mm}^3$ was manufactured and subjected to the initial drying, followed by a water immersion as described above. The change of mass in the plate as a function of time of immersion was used to back-calculate the diffusion parameters, as follows. Preliminary compression tests in three different directions revealed that the mechanical response of the epoxy was approximately isotropic, suggesting an isotropic microstructure. The first and second Fick's laws of

diffusion, in their isotropic form, can be summarised in Equations 3.2 and 3.3.

$$\underline{J} = -D\nabla\phi, \tag{3.2}$$

$$\frac{\partial\phi}{\partial t} = D\nabla^2\phi, \tag{3.3}$$

where $\underline{J}$, is the diffusion flux vector, ϕ is the concentration in arbitrary units, D is the diffusivity of the material, and t is the time. For the case of one-dimensional diffusion in a thin plate of thickness h, integration of Equations 3.2 and 3.3 gives [60]:

$$\frac{M_t}{M_s} = 1 - \frac{8}{\pi^2}\sum_{n=0}^{\infty}\frac{1}{(2n+1)^2}\exp\left[-\frac{(2n+1)^2 Dt\pi}{h^2}\right], \tag{3.4}$$

where M_t is the mass of solute at time t, M_s is the mass of solute at saturation. Equation 3.4 can be approximated numerically by Equation 3.5 [60].

$$\frac{M_t}{M_s} = 1 - \exp\left[-7.3\left(\frac{Dt}{h^2}\right)^{0.75}\right], \tag{3.5}$$

According to Equation 3.5, in case Fick's laws hold, the diffusion is characterised by two parameters, the diffusivity D and the water content at saturation M_s. The fidelity of this equation, strictly valid in unidirectional diffusion (*e.g.* infinite plate), was assessed by Finite Element simulations performed in Comsol [99]. The constitutive behaviour was assumed to obey Fick's law; the outer boundaries were assumed to be fully saturated at time $t = 0$, therefore predicting the time history of water content at every point until full saturation. Fitting Equation 3.5 (curve PL-PW-Eq5 in Figure 3.4) to the measured water content of the epoxy plate (PL-PW-Exp in Figure 3.4), allowed the determination of the diffusion parameters of pure water into the epoxy resin. Figure 3.4 includes FE predictions of the time history of average water content in the PL sample (PL-PW-FEM), which superimposes on the gravimetric curve PL-PW-Eq5, showing the accuracy of Equation 3.5.

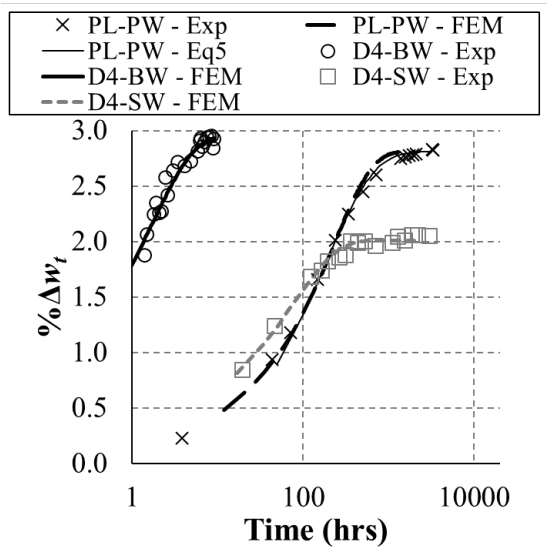

Figure 3.4: Measurements and predictions of the time histories of water content

The accuracy of the FE predictions suggested that water diffusion followed Fick's laws in the case of pure water (PW). The diffusion parameters in the case of salty water and boiling pure water (SW and BW, respectively) were determined from the measured absorption histories on small cylindrical specimens of type D4, as using these small specimens allows saving material and time. An iterative procedure was used to obtain fittings of FE predictions (obtained to simulate water absorption of D4 specimens) to the measurements, shown in Figure 3.4 . The procedure consisted in running FE simulations with several values of diffusivity (varied in steps of 0.01×10^{-13} m^2/s for SW and 0.01×10^{-11} m^2/s for BW) and the measured value of water content. This allowed to identify the optimal values of diffusivity by minimising the differences between experiments and predictions.

As evident from Figure 3.4, diffusion was found to follow Fick's laws also for the cases of SW and BW. The diffusivities for PW, SW and BW were $D_{PW} = 6.05 \times 10^{-13}$ m^2/s, $D_{SW} = 5.6 \times 10^{-13}$ m^2/s and $D_{BW} = 2.7 \times 10^{-11}$ m^2/s. The water contents at saturation were of approximately 2.7%, 2% and 2.9% for PW, SW and BW, respectively. Figure 3.5 presents the loss of water of different specimens upon re-drying. Figure 3.5a suggests that, for the case of PW, approximately 0.3% of water

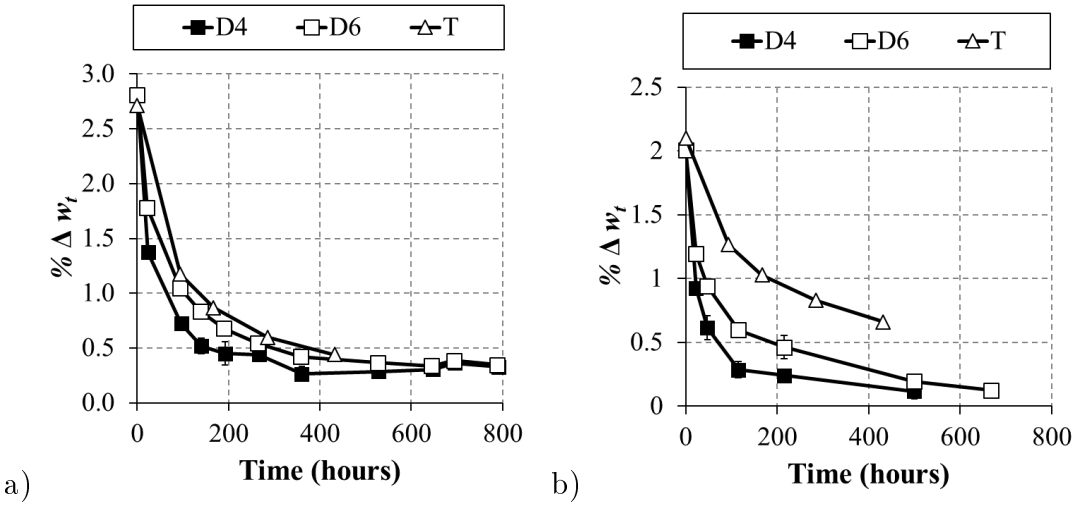

Figure 3.5: Redrying of specimens after saturation in (a) Pure water and (b) salt water.

remains in the polymer after full re-drying; for the case of SW the fraction of water mass permanently trapped in the polymer's structure is of order 0.1%.

3.5 Mechanical characterisation

All mechanical tests were performed in a laboratory at 22°C ± 2°C and 40% ± 8% relative humidity. Pre conditioned specimens were taken out of the water bath and tested within 30 minutes time span as recommended by the standard ASTM D618 [100], to avoid significant water loss in the sample due to evaporation.

Quasi-static tests were performed in the screwdriven universal testing machine Zwick Z250 fitted with a 20 kN load cell at 0.001 s^{-1} and 0.1 s^{-1} imposed strain rates. In the compression experiments, the cylindrical specimens were deformed by two lubricated platens, while metallic threaded grips were used in tensile tests. Displacements were measured with the laser extensometer EIR-L05 (1 μm resolution), tracking 2 reflective bands attached to the platens in case of compression tests and to the ends of the gauge length in case of tensile tests.

Uniaxial tension and compression tests at strain rates above 200 s^{-1} were performed in split Hopkinson bars with setups as described in [18, 101, 102] (Figure

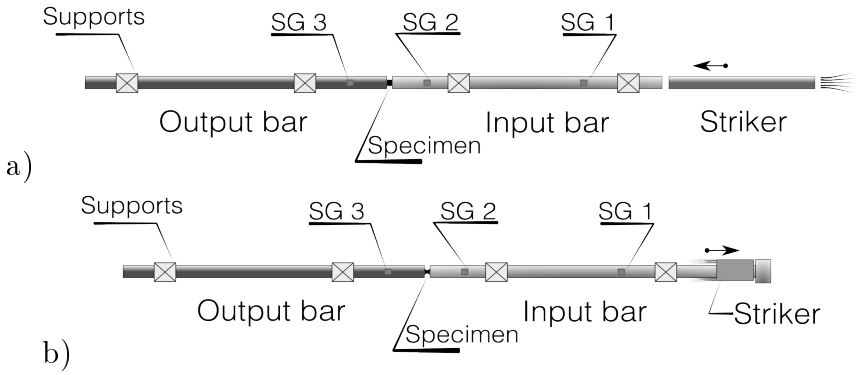

Figure 3.6: Schematic of the split Hopkinson bar in: a) compression, and b) tension.

3.6). In compression, the history of strains and stresses were deduced with the one-dimensional wave theory, as described by Harding and Welsh [41]. In tensile tests, the time history of stresses was obtained with wave theory, while the strain history was calculated with Digital Image correlation (DIC) analysis of the high speed video footage recorded at 200000 fps (taken with the camera Kirana from Specialised Imaging). The times to reach force equilibrium was 40 and 100 μs in case of tensile and compression specimens. After equilibrium was reached, the strain rate was approximately constant. In tensile tests the transmitted force might be small hence a hollowed aluminum output bar was chosen. Since aluminum has a low Young's modulus, the the signal captured from the strain gauge is higher and with better signal to noise ratio.

Microhardness tests were conducted with the hardness meter (Wilson TUKON 1202) with a Vickers indenter. During operation of the machine, a weight 0.5 kg was released onto the indenter. This load was removed after different times (10 s, 50 s, 100 s) to deduce the indentation creep response of the epoxy.

3.6 Results

Results are reported, indicating by a letter whether they refer to tensile (T) or compression (C) tests; the letter is followed by an indication of the conditioning of the

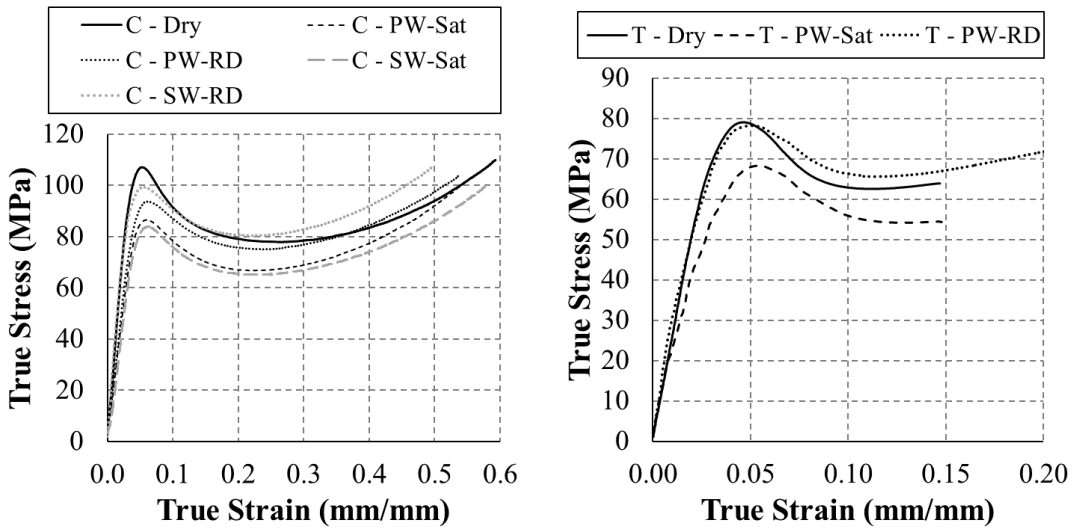

Figure 3.7: Measured quasi-static strain-stress curves at 0.001 s^{-1}.

specimen. In some cases, the last number indicates the strain rate of the test.

Figure 3.7 shows representative true strain-stress curves in compression and tension, at strain rate 0.001 s^{-1}. After an initial elastic regime, the curves show a local maximum in flow stress, denoted as yield stress (YS) in the following. In compression, this is followed by softening and subsequent strain hardening. In tension the response was similar, but ductile failure intervened in some cases prior to strain-hardening. The compressive response was stronger than the tensile response, as expected, and the tensile ductility does not decrease (and, in some cases, increases) as a consequence of water absorption.

Figure 3.8 displays representative true strain-stress curves in tension and compression; the average strain rate following force equilibrium is denoted, in s^{-1}, by the number in the labels. In the following we shall denote as yield stress (YS) either the first peak in flow stress (where this is present) or, where strain-softening is not observed (*i.e.* when the response does not display a stress peak), as the flow stress at a true strain ε_{Dry}^{YS} ; the strain ε_{Dry}^{YS} denotes the strain at peak stress for the corresponding quasi-static test. In compression, the strain-softening phase was negligible, compared to the quasi-static measurements in Figure 3.7; the strain-hardening phase was much

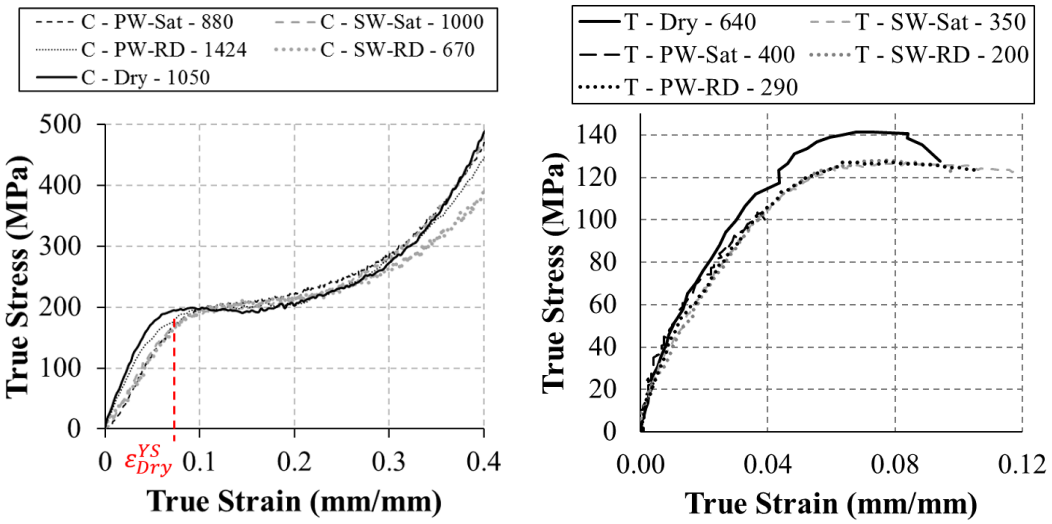

Figure 3.8: Measured strain-stress curves at high strain rates; the average strain rate (in s^{-1}) following force equilibrium is indicated by the numbers in the labels.

more pronounced in dynamic tests than in quasi-static tests. Similar observations apply to the measured tensile response in dynamic tests; the specimen's ductility was much lower in dynamic measurements then in quasi-static tests, as expected.

Figures 3.9 and 3.10 summarise the measured yield stress (YS) and apparent modulus (E) at 0.001 s^{-1} for different types of specimens and following different conditioning procedures. Figures 3.11 and 3.12 present similar information for tests conducted at a strain rate of 0.1 s^{-1}.

To highlight the progressive change in mechanical response with increasing water intake, compressive strength and stiffness (measured at strain rates of 0.001 s^{-1} and 0.1 s^{-1}) are shown in Figure 3.13 as a function of water intake. Figures 3.14 and 3.15 illustrate the strain rate sensitivity in compression and tension, respectively, and after different conditioning procedures. The Poisson's ratio measured with DIC was approximately constant with strain rate and water conditioning $\nu = 0.4$.

The results of Vickers hardness measurements are shown in Figure 3.16. The effects of drying, saturation in PW and SW and re-drying are shown, for three different load dwelling times. While this is not pursued here for the sake of brevity, the data in Figure 3.16 can be used to extract the visco-plastic properties of the material in

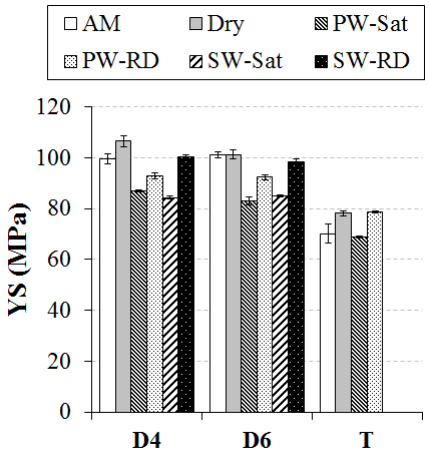

Figure 3.9: Yield stress at a strain rate of $0.001\,\mathrm{s}^{-1}$.

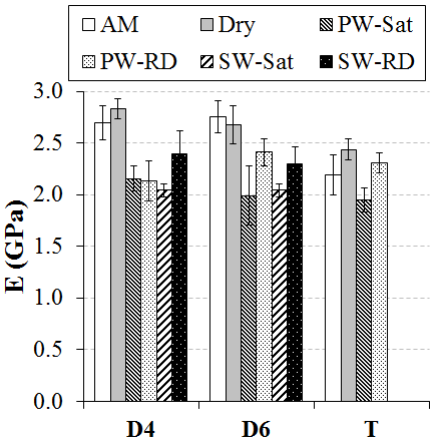

Figure 3.10: Apparent modulus at a strain rate of $0.001\,\mathrm{s}^{-1}$.

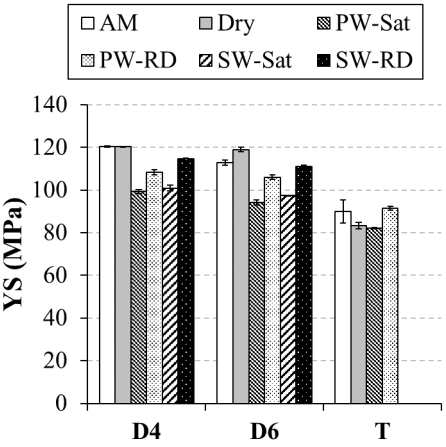

Figure 3.11: Yield stress at a strain rate of $0.1\,\mathrm{s}^{-1}$.

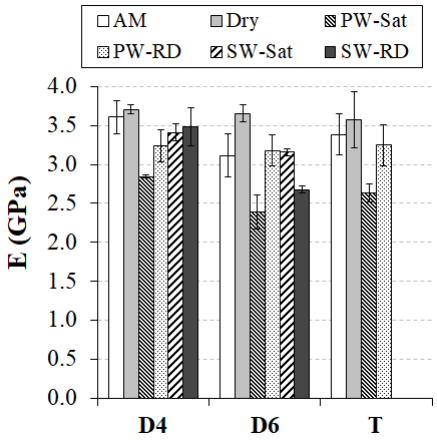

Figure 3.12: Apparent modulus at a strain rate of 0.1 s^{-1}.

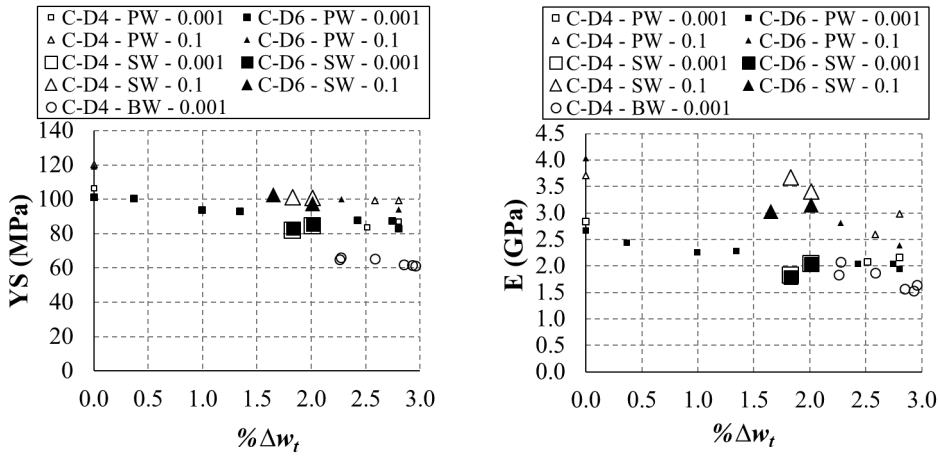

Figure 3.13: Measured strength and stiffness at different water contents and in different conditioning media.

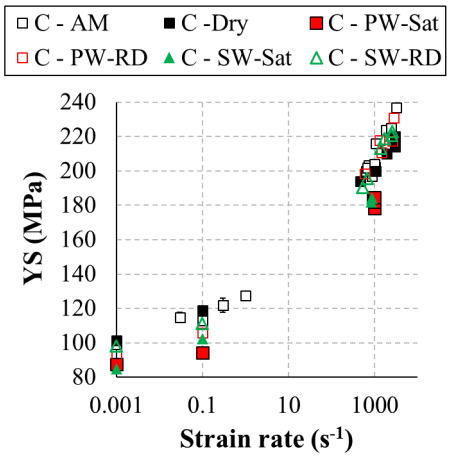

Figure 3.14: Sensitivity of the compressive strength to the applied strain rate.

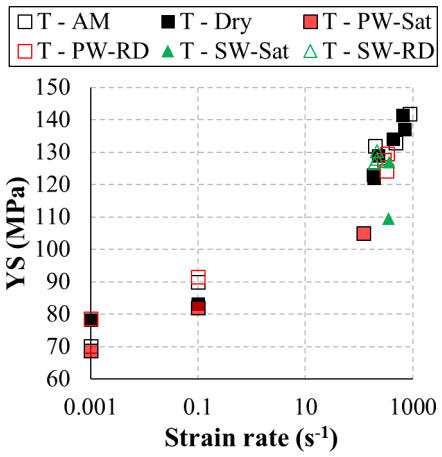

Figure 3.15: Sensitivity of the tensile strength to the applied strain rate.

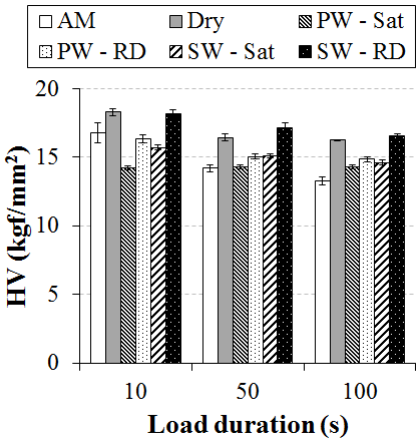

Figure 3.16: Effects of conditioning and load dwelling duration on the measured Vickers microhardness.

the quasi-static regime, by fitting to appropriate models for the creep indentation of visco-plastic solids (*e.g.* [103]).

3.7 Discussion

3.7.1 Water diffusion in epoxy resin

The measured values of diffusivity are in line with previous findings by Scott and Lees [66]. The smaller diffusivity in salt water has been previously explained by a mechanism of inverse osmosis [104], which also justifies the smaller water content at

saturation and the differences in residual water content after re-drying.

In boiling water the diffusivity is two orders of magnitude higher than in pure or salt water at 50°C. Previous studies [61, 2] have shown that the water content at saturation in pure water is approximately independent of temperature, at temperatures below T_g; in this study we found that in boiling water the saturation water content is slightly higher than in pure water; it can be conjectured that since T_g is below the boiling point of water free volumes increase [50], allowing for additional water molecules to reach the bulk of the material.

3.7.2 Effects of initial drying

These effects are evaluated by comparing results of AM specimens with the dry ones in Figure 3.9-3.12. Drying increases mildly both YS and E in the quasi-static regime. This is confirmed by the hardness measurements shown in Figure 3.16. We deduce that the small (0.35%-0.5%) water content initially present in the specimens is acting as a weakening agent of the material. For tests at high strain rate (Figures 3.14 and 3.15), no clear improvement upon drying could was detected, possibly because it actually does not exist in the high rate regime or because of the higher intrinsic scatter of the dynamic tests.

3.7.3 Effects of water absorption

Water absorption clearly showed detrimental effects on the mechanical properties of the epoxy, at all strain rates (Figures 3.13-3.15). The modulus, yield stress, and hardness reduced with increasing water content. Most of the stiffness and strength degradation observed in quasi-static tests occurred after the first two weeks of immersion (corresponding to approximate water intakes of 2.5% and 1.5% in PW and SW, respectively, Figure 3.13). This indicates that a good estimate of the degradation of mechanical properties may be obtained (for the specimen volume investigated here) after only two weeks of immersion. FE simulations, not shown here for the sake of

brevity, confirmed that after two weeks of immersion the concentration of water in the specimen is uniform in specimens of type D4, within a margin of approximately 5%. Figures 3.14 and 3.15 show that while strength reduced with water intake, its sensitivity to strain rate remained approximately unchanged.

3.7.4 Effects of aging above T_g

Figure 3.13 includes the measured properties of specimens aged in boiling water (BW) and shows that clearly this conditioning is the most detrimental, with the strength reducing by 40% compared to fully dry specimens. Immersion in boiling water was a very effective way to accelerate water uptake, however the effects on the properties are not equivalent to ageing at lower temperatures due to additional mechanisms occurring, such as the increase of free volumes or possibly the breaking of both primary and secondary bonds.

3.7.5 Effects of salinity

Figures 3.9-3.16 show that specimens conditioned by salt water have similar properties degradation as specimens conditioned by pure water, even though different values of water content are reached at saturation by these two different types of conditioning. This reinforces the notion that degradation of the mechanical response depends strongly on the composition of the solution diffused in the polymer and not only on the amount of solution absorbed.

3.7.6 Effects of re-drying: recoverability of properties

As seen in Figures 3.9-3.12 and 3.16, mechanical properties were recovered by up to 91% of the values in fully dry conditions. This is related to the data in Figure 3.5, showing that the drying process does not allow removing all water, consistent with the observations of Zhou and Lucas, who reported they were unable to remove all

water in their samples even after 1450 hours of exposure at 60°C [2].

3.7.7 Effects of strain rate

Figures 3.13-3.15 show a clear strain rate sensitivity of this polymer, in line with previously reported data for dry polymers. The mechanical properties are reduced, for conditioned specimens, at all strain rates. The ratio of saturated to dry property however is not the same for the different strain rates. In tests at 0.001 s^{-1}, for instance, water saturation induced more degradation on E (23-25% decrease) than in experiments at 0.1 s^{-1} (8-16% reduction). In general, the mechanical response of the epoxy at high strain rates is less affected by degradation, resulting in a slightly higher strain rate sensitivity for conditioned samples compared to dry samples.

3.8 Concluding remarks

The results of the experimental campaign presented above explored the effects of conditioning in pure, salt, or boiling water on the mechanical response of an epoxy commonly used in marine composite constructions, over a wide range of applied strain rates. We characterised the diffusion parameters for the three different types of conditioning, and diffusion was found to obey Fick's law. We suggested optimal sizes of specimens and conditioning procedures to conduct similar investigations on other materials. We presented a comprehensive set of measurements for the epoxy under investigation, which can be used to simulate the response of fibre-reinforced epoxy after different types of conditionings and at different strain rates; we leave this investigation as a subject for further research. The main conclusions from this study are as follows:

- The diffusion of pure, salt and boiling water in epoxy obeys Fick's law. The diffusivity of pure boiling water in Epoxy is two orders of magnitude greater than in pure water at 50 °C.

- The water absorbed in specimens up to saturation cannot be fully removed by drying.

- Conditioning in salt water solutions until saturation has similar effects on the mechanical properties as conditioning in pure water; conditioning in boiling water has the most detrimental effects on mechanical response. The three different conditionings explored in this study correspond to different water contents at saturation.

- At all strain rates, conditioning until saturation results in a marked decrease in stiffness and strength. The relative decrease in stiffness is higher than the decrease in strength. Tensile ductility was not detrimentally affected by conditioning.

- After conditioning the material retains a similar strain rate sensitivity to that measured in fully dry conditions.

Chapter 4

Constitutive modelling of dry and wet epoxy resin

The Arruda-Boyce model is capable of capturing the behaviour of polymers up to large deformations. In this chapter, the model was modified to account for strain rate dependent elasticity. Additionally, the experiments from the previous Chapter and an optimisation routine were used for the identification of the material model to appreciate how they are affected by water absorption. It was found that only some material parameters could be modelled by a simple piecewise linear law with dependence on the water content $\%\Delta w_t$.

4.1 Introduction

Epoxy resins are widely used in the composites industry as a matrix to keep fibres together, to help to distribute the loads, to provide damping, *etc.* Depending on how the loads are applied, the matrix can play a minor or a major role in the composite response. For instance, in a laminate in shear or an unidirectional plate with a load orthogonal to the fibres, the behaviour of the matrix is of key importance.

The previous Chapter focused on the experimental characterisation of various

properties of an epoxy matrix at strain rates from $0.001 - 2000\,\mathrm{s}^{-1}$ and at various pre-conditioning states from fully dry to fully water saturated. This Chapter investigates how those measurements can be translated into an existing constitutive material model for the epoxy resin.

Polymers exhibit a variety of mechanical response to loads, depending on their composition and the loading conditions. Conversely, material models for polymers are very diverse, some of them are accurate at small strains [18, 23], and others are more complex as they can follow the material response for up to large deformations, including features such as softening and hardening [105, 106, 107, 108, 109].

Some of the efforts on modelling polymers and hydrothermal aging have been put into the diffusion phenomenon [54, 110, 52]. Also, previous research has developed formulations of the governing equations for a deforming polymer, including effects of water vapour pressure by thermal and thermo-mechanical coupling [111, 50]. However, there has been no detailed investigation into any constitutive material model for polymers and the degradation effects caused by water. In this Chapter, a modified version of the Arruda-Boyce model [112] is used to fit the fully dry and fully pure water saturated states of the epoxy matrix. Some parameters were directly obtained from the experiments, while others were the result of an optimisation script.

In the following section, the Arruda-Boyce model and its modification to include strain dependent elasticity are briefly described. In Section 4.3, the setup of the simulations is given. Moreover, the methods for identification of the material parameters are detailed. Finally, in Section 4.5, the obtained parameters are summarised, and a simple evolution law for some parameters with respect to water content is provided.

4.2 Model description

The Arruda-Boyce model [106, 25] can capture the behaviour of polymers for up to large deformations that show softening and post hardening. It has proved its validity

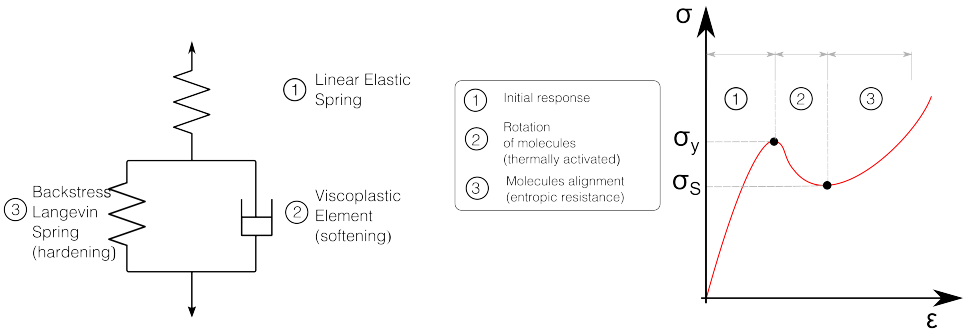

Figure 4.1: The rheological model and a typical strain *vs* stress curve.

for up to strain rates of $1\,\mathrm{s}^{-1}$. As shown in Figure 4.1, three regimes can be identified: (1) an initial linear response until a local maximum yield stress σ_y (the thermally activated yield point); (2) softening driven by the chain rotation up to a stress σ_s; and (3) strain hardening due to the entropic resistance to chain alignment according to the 8-chain model [25]. This model, without pressure dependence, was implemented in a Fortran Abaqus VUMAT written by Tømmernes [113], available through the website of the Norwegian University of Science and Technology [114].

In the following, the three regimes and their material parameters will be described. Additional details about the model and its parameters can be found in the references [106, 25].

4.2.1 Linear spring

The elastic response is driven by the elastic spring 1 in the rheological model of Figure 4.1. A phenomenological approach was followed to modify the model in order to account for a strain-rate dependent elastic modulus $E(\dot{\varepsilon})$. A simple linear dependency with the logarithm of the strain rate was introduced:

$$E(\dot{\varepsilon}) = E_o + m \ln \dot{\varepsilon}_{eq}, \tag{4.1}$$

where E_o is the modulus at strain rate $\dot{\varepsilon}_{eq} = 1\,\mathrm{s}^{-1}$, m is the strain rate dependency factor, and $\dot{\varepsilon}_{eq}$ is the equivalent strain rate evaluated as:

$$\dot{\varepsilon}_{eq} = \sqrt{\frac{2}{3}\left((\dot{\varepsilon}_{11} - \dot{\varepsilon}_m)^2 + (\dot{\varepsilon}_{22} - \dot{\varepsilon}_m)^2 + (\dot{\varepsilon}_{33} - \dot{\varepsilon}_m)^2 + 2\dot{\varepsilon}_{12} + 2\dot{\varepsilon}_{13} + 2\dot{\varepsilon}_{23}\right)}, \tag{4.2}$$

with $\dot{\varepsilon}_m = \frac{1}{3}(\dot{\varepsilon}_{11} + \dot{\varepsilon}_{22} + \dot{\varepsilon}_{33})$.

The Poisson's ratio ν is independent of strain rate, as observed in the experimental campaign from Chapter 3. Thus, the Lame's parameters λ and G are proportional to the strain rate dependent E:

$$\lambda = \frac{E(\dot{\varepsilon}) \cdot \nu}{(1 - 2\nu) \cdot (1 + \nu)}, \tag{4.3}$$

$$G = \frac{E(\dot{\varepsilon})}{2 \cdot (1 + \nu)}, \tag{4.4}$$

Equation 4.5 describes the constitutive relation for linear elasticity:

$$\sigma_{ij} = \lambda \varepsilon_{kk} \delta_{ij} + 2G\varepsilon_{ij}, \tag{4.5}$$

where δ is the Kronecker delta function, and ε is the strain. The strains can take large values in this material model. Therefore the Cauchy stress T^e is preferred:

$$T^e = \frac{1}{\det(F^e)}\left(\lambda \ln\left(\sqrt{B^e}\right) \cdot I + 2G \ln\left(\sqrt{B^e}\right)\right), \tag{4.6}$$

where $\det(F^e)$ is the determinant of the elastic deformation gradient ($F = F^e F^i$), I is the identity, and $B^e = F^e F^{e^T}$ is the elastic left Cauchy-Green strain tensor.

4.2.2 The Langevin spring

The Langevin spring is the element 3 in Figure 4.1. It controls the hardening and contains elements of rubber elasticity. The stress in this element is:

$$T^b = \frac{n \cdot k \cdot \Theta}{3} \sqrt{N_l} \mathscr{L}^{-1} \left\{ \frac{\Lambda^p_{chain}}{\sqrt{N}} \right\} \frac{\Lambda^{p2}_i - \frac{1}{3} I_1}{\Lambda^p_{chain}}, \tag{4.7}$$

where n is the number of chains per volume, Θ is the temperature, the Boltzmann constant $k = 1.38 \cdot 10^{-10}$ N.mm/K. The rubber modulus is defined as $C_R = n \cdot k \cdot \Theta$ and can be substituted in 4.7. $\mathscr{L}^{-1}$ is the inverse Langevin operator, N_l is the amount of statistical rigid links in a chain, Λ^p_i are the principal values of the stretch tensor V^i, $I_1 = (\Lambda^{p^2}_1 + \Lambda^{p^2}_2 + \Lambda^{p^2}_3)$, and Λ^p_{chain}:

$$\Lambda^p_{chain} = \sqrt{\frac{trace(F^i F^{i^T})}{3}}, \tag{4.8}$$

where F^i is the inelastic deformation gradient.

4.2.3 Viscoelastic dashpot

The viscoplastic element is driven by the rotation of polymeric chains and is represented by the dashpot in Figure 4.1. The stress in this element is evaluated from the difference of the elastic and Langevin springs:

$$T^{vp} = T^e - \frac{1}{\det(F^e)} F^e T^b F^{e^T}, \tag{4.9}$$

The equivalent shear stress is defined as:

$$\tau = \sqrt{\frac{T^{vp}_{dev} : T^{vp}_{dev}}{2}}, \tag{4.10}$$

where T^{vp}_{dev} is the deviatoric part of T^{vp}. The rate of deformation is herein defined as $D^i = \dot{\gamma}^p S$, with S:

$$S = \frac{T^{vp}_{dev}}{\sqrt{2}\tau}, \tag{4.11}$$

and the plastic shear strain rate $\dot{\gamma}^p$:

$$\dot{\gamma}^p = \dot{\gamma_o} \exp\left(-\frac{A(s_o - \alpha p)}{\Theta k}\left(1 - \left(\frac{\tau}{(s_o - \alpha p)}\right)^{5/6}\right)\right), \tag{4.12}$$

where $\dot{\gamma_0}$ is the pre-exponential shear strain factor, τ is the shear stress, s_o is the athermal shear strength, p is the pressure, Θ is temperature, A is the product of various constants and α is the pressure sensitivity factor.

The athermal shear strength s_o can be calculated from the shear modulus G from the diagram G *vs* T at the required temperature [24]. This parameter is independent of the strain rate.

$$s_o = \frac{0.077}{1 - \nu} G, \tag{4.13}$$

The lumped parameter A includes the rotation angle ω, the mean molecular radius a, and the Boltzmann constant k.

$$A = \frac{39\pi\omega^2 \cdot a^3}{16 \cdot k}, \tag{4.14}$$

The athermal shear stress evolves from an initial value s_o to a preferred state s_{ss} according to Equation 4.15, where h is the slope of the yield drop with respect to the plastic strain.

$$\dot{s} = h\left(1 - \frac{s}{s_{ss}}\right)\dot{\gamma}^p, \tag{4.15}$$

Table 4.1 lists all the constitutive material parameters of this modified version of the Arruda-Boyce model.

Table 4.1: Material parameters of Arruda-Boyce.

	Symbol	Description
1	E_o	Apparent modulus at strain rate $1\,\mathrm{s}^{-1}$
2	ν	Poisson's ratio
3	m	Factor of modulus rate dependency
4	s_o	Athermal shear resistance
5	$\dot{\gamma}_o$	Pre-exponential shear strain factor
6	A	Lumped parameter
7	$\frac{s_{ss}}{s_0}$	Ratio of yield drop
8	h	Slope of yield drop with respect to plastic strain
9	α	Pressure sensitivity factor
10	N_l	Number of rigid chain links
11	C_R	Rubbery modulus

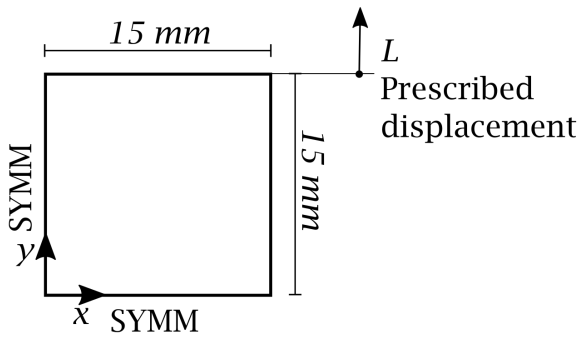

Figure 4.2: Virtual experiment setup in Abaqus.

4.3 Virtual experiments

The model was created in Abaqus 6.14 [115] for tensile and compression modes at two different strain rates: $0.001\,\mathrm{s}^{-1}$ and $0.1\,\mathrm{s}^{-1}$. It consisted of a single element that was either pulled or pushed with a prescribed unidirectional displacement, over a time according to the desired strain rate. Figure 4.2 shows a schematic of the 2D model and the boundary conditions of unidirectional displacement and symmetries.

One set of material parameters should be able to reproduce the experimental results at $0.001\,\mathrm{s}^{-1}$ and $0.1\,\mathrm{s}^{-1}$ in both compression and tension for a particular pre-conditioning state. Thus, four simulation cases were considered and summarised in Table 4.2. The material parameters were identified from the experiments of Chapter

Table 4.2: Simulation cases.

Case	Mode	Strain rate
1	Compression	0.001
2	Compression	0.1
3	Tension	0.001
4	Tension	0.1

3 and an optimisation scheme described below.

4.4 Identification of material parameters

The material parameters were obtained for two extreme pre-conditioning cases: fully dry (Dry), and fully saturated (W-Sat). In addition, an intermediate state of $\%\Delta w_t = 1\%$ was analysed. Parameters 1-4, 7, and 9 from Table 4.1 were obtained from the compression and tensile experiments at different strain rates of $0.001{-}0.1\text{s}^{-1}$ described in the previous Chapter. The remaining parameters were calculated by running an optimisation routine.

Since no tests at $1\ \text{s}^{-1}$ were conducted, the E_o and m parameters at each pre-conditioning state were identified by fitting the experimentally obtained compression moduli E at different strain rates to Equation 4.1 (data from Figure 3.13). In the experimental campaign described in the previous Chapter, the Poisson's ratio ($\nu = 0.4$), measured through DIC analysis on the compression and tensile tests, was observed to be indifferent to strain rates and water treatment.

The athermal shear stress s_o was obtained from DMA tests (Figure 4.3). At room temperature ($20 - 25°\text{C}$), the storage modulus was approximately constant and equal to E measured in quasi-static tests at $0.001\ \text{s}^{-1}$ (2.6 GPa). Therefore, $E(0.001\ s^{-1}) = E'(25°\text{C})$ was used to calculated $G = E/(2(1+\nu))$ and subsequently, s_o with Equation 4.13.

The pressure sensitivity factor α can be measured by a linear fitting of the maximum shear stresses with the different pressures at which they were obtained [116].

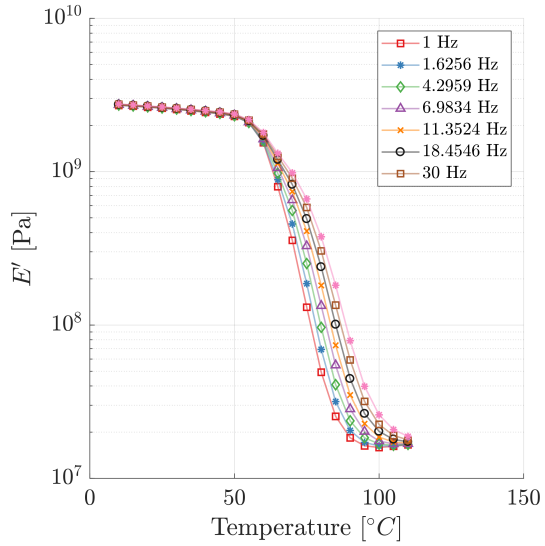

Figure 4.3: Storage modulus versus temperature obtained in the DMA test.s

Thus, experiments in compression and tension can be used to obtain an estimation of α, as they involve different pressures. For tensile and compressive yield stresses σ_y^t and σ_y^c respectively, the pressure sensitivity factor α is:

$$\alpha = -\frac{3}{2}\frac{\left(\sigma_y^t + \sigma_y^c\right)}{\left(\sigma_y^t - \sigma_y^c\right)}. \tag{4.16}$$

Both tensile and compression experiments were performed for Dry and water saturated specimens. The pressure dependence factor α was observed to be approximately independent of the strain rate, but different for each conditioning environment.

The ratio of yield drop $\frac{s_{ss}}{s_0}$ was obtained from compression tests. It is equal to the ratio between the softening and the yield stress (σ_s and σ_y in Figure 4.1) and it was observed that they were approximately independent of the strain rate.

A and $\dot{\gamma}_0$ were initially calculated from compression tests at different strain rates. Boyce *et al.* provided a method to calculate these parameters from the yield stresses in experiments at different strain rates [24]. However, as only two strain rates for each condition were available, and compression and tensile results were giving significant scatter in the values of these parameters, they were left to the optimisation process.

The experiments did not reach a strain large enough to observe locking. Hence, the parameter N_l could not be evaluated from the experimental curves.

Parameters A, $\dot{\gamma}_0$, h , N_l, and C_R were optimised using the `fminsearchbnd` Matlab function [117] which uses the Nelder-Mead simplex search method [118] to minimise the objective function. This objective function requires an initial set of values and allows to prescribe upper and lower limits for the arguments. For A, and $\dot{\gamma}_0$, the initial values and the limits were taken from the scattered data obtained from the experiments and the method by Boyce *et al* [24].

The objective function $\epsilon = \texttt{f\_obj}(A, \dot{\gamma}_0, h, N_l, C_R)$ contained the material parameters to be optimised as arguments. During execution, an Abaqus material card was created and later called by four input files in order to automatically run all simulation cases. The input files corresponded to the virtual experiments of Table 4.2: compression at $0.001\,\mathrm{s}^{-1}$, tension at $0.001\,\mathrm{s}^{-1}$, compression at $0.1\,\mathrm{s}^{-1}$ and tension at $0.001\,\mathrm{s}^{-1}$. Finally, the objective function calculated the error ϵ_{case} between the FE simulation and the experimental data in each simulation case:

$$\epsilon_{case} = P^{mod}(\varepsilon)^2 - P^{exp}(\varepsilon)^2, \tag{4.17}$$

where $P^{mod}(\varepsilon)$, and $P^{exp}(\varepsilon)$ are the stresses (in MPa) corresponding to a strain ε in the simulation, and the experiment respectively. The total error ϵ was the output of the objective function to be minimised and was equal to the sum of the ϵ_{case} for all simulation cases. The tolerance criterion was set to 100 and took under 20 iterations to be completed.

4.5 Results and discussion

In light of the tests performed on D6 specimens in compression at dry, water saturated and intermediate wet states (Chapter 3), some of the experimentally obtained parameters can be correlated with the water content. Figures 4.4-4.6 show a common

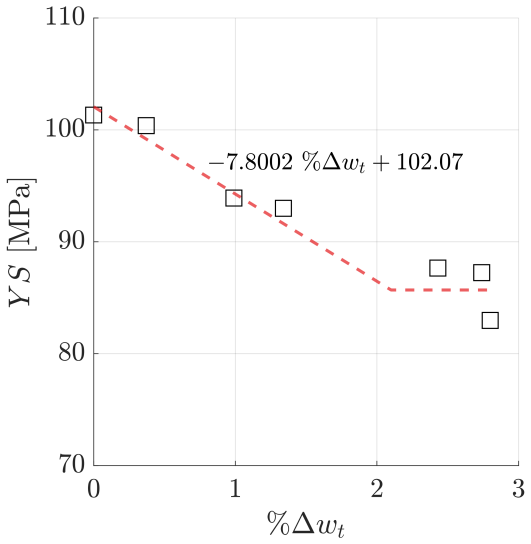

Figure 4.4: Evolution of YS at $0.001\,\mathrm{s}^{-1}$ with water content.

trend on some of the epoxy properties. As water content increases, there is an initial region of property evolution that is linear with respect to $\%\Delta w_t$. After $\%\Delta w_t \approx 2\%$, the properties seem to remain stationary. Similar trends have been observe in previous studies of epoxy resins [87].

Table 4.3 provides all the material parameters that were found from the experiments and the optimisation script described in Section 4.4. All parameters, except the Poisson's ratio, were different for every pre-conditioning scenario.

The lumped parameter A, proportional to the cube of the mean molecular radius a increases with water. This could be explained by the secondary links created by the interaction with water molecules [2] which increases the mean molecular radius. In addition, the pre-exponential factor $\dot{\gamma}_o$ also increases with $\%\Delta w_t$, indicating that water acts as a plasticiser, promoting the viscous flow of the bulk.

In the following plots, the absolute value of the compressive strains and stresses were used in order to appreciate in detail the effects of pressure. Figure 4.7 shows the results of compression and tensile simulations of the model with the optimised parameters. Simulation results are identified by the suffix "Sim" in the legend, while experimental curves by the suffix "Exp".

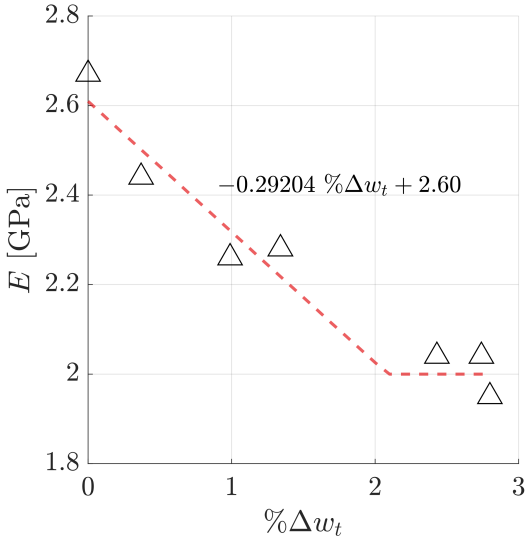

Figure 4.5: Evolution of E at $0.001\,\mathrm{s}^{-1}$ with water content.

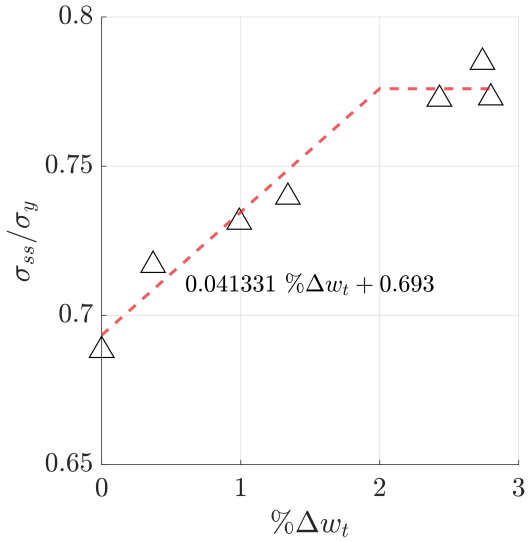

Figure 4.6: Evolution of $\frac{\sigma_s}{\sigma_y}$ at $0.001\,\mathrm{s}^{-1}$ with water content.

Table 4.3: Material parameters obtained from experimental measurements (Exp.) or by the optimisation script (Opt.) for various conditioning cases.

	Parameter	Units	*Dry* $\%\Delta w_t = 0\%$	*W-Sat* $\%\Delta w_t = 2.8\%$	$\%\Delta w_t = 1\%$	Obtained from
1	E_o	MPa	4210	2590	3400	Exp.
2	ν	-	0.4	0.4	0.4	Exp.
3	m	MPa·s	230	85	157	Exp.
4	s_o	MPa	120	91.7	105	Exp.
5	$\dot{\gamma}_o$	s^{-1}	$3.74 \cdot 10^{10}$	$1.48 \cdot 10^{12}$	$1.58 \cdot 10^{12}$	Opt.
6	A	mm^3	$2.07 \cdot 10^{-18}$	$3.44 \cdot 10^{-18}$	$2.86 \cdot 10^{-18}$	Opt.
7	$\frac{s_{ss}}{s_0}$	-	0.68	0.78	0.73	Exp.
8	h	MPa	480	754	528	Opt.
9	α	-	0.25	0.16	0.2	Exp.
10	N_l	-	3.24	5.55	6	Opt.
11	C_R	MPa	31.88	24.94	24.87	Opt.

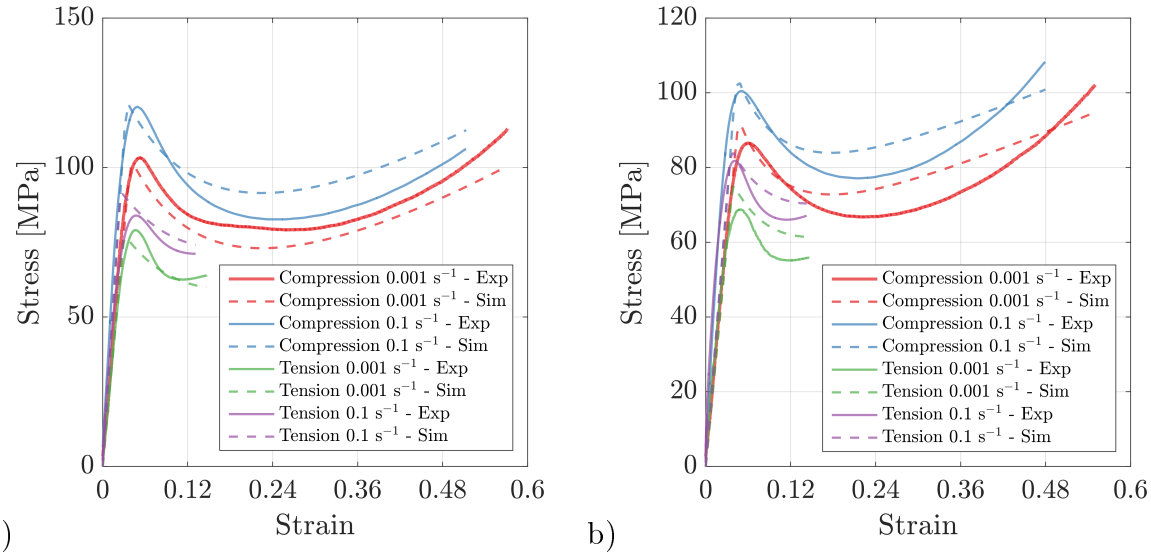

a) b)

Figure 4.7: Experimental and numerical results of the modified Arruda-Boyce simulations for a) Dry condition, and b) W-Sat condition.

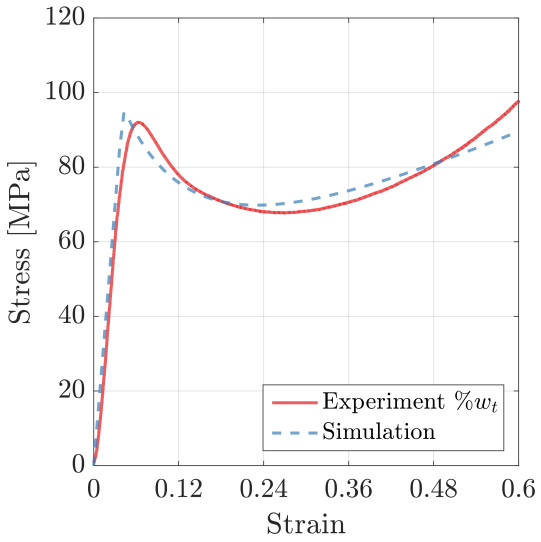

Figure 4.8: Simulation of the behaviour of a compression specimen with $\%\Delta w_t = 1\%$.

For $\Delta w_t = 1\%$, only compression data at 0.001 s^{-1} was available. Again, some of its parameters were obtained from the piecewise linear correlation (experimental), whilst others by optimisation running only the simulation case 2. There is not enough evidence to tell if parameters such as $\dot{\gamma}_o$ or A follow a similar linear trend. Additional experiments at intermediate wet states would be needed to draw such conclusions. The obtained parameters are also listed in Table 4.3 and the virtual experiment is displayed in Figure 4.8.

An issue that was not addressed in this study was the investigation into the effects of heterogeneity and the correlation of the local material properties to the local content of water as in [87, 22]. In this case, such heterogeneity comes from the gradient of water content in the bulk because after 29 hours of water immersion ($\%\Delta w_{t=29\,h} = 1\%$), the gradient of water content goes from 2.8% in the outer surface, to 0.002% in the volumetric centre of the specimen.

4.6 Conclusions

In this chapter, an existing VUMAT Abaqus subroutine was modified to account for strain rate dependent elasticity. In addition, it was investigated how parameters change with water content. The constitutive material parameters were identified and calculated for a fully Dry, fully saturated specimens, and one intermediate state.

The main conclusions to draw from this Chapter are:

- It was possible to tune the Arruda-Boyce model to implement a phenomenological strain rate dependent linear elasticity.
- The Arruda-Boyce model can capture the behaviour of polymers with different water content.
- Parameters such as E_0, m, s_0, s_{ss}/s_0 can be modelled with a piecewise function initially linear up to a water content of $\%\Delta w_t = 2\%$, followed by stabilisation of the material parameter.
- Other material parameters do not necessarily follow a piece evolution law. Additional experiments would be needed to perform a more detailed characterisation, with more intermediate states, and less heterogeneity.

Chapter 5

Effects of water immersion and strain rate on E-glass fibres

This chapter explores the effects of water and salt water upon the quasi-static and high rate performance of E-glass fibres. Single fibres and bundles of approximately 2600 filaments, were immersed in water and salt water at 50°C and tested at strain rates from $0.001 - 600\,\mathrm{s}^{-1}$. Single fibre tests revealed that after 24 hours of water immersion there was not statistically significant change in the value of the quasi-static strength across the different preconditioning scenarios. Tests of fibre bundles suggested that the modification of the interface between the fibres due to pure water immersion caused an irreversible decrease of 22% in the measured bundle strength.

In addition, a novel experimental technique called Sound Measurements was used to generate a set of effective values of strength for glass fibres within a bundle. This technique relies on the ability to capture the sound emitted when fibres break. The virtual experiments showed that not only did this methodology provide a more accurate representation of the features observed in the mechanical test, but also a better coefficient of determination R^2 in relation to the Weibull approach.

5.1 Introduction

5.1.1 Mechanical characterisation of fibres

The study of fibres is of great importance because they are the constituents that most contribute to the strength and stiffness of fibre reinforced composite materials. In fact, the severity of the degradation induced by water absorption on composites can be determined by the fibres [119]. Therefore it is important to characterise the effects of wet environments on neat glass fibres.

Silica glass fibres can have their properties affected by several factors such as temperature [35, 37], strain rate [31, 30, 33], and interaction with water whether as moisture or liquid water. Mould showed that water interaction decreases the static fatigue strength of glass, and that liquid water is actually more detrimental than relative humidity [120]. Kurkjian and Mathewson observed a decrease of 25% in the strength of a fused silica optical fibre after 2.3 days of pure water immersion at 100°C [121, 122]. A similar effect was also found after nine years of exposure to water at 25°C. From those observations, they suggested that it was possible to make an equivalent between accelerated lab conditioning (at elevated temperatures), and ageing at room temperature or under real work conditions, by relating the activation energy. They calculated an activation energy of around 90 kJ/mol which corresponds to the $SiO_2 + H_2O$ reaction. Kurkjian *et al.* reported that fibre coatings can decrease the water induced degradation in silica and silica-germanium optical fibres [121].

Brown *et al.* reported a decrease in strength of E-glass fibre bundles after water immersion, and less severe strength drops for fibres exposed to humid environments (10%, 40%, 80% RH) [123]. However, fibres sized with epoxy resin, seemed to be more resistant to degradation. Cameron investigated the effects of environmental humidity upon the strength of E-glass [69]. In his study, glass fibres subjected to vacuum increased their strength as a function of the preconditioning time and testing temperature. This suggested that vapour adsorbed by the glass fibre had more neg-

ative effects than the humidity in the environment. Mišíková *et al.* reported leaching of some elements like Mg ,Al, and B, in unsized borosilicate E-glass fibres immersed in distilled water at 50, 70 and 90°C [124].

Although most surveyed literature has shown detrimental effects of water upon the mechanical performance of glass and certain types of glass fibres, there are also studies in which the opposite effect has been observed. For instance, in the case of surface abraded glass, Mould [120] observed an increase in the liquid nitrogen strength of $30 - 60\%$ depending on the abrasion method. The mechanisms of strengthening could be explained by blunting of existing crack tips [125] or by swelling of the material leading to compressive stresses around the crack tip that act as reinforcement [126].

Few instances in the reviewed literature have explored the consequences of water and salt water immersion of E-glass fibres, the most widely used fibre for reinforcement [31]. All the studies presented above are concerned with the consequences upon either pure glass, single glass fibres, or bundles individually. No study in the surveyed literature investigates the effects of water and salt water immersion on single fibres and how they reflect upon their bundles. In addition, it is not yet clear what the impact of water immersion is on the dynamic properties of fibres.

5.1.2 Modelling techniques and sound measurements

The classic approach to studying and modelling the mechanics of fibre bundles consists of randomly generating a distribution of strengths and assigning them to each fibre. This distribution can be normal [127], or the more frequently used Weibull [128, 129, 130]. The non-interacting parallel fibres in the bundle should break in a stable manner and have a smooth bell-shaped strain vs. load curve when pulled in a strain-controlled mode manner [130]. However, due to imperfections of the material, misalignment of fibres, unequal fibre radii, inter-fibre interaction, and defects introduced during the manufacture of specimens, the aforementioned distributions may not follow accurately a real test.

Acoustic emissions (AE) is now a well-accepted technique to capture failure events. Its work principle is simple: transmitted stress waves are measured by a piezoelectric sensors capable of capturing frequencies up to 1 MHz. It has been applied to a wide range of material such as metals [131], granular materials [132, 133], composites materials [134], and fibres [135, 136]. Regardless of this wide field of applications, there are still some drawbacks to using AE. For example, in granular materials the size of the probes can be relatively large when compared to RVE volumes of few millimetres. For application with fibres, probes are attached to the machine near the specimens [137], which are usually fibre bundles glued onto lining plates. Since AE captures transmitted waves, the solids between the event source and the probes can induce noise, attenuation, and alteration of the waves. Therefore, the actual captured signal contains characteristics that cannot be intrinsically related solely to the acoustic phenomenon of the fracture event, but also to the properties of the intermediate solids. This may not affect the detection of breaks, but may have an impact upon the analysis in the frequency domain. Moreover, AE does not allow for a clear distinction between events generated by failure events and those coming from friction between surfaces.

It is proposed that with the aid of the Sound Measurements (SM) [138] inspired by acoustic emissions (AE), a distribution of strengths can be found for the individual fibres that can lead to a more accurate representation of the mechanical behaviour of the bundle. It is assumed that all imperfections will have an effect upon the "apparent strength" of the single fibres within the bundle. The apparent strength is not the real strength of the material, but an effective one, that accounts for the defects such as non-parallelism, manufacture, *etc.* These apparent strengths can be found thanks to the fact that SM is exclusively sensible to fracture [138]. Therefore, the number of surviving fibres at a certain load, at any time, can be estimated. Additionally, the sound waveform can be analysed in the frequency domain, to reveal some main frequencies related to the breakage of glass fibres.

5.2 Experimental methods

5.2.1 Material description

Fibres bundles were manually extracted from the sized E-glass multiaxial fabric Formax FGE238. This fabric is made of *tex* 1200 fibre bundles oriented at 90° (94.7% of the total fabric weight), and 0° oriented *tex* 300 bundles (5.3% of the weight), and texturized polyester stitching the bundles to keep them together. Single filaments were carefully extracted from the bundles by hand. Unfortunately, no information of the exact sizing agent was found.

The *tex* number denotes the mass of 1000 meters of bundle length expressed in grams, hence:

$$tex = 10^{-6}\rho_g \sum_{i=1}^{n_f} A_i, \tag{5.1}$$

where ρ_g is the density of E-glass in kg/m^3, A_i is the area of the i^{th} fibre in m^2, and n_f is the total number of fibres in the bundle. From Equation 5.1, and considering all fibres to be of equal diameter D_f, the number of fibres within a bundle can be estimated with Equation 5.2.

$$n_f = \frac{4 \cdot 10^{-4} \cdot tex}{\pi \cdot D_f^2 \cdot \rho_g} \tag{5.2}$$

The diameter of 28 single fibres were microscopically measured in an Alicona InfiniteFocus, obtaining values ranging from $13-17\,\mu$m with an average $D_f = 14.63\,\mu$m. The density of E-glass is $\rho_g = 2550\,$kg/m^3 [139], hence from Equation 5.2 $n_f = 2680$ fibres.

5.2.2 Water immersion

The time to reach saturation in a $14.6\,\mu$m fibre was estimated with an finite element simulation. Assuming Fickian diffusion and a value of diffusivity taken from [140],

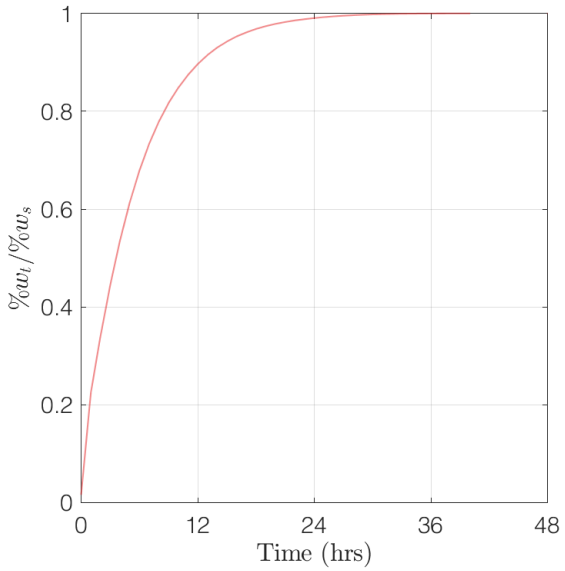

Figure 5.1: Water absorption in a single fibre.

simulation results showed that 24 hours should guarantee over 99% saturation of the 14 μm diameter fibres (Figure 5.1).

Both single fibre and bundle specimens were tested as they were extracted from the raw material (AM), and after exposure to other 5 different types of conditioning environments. Specimens were firstly placed in the oven for 24 hours at 50°C and tested in the "Dry" condition.

Dry samples were divided in two groups and immersed in two separate water baths for 24 hours: one with pure distilled water at 50°C (W-Wet), and another bath with a salt solution of 18 g of salt per 100 ml of water (SW-Wet).

Finally, after immersion, specimens were "re-dried" in the oven at 50°C for 24 hours (W-RD and SW-RD for re-drying after pure and salt water respectively).

A summary of the types of conditioning scenarios is shown in Table 5.1. The time for handling and testing of the specimens was never longer than 10 minutes.

At least 4 specimens per type of preconditioning were tested. The scattered data and their corresponding box plots are reported in the next section. A multiple one-way analysis of variance (ANOVA) will tell, with 95% confidence, if the conditioning

Table 5.1: Preconditioning environments.

Type	Description
AM	As extracted from the raw material
Dry	After 24 hours in the oven at 50°C
W-Wet	Dry+24 hours pure water immersion
SW-Wet	Dry+24 hours salt water immersion
W-RD	W-Wet + 24 hours in the oven at 50°C
SW-RD	SW-Wet + 24 hours in the oven at 50°C

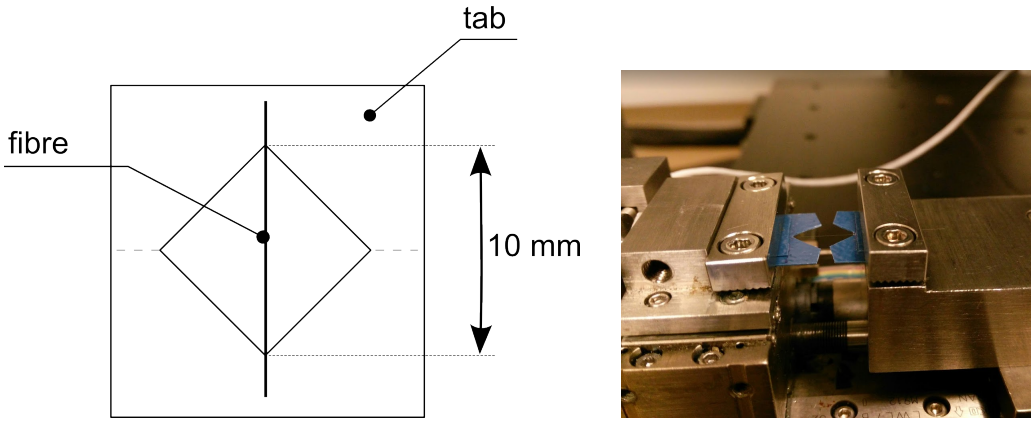

Figure 5.2: Single fibre specimen and test setup.

environments actually induced detrimental effects upon the strength of the single fibres and the bundles.

5.2.3 Single fibre tests

Single fibre specimens of gauge length 10 mm were manufactured as per recommendations of the standard ASTM C1557 [141]. They were glued onto protective plastic tabs previously prepared with central cut as illustrated in Figure 5.2. After fixing the specimen with the metallic grips of the rig, the tabs were cut across the side dashed lines.

Specimens were tested in the Deben UK micro-tensile rig mounted with a 20 N load cell with a crosshead speed of 1 mm/min. The relative displacements between the grips were measured with the machine built-in linear scale.

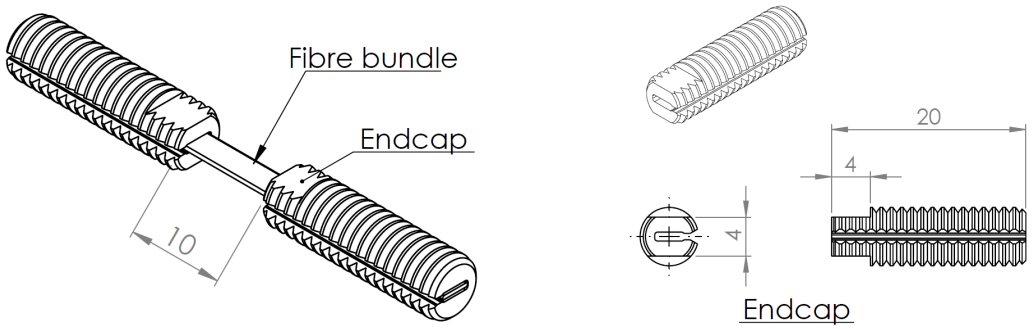

Figure 5.3: Fibre bundle specimen.

5.2.4 Fibre bundle tests

The specimen design of fibre bundles involves several challenges. Clamping shoulders should ensure that the strain is the same for all fibres, and that mounting on the testing rig can be done with ease. The proposed design consisted of a bundle inserted into aluminum endcaps with slots to insert those bundles. Slots, cut with electric discharge machined, were designed with a profile that allowed for an easy insertion of the bundles and for enough volume to be filled with glue. In addition, the endcaps had a flat surface, near the ends of the gauge section. They could be utilised to either to stick reflective tapes to be used with a laser extensometer or to paint a speckle pattern to perform DIC analysis. The details and dimmensions of the endcaps can be see in Figure 5.3.

The procedure to prepare the specimen was as follows. Epoxy-based adhesive 3M DP460 was injected with a syringe inside the endcap slot. Afterwards, the bundle was slowly inserted to keep the overflow of the adhesive to the minimum. The bundle is left to dry with one endcap on a specially designed support. After drying, the second endcap is glued repeating the procedure. The viscosity of the chosen adhesive is very important because if it is too fluid, capilarity effects would make the glue go in between the fibres in the gauge section.

For quasi-static and high strain rate tests, E-glass bundles of *tex* 1200 were glued into the threaded aluminium endcaps. The same gauge length of the single fibre

specimens (10 mm) was chosen to prevent length effects [142, 30] when comparing the responses of single fibres and fibre bundles.

Quasi-static experiments were performed in the universal testing machine Zwick Z250 instrumented with a load cell of 20 kN and an imposed crosshead speed of 0.01 mm/s. Reflective tapes were stuck to the flat surface of the endcaps, near the specimen, to track relative displacement with the laser extensometer EIR-L05 of 1 μm resolution.

High strain rate experiments from $150 - 400$ s^{-1} were performed in a tensile Hopkinson bar with setups similar to the ones used in previous studies [18, 101, 102] (Figure 3.6b). The titanium solid input bar and the hollowed aluminium output bar were instrumented with two and one set of strain gauges respectively. The time history of stresses was calculated with one-dimensional wave theory as in Chapter 3. The history of strains was calculate by Digital Image Correlation (DIC) analysis, using the high-speed photographies taken at 250000 fps with the camera Kirana from Specialised Imaging. The speckled areas (prepared on the flat surfaces of the endcaps) were tracked with the DIC Matlab code written by Eberl *et al.* [143]. Dynamic equilibrium was reached after approximately 450 µs, with approximately constant strain rate afterwards.

Assuming that an applied load F is equally distributed among all fibres within the bundle with a total cross sectional area of $\sum_{i=1}^{n_f} A_i$ (see Equation 5.1), the nominal value of the stress σ is calculated with Equation 5.3.

$$\sigma = \frac{F \cdot \rho_g \cdot 10^{-6}}{tex}, \tag{5.3}$$

where σ is the resulting stress in Pa, and F is the applied force in N. This expression will be used to report the stresses in the rest of this Chapter. This value is only nominal as it does not take into account the reduction of effective area due to fibre breaking.

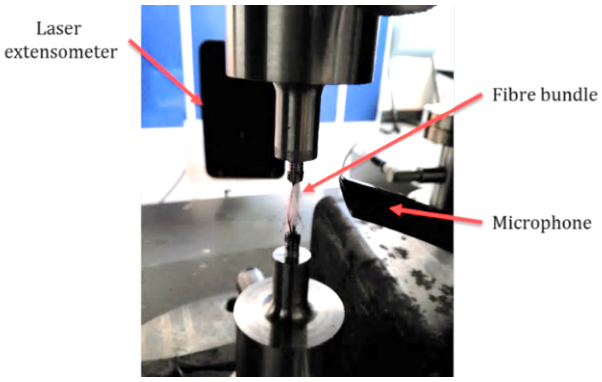

Figure 5.4: Experimental setup for the SM technique.

5.2.5 Sound measurements

To implement this technique, the only addition to the setup described in 5.2.4 was a microphone Plantronics Audio 300 (Figure 5.4), which is a conventional PC microphone with an electret capsule. The sound emitted by the breakage of fibres was acquired through the PC audio card and the software Audacity 2.1.3 [144] at a rate of 96 kHz. Calibration tests were run to set the acquisition gain, to obtain signal levels sensitive to the noise produced by fibre breakage, and to prevent signal saturation. Since sound is acquired with set internal gain parameters in the software, no physical units can be assigned to the recorded waveform. However, this is not a problem as the only quantitative calculations are the counting of events. Post de-noising was performed on the audio signal to reduce the environmental sound and improve the signal to noise ratio (SNR). This was done with a built-in function of Audacity, which makes use of the spectral noising gating [145].

An SM event is herein defined as the portion of the sound signal of 5 ms duration that contains a peak above a chosen threshold A_t. The choice of 5ms as the SM event duration comes from a calibration test with a single fibre. Signals in this study were analysed with a threshold that is a fraction of the maximum signal amplitude A_m: $A_t = 0.02 \cdot A_m$. The acquired waveform was post-processed in Matlab 2014a [146] to identify the SM events, that are associated with the breakage of individual fibres. In this way, it was possible to evaluate the cumulative number of SM events, or the

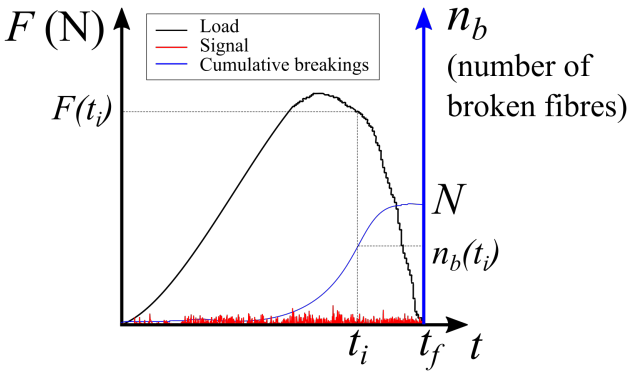

Figure 5.5: Typical experimental data: history of load $F(t)$, sound waveform, and cumulative number of SM events.

total number of broken fibres $n_b(t)$.

Figure 5.5 shows typical experimental data in the time domain: the sound signal waveform, the load history during the test $F(t)$, and the cumulative number of SM events n_b which reaches a maximum value N. Whenever a peak that meets the prescribed criterion is found, the time t_i of an SM event occurrence can be identified. Let n_f be the total number of fibres in the bundle, and $n_b(t_i)$ be the number of broken fibres at time t_i. The tensile strength TS_i of the fibre breaking at time t_i can be calculated from the load $F(t_i)$ acting on the total area of the surviving fibres:

$$TS_i = \frac{F(t_i)}{(n_f - n_b(t_i)) \cdot A_f} \tag{5.4}$$

After complete breakage of the bundle at $t = t_f$, it would be expected that $n_b(t_f)$ takes the value of the total number of fibres of the bundle n_f. Nevertheless, that is not the case due to distinct reasons such as simultaneous breakages, and the arbitrary way to pick the threshold A_t. Instead, $n_b(t_f)$ is equal to N, which can be smaller than n_f, depending on the chosen amplitude threshold A_t.

The calculation of the apparent strengths of the fibres will rely on the assumption that the total number of fibres within the initial bundle are N instead of n_f. The diameter D_f of the fibres (of area A_f) is then re-scaled to D_f^* (for fibres of area A_f^*) to keep the total cross sectional area of the bundle constant (see Eqs 5.5 and 5.6).

Thus, the apparent tensile strengths for the N equivalent fibres in the bundle can be computed with Equation 5.7.

$$A_f^* = \frac{A_f \cdot n_f}{N} \tag{5.5}$$

$$D_f^* = D_f \sqrt{\frac{n_f}{N}} \tag{5.6}$$

$$TS_i = \frac{F(t_i)}{(N - n_b(t_i)) \cdot A_f^*} \tag{5.7}$$

All SM events were also studied in the frequency domain. Their power spectral density (PSD) was estimated with the periodogram built-in function of Matlab [147]. The PSDs were then then normalised with respect to their respective maximum value of energy. The energy peaks above 0.5 in those normalised PSD plots, were related to the main frequencies and will be a topic of later discussion.

To be able to distinguish frequencies coming from fracture events from those coming from the loading equipment and background noise, the frequency-time distribution [148, 149] was plotted. This kind of diagram provides an overview of the frequencies of the signal and their associated energies along the recording time.

5.3 Modelling framework

The simpler analytical models of fibre bundles consider that there is no interaction of any kind among fibres, and that each of them breaks as soon as its strength is attained. To model this behaviour, a Weibull distribution of strengths is assigned to the fibres within the bundle. It has been found convenient for its mathematical simplicity and good agreement with experimental observations [32, 35]. The Weibull distribution of strengths has a cumulative function as shown in Equation 5.8. Some modifications to this distribution have been proposed to include effects of temperature, and strain

rate [35, 37].

$$F(\sigma_w) = 1 - \exp\left(-\left(\frac{\sigma_w}{\sigma_o}\right)^{\beta}\right), \tag{5.8}$$

where σ_w is the strength of a single fibre, σ_o is the scale factor, and β is the shape factor of the distribution. These two parameters, and a number of values to generate, are enough to fully describe and to generate a non-unique distribution of strengths with the Matlab function wblrnd [150].

The shape and scale factors can be obtained in several ways from the experimental strain vs. stress curve. For instance, Yuanming *et al.* [32] proposed Equations 5.9, and 5.10 to compute the shape and scale factors.

$$\beta = -ln\left(\frac{\sigma_{max}}{E \cdot \epsilon_m}\right), \tag{5.9}$$

$$\sigma_o = \beta^{-\beta} \cdot \epsilon_m \cdot E, \tag{5.10}$$

where σ_{max} is the maximum stress measured during the experiment at a strain ϵ_m, and E is the elastic modulus.

The numerical experiment was implemented in Matlab R2014b [146]. It considers n_f parallel fibres of the same diameter pulled uniaxially in a strain-controlled manner (Figure 5.6). The computer program starts by generating values of strength for every fibre according to the case of study:

- Case 1: Weibull distribution of strengths to $n_f = 2680$ fibres. The distribution will be created with the parameters obtained from experiments for all types of conditioning according to Equations 5.9 and 5.10; or
- Case 2: A model for $n_f = N$ fibres with strengths calculated with the proposed SM technique. This numerical experiment will be run only for the AM conditioning, to show the applicability of the SM technique in the study of fibre

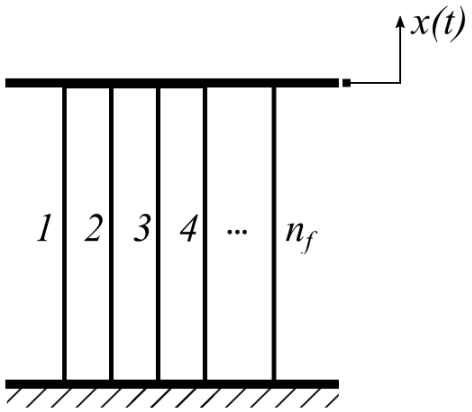

Figure 5.6: Numerical experiment where non-interacting parallel fibres are pulled.

bundles.

In every strain iteration of the program, the load within every single fibre is computed, and if the strength is reached, the breakage is reproduced by setting their modulus to zero to stop contributing to the load carrying capacity.

5.4 Results

Regardless the conditioning of the specimens, all single fibres and bundles exhibited typical strain stress curves as shown in Figure 5.7. The mechanical response of single fibres was perfectly elastic, with a sudden failure. Fibre bundles, on the other hand, showed progressive failure after a maximum value of stress.

5.4.1 Single fibres

In Figure 5.8, the tensile strengths (TS) of single fibres are displayed. The values of strength for AM fibres are in agreement with the ones reported for E-glass by other authors [33]. Also, the observed scatter in the tensile strength is characteristic of brittle fibres [151]. The average TS in the AM condition was 1.71 GPa. However, as it could be argued that this value might not be statistically meaningful because of the small number of tests, 29 other AM specimens were tested, obtaining 1.77 GPa

a) b)

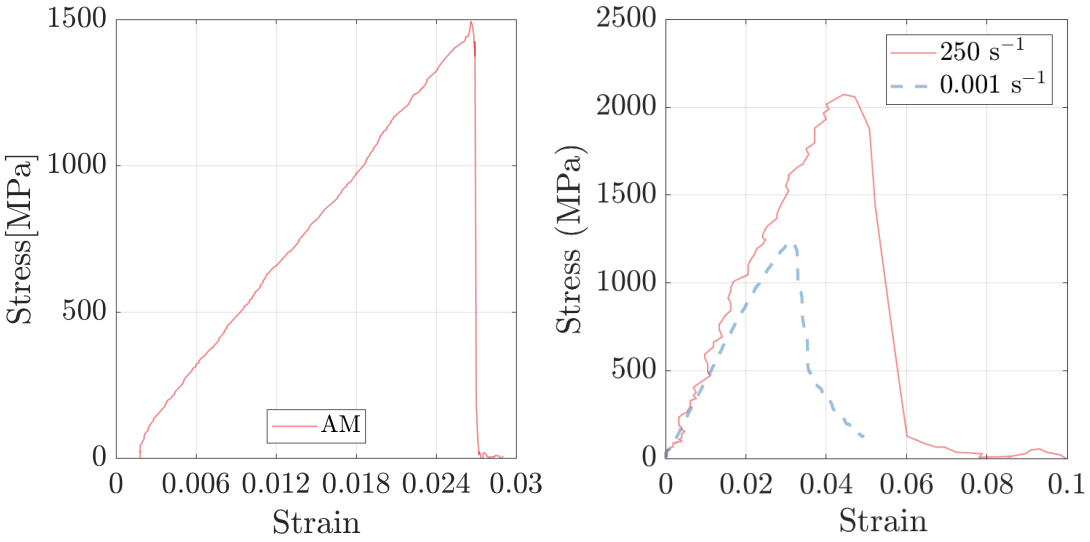

Figure 5.7: Typical curves in a) Single fibre tests and b) Bundle fibres experiments.

Table 5.2: ANOVA results for comparison of the single fibre strength of AM specimens with treated specimens.

	LLI	Mean difference	ULI	$p-$value
AM / Dry	-0.7407	-0.2102	0.3203	0.8205
AM / SW-RD	-0.7284	-0.1743	0.3798	0.9221
AM / SW-Wet	-0.7931	-0.2055	0.3823	0.8842
AM / W-RD	-0.5332	-0.0027	0.5278	1
AM / W-Wet	-0.7095	-0.1218	0.4659	0.9866

as the mean strength, in good agreement with the mean of the 4 filaments initially tested.

A multiple one-way ANOVA was run to compare the average of the AM fibre strength with the other cases. Results are shown in Table 5.2. The second and fourth columns are the lower and upper limits of the 95% confidence interval (LLI and ULI respectively). The third column is the difference between the mean value of the groups under comparison.

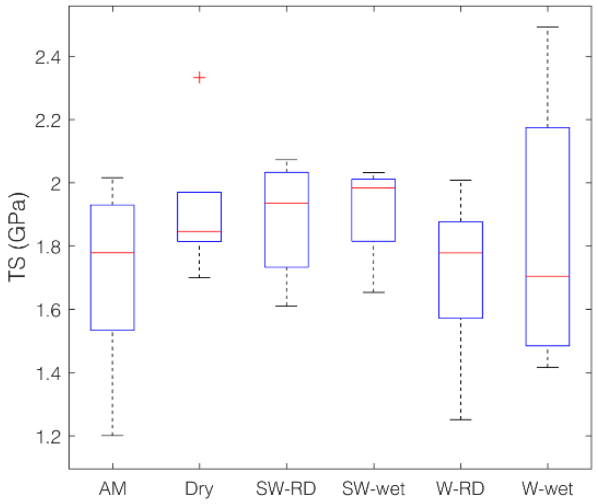

Figure 5.8: Strength of fibres after exposed to various conditioning environments.

Table 5.3: ANOVA results for multiple comparison of the AM mean strength of fibre bundles.

	LLI	Mean difference	ULI	$p-$value
AM / Dry	-0.2323	-0.0113	0.2097	1
AM / SW-RD	-0.0785	0.1425	0.3634	0.3593
AM / SW-Wet	-0.1856	0.0353	0.2563	0.9953
AM / W-RD	0.0285	0.2495	0.4705	0.0215
AM / W-Wet	0.0545	0.2755	0.4964	0.0098

5.4.2 Fibre bundles

Strengths of fibre bundles are normally smaller than the ones of single fibres due to various factors such as the statistical distribution of the strength, load sharing, fibre alignment, inter-fibre friction, *etc.* The quasi-static strength of fibre bundles after exposure to the different preconditioning environments are displayed in Figure 5.9. The results of the one-way ANOVA are shown in Table 5.3.

The strengths of fibre bundles at strain rates of up to 600 s^{-1} are presented in Figure 5.10. A consistently increasing strength was observed with higher strain rates at all preconditioning states.

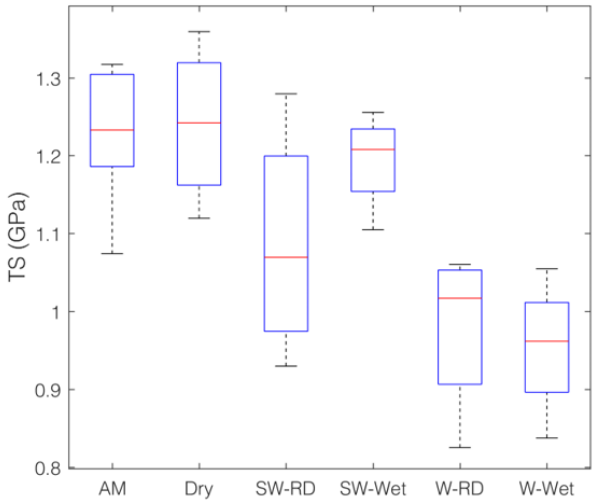

Figure 5.9: Bundle strength of fibre bundles after exposure to all preconditioning environments.

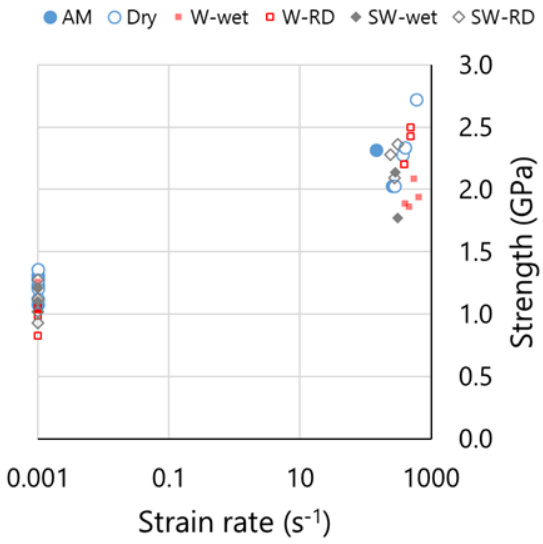

Figure 5.10: Strength of bundles at various strain rates and preconditioning environments.

Table 5.4: Quasi-static Weibull parameters of fibre bundles.

	β	σ_o
AM	8.05	$1.91 \cdot 10^9$
Dry	9.11	$1.71 \cdot 10^9$
SW-RD	6.36	$1.75 \cdot 10^9$
SW-Wet	10.94	$1.51 \cdot 10^9$
W-RD	10.27	$1.14 \cdot 10^9$
W-Wet	20.57	$1.18 \cdot 10^9$

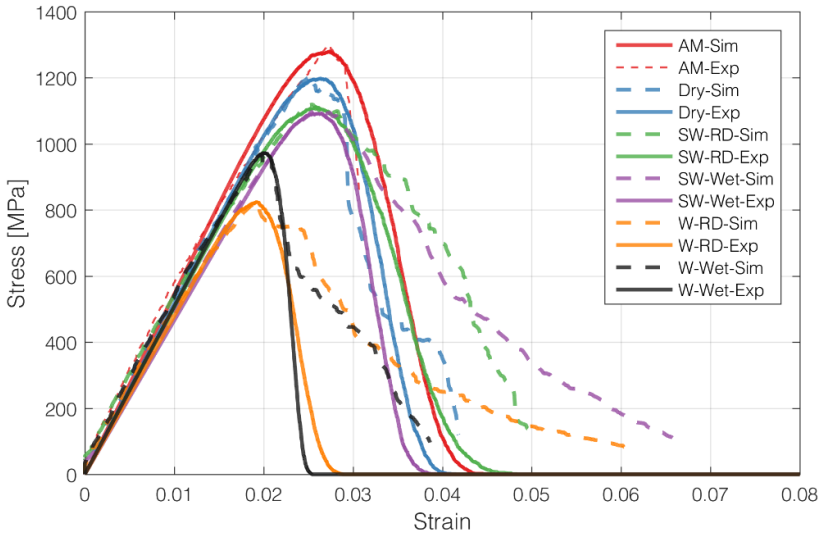

Figure 5.11: Experiments versus simulations with the Weibull model at all preconditioning states.

5.4.3 Weibull model

Table 5.4 shows the Weibull parameters obtained from the Equations 5.9 and 5.10. For all conditioning environments, the simulated tests (with suffix Sim in their label) and their correspondent experimental curves (with suffix Exp in their label) are shown in Figure 5.11.

5.4.4 Sound measurements

The sound measurement analysis was run with a threshold A_t of 2% of the maximum signal amplitude. As a result, 800 SM events were identified across the whole waveform as shown with circular markers in Figure 5.12. The cumulative number of

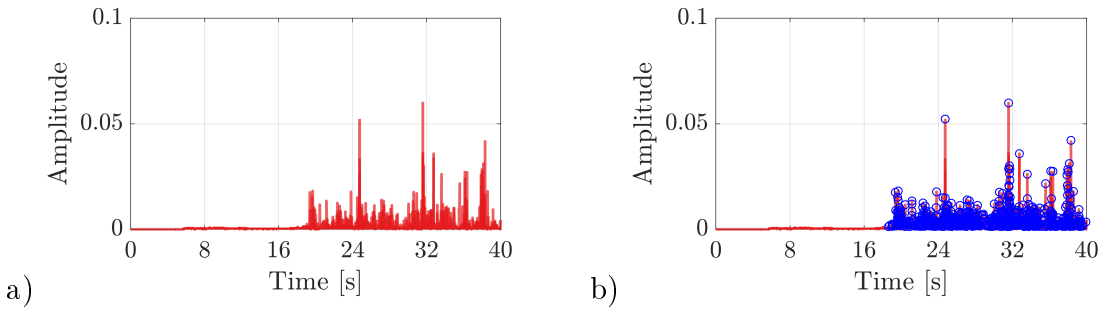

Figure 5.12: a) Raw Sound signals and b) SM events detected in the sound waveform.

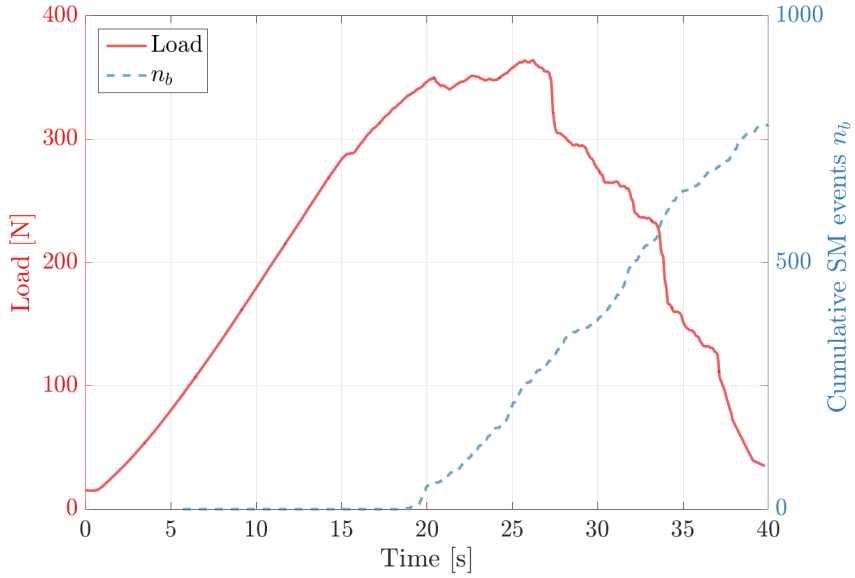

Figure 5.13: Time history of the cumulative number of breaks and load.

broken fibres is plotted in Figure 5.13 along with the time history of load during the test.

In the model, $N = 800$,and $n_f = 2680$ are substituted in Equations 5.5, 5.6 and 5.7 to obtain the distribution of apparent strengths.

Figure 5.14 pictures the results of the numerical experiment using Weibull and the SM technique.

Results of the frequency post-process of the sound waveform are displayed in Figures 5.15-5.18. Figure 5.15 shows the time frequency distribution of the acquired sound signal. Figure 5.16 shows four signals corresponding to the 1^{st}, 200^{th}, 400^{th}, and 650^{th} SM event. Their normalised PSD curves are displayed in Figure 5.17. All

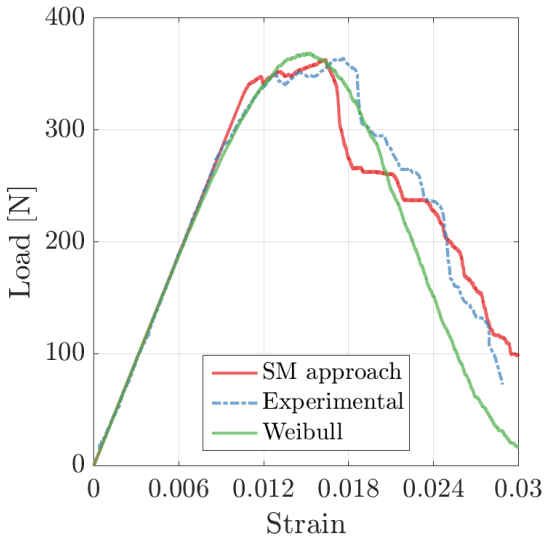

Figure 5.14: Simulation of numerical experiments: case 1 (Weibull Distribution), and case 2 (SM apparent strengths).

the main frequencies of the 800 SM events, as defined in Section 5.2.5, are plotted in Figure 5.18, where the vertical axis is the event number (in ascending order), and the horizontal axis corresponds to the main frequencies. The markers used in the plot have transparency and sometimes overlap, which means that darker regions contain a higher concentration of main frequencies.

5.5 Discussion

5.5.1 Effects of pure and salt water exposure

The minimum p-value obtained in the ANOVA of single fibre strengths is 0.8205 (Table 5.2), which means that, with 95% confidence, there is no influence of the conditioning environments upon the strength of the single fibres. Water immersion for one day may not have been long enough to observe clear detrimental effects similar to the ones observed in previous works [121, 122]. However, the water bath places the fibres in an environment already more extreme than within the composite, where it would actually be surrounded by a water saturated resin matrix only. Another

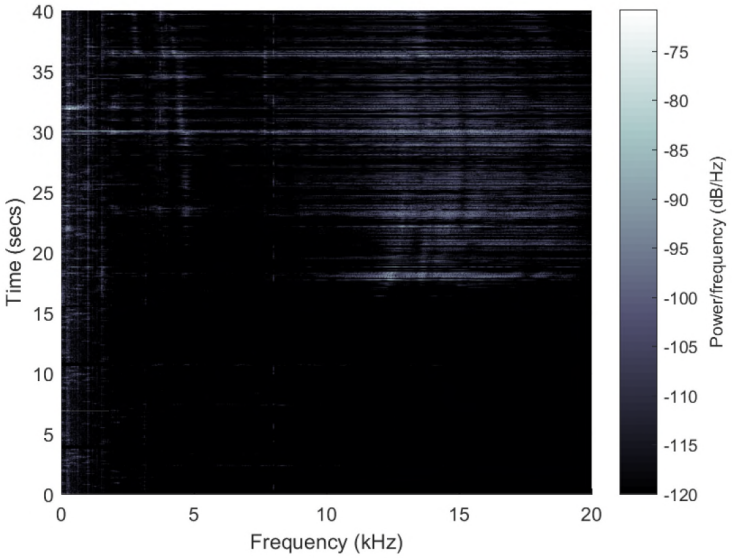

Figure 5.15: Time - Frequency distribution of the sound acquired during the test.

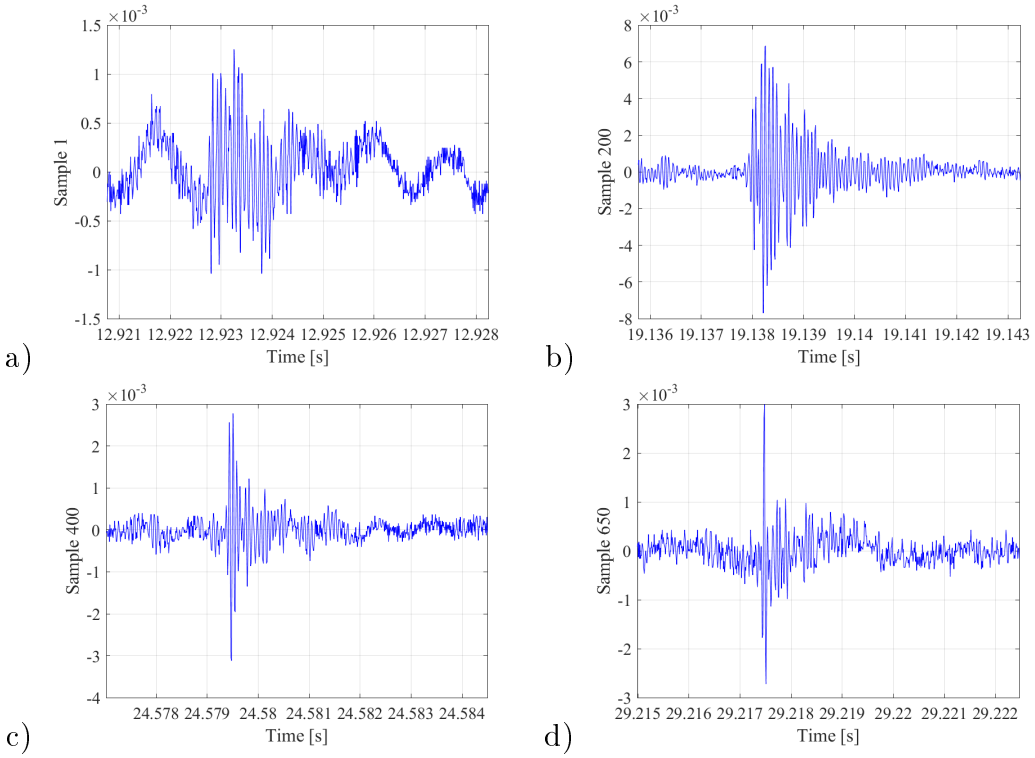

Figure 5.16: Four samples of SM events in the time domain: a) 1^{st} SM event, b) 200^{th} SM event, c) 400^{th} SM event, and d) 650^{th} SM event.

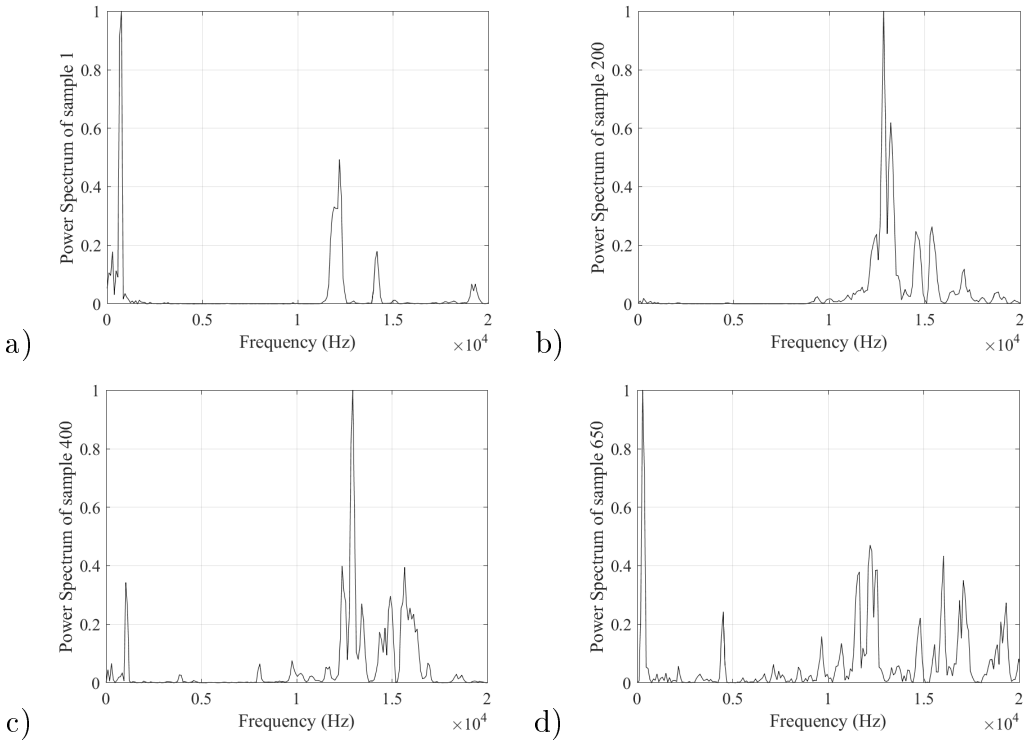

Figure 5.17: Normalised PSD of the events: a) 1^{st} SM event, b) 200^{th} SM event, c) 400^{th} SM event, and d) 650^{th} SM event.

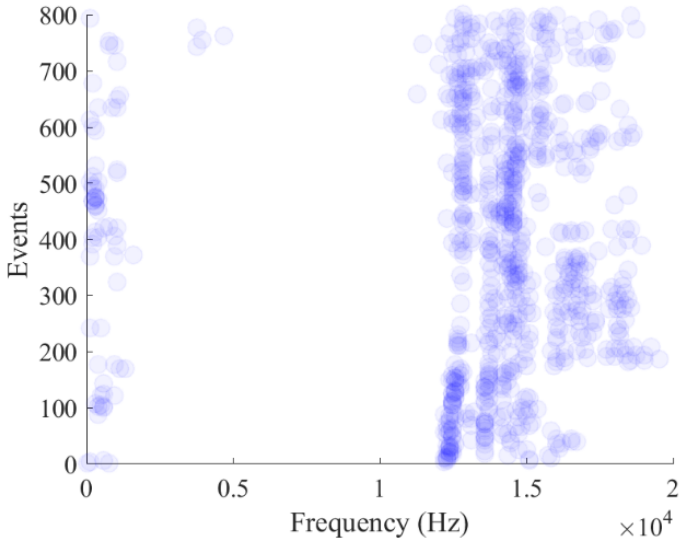

Figure 5.18: Main frequencies of all SM events.

factor that could have prevented us from observing clear detrimental effects in the single fibres, is the sizing protection. Sized fibres were used during the presented experimental campaign to make use of fibres in similar conditions to those which are within the composite.

The results of the ANOVA of fibre bundles, shown in Table 5.3, suggests with 95% confidence, that the only groups with strength different than the AM group, are the specimens with treatment W-RD and W-Wet (small p-values of 0.0215 and 0.0098 respectively). Despite single fibres being indifferent to water immersion, there is a clear negative effect of water conditioning upon the strength of fibre bundles (respectively, 22% and 20% decrease in W-Wet and W-RD with respect to AM).

If the presence of water in between the fibres acted as a lubricant, lowering the friction in between fibres, it would lead to a modification of the bundle strength. The effects of lubricants in E-glass fibre bundles were investigated by Hill and Okoroafor [135], who reported 14.6% higher strength in lubricated fibre bundles due to the decrease of inter-fibre friction. Contrarily to those observations, in this study water exposure decreased the value of the tensile strength, suggesting no decrease of the inter-fibre friction. In addition, if water in between fibres were responsible of this decrease, the detrimental effect should be reversible by the post-drying procedure. However, the tests on the W-RD specimens did not reveal any recovery of the strength. A possible explanation for this might be that the lateral surfaces of the fibres, covered by the sizing material, are permanently modified due to pure water exposure. Thus, the damage in the sizing would cause an increase of the inter-fibre friction, which would explain the drop in strength in fibre bundles exposed to pure water. For single fibres, sizing damage would not have any effect on the strength because sizing does not have any contribution upon the single fibre strength [129], which is in agreement with the observation in single fibre experiments. A note of caution is due here since the same effect was not observed in the bundles immersed in salt water (SW-wet and SW-RD).

5.5.2 Effects of strain rate

Figure 5.10 shows the strain rate dependency of fibre bundles. Results are in line with observations of previous reports [31, 30, 33]. A consistently increasing strength was observed with higher strain rates at all preconditioning states. The effects of preconditioning, however, are not entirely clear due to the scattered data at high strain rate, but W-wet specimens exhibited the lower values of strengths at all strain rates.

The effect of water immersion at different strain rates seems to be similar at different strain rates. For example, at 0.001 s^{-1} there is a reduction of 23% in the W-Wet strength with respect to the Dry condition; at 400 s^{-1}, this drop is 22%.

5.5.3 Weibull model in fibre bundles

The simulations shown in Figure 5.11, suggest that after the maximum load is attained, the model tends to underestimate the load, particularly for the cases in which there was pure or salt water treatment (W-wet, SW-wet, W-RD, SW-RD). Hill and Okoroafor [135] recommended special care when applying the Weibull model in the region after the maximum load. Due to friction, broken fibres can still contribute to the stress. This effect is ignored by the model, underestimating the load after a significant amount of fibres have broken. When fibres are exposed to wet environments, a modification of the interface, irreversible with re-drying, can lead to a change in friction due to sizing damage.

With respect to the Weibull parameters, it can be observed in Table 5.4, that the scale factor σ_o is smaller and the scale factor β is larger in those specimens with water treatment W-Wet, W-RD, SW-Wet.

5.5.4 Sound measurements and apparent strengths

Qualitatively, in Figure 5.14, simulations with the apparent distribution of strengths provide a virtual test with more "realistic" features such as ups and downs in the strain vs. load curve. To quantify how close the 2 study cases are to the experimental curve, a residual can be defined as:

$$e(\epsilon) = (F_{model}(\epsilon) - F_{exp}(\epsilon))^2, \tag{5.11}$$

where $F_{exp}(\epsilon)$ is the load at the strain ϵ measured in the experiment, and $F_{model}(\epsilon)$ is the load at the same given strain for either the model based on the Weibull distribution or the one that considers the apparent distribution of strengths found with the SM technique.

The residual is plotted with respect to the strain in Figure 5.19. It is evident that the SM-obtained apparent distribution of strengths does not only provide an input for the model that leads to qualitatively better results, but also provides an output quantitatively closer to the real measurements. The coefficient of determination R^2 was computed between experimental curve, and the Weibull and the SM Apparent distribution models, obtaining 0.9102, and 0.9608 respectively. Thus, confirming the improvements of the model when relying on SM obtained apparent strength distributions.

The simulation with the apparent strengths in Figure 5.14 was conducted only with the following input sources: the recorded sound, the history of loads, and single fibre properties previously measured. Therefore, another important finding is that the complete strain-load curve can be accurately reconstructed without any information about the history of displacements.

A limitation of this technique is that it was not able to provide the exact amount of fibres in the bundle. Despite a calibration was performed to estimate the sound level produced by the rupture of a single fibre, fibres surrounding a breaking fibre

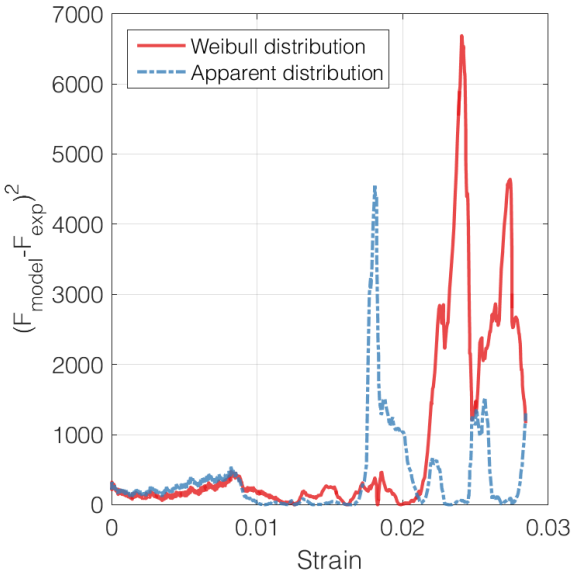

Figure 5.19: Residuals from the two simulation study cases with respect to the experimental results.

within a bundle will cause acoustic absorption; consequently reducing the levels of the sound acquired by the microphone. Further experiments with bundles containing fewer fibres should be conducted, to minimise acoustic absorption.

5.5.5 Frequency domain analysis

No SM events were registered in the first 10 seconds, therefore those frequencies below 3 kHz that appear during that time period in the time-frequency plot (Figure 5.15) must be the contribution of ambient noise only. This means that, when analysing the signals obtained during the breaking events, those frequencies will not be considered to be necessarily related to the breaking phenomenon.

From the main frequencies of all SM events, displayed in Figure 5.18, two main regions can be identified: a low frequency region below 2.5 kHz, that can be due to ambient noise as explained lines above, and a higher frequency region starting from approximately 12 kHz. Within this second area, frequencies of 12.5 kHz and 15 kHz seem to be common to most SM events. These are the frequencies that could

be related to the fracture of the glass fibres of the specific length of the specimens (10 mm).

5.6 Conclusions

In this Chapter the strength of single fibres and fibre bundles after exposure to water, salt water and post re-drying has been studied. Experimentally, tests on single fibres, and fibre bundles were conducted. In addition, a novel SM experimental method based on sound measurements was introduced to obtain a distribution of representative strengths of the fibres within a bundle. Numerically, the Weibull distribution of strengths and the set of strengths obtained by the SM technique were used to model the mechanical response of the bundles. The main concluding remarks of this chapter are:

- From the experiments on single fibres, it was observed that E-glass material itself is indifferent to 24-hour immersion in pure and salt water at 50°C.
- Bundle specimens immersed in pure water have shown a reduction in their strength, likely coming from the damage of the sizing.
- Rate sensitivity of the fibre bundles was observed in specimens exposed to all preconditioning environments.
- E-glass fibre bundles show strain rate sensitivity. The ratio W-Wet to Dry bundle strength is constant at different strain rates.
- SM allows a set of values to be reconstructed for "apparent strengths" that can be used as input for numerical experiments. The method provides results closer to the experiments and with more realistic features, in contrast to what is obtained with the Weibull set of strengths.

- This low cost and easy-to-implement method showed that, within the audible range, there are some main frequencies (12-15 kHz) that seem to be associated intrinsically with the breaking of E-glass fibres specimens of 10 mm.

Chapter 6

Effects of water absorption and strain rate on fibre reinforced polymers

This chapter investigates some effects of water immersion upon composite laminates experimentally and numerically. Specimens were immersed in a pure water bath at 50°C, and later re-dried to study the recoverability of properties. Tensile tests at strain rates from $0.001 - 700$ s^{-1}, and quasi-static short three-point bending experiments showed a drop in strength and modulus after water saturation. Experiments on re-dried specimens showed little or no recoverability of properties. The Hill-Mandel homogenisation on a unit cell, with wet and re-dry properties of the constituents, showed some limitations on conditioned composites due to the insensibility of the chosen homogenisation approach to damage of the fibre-matrix interface. Finally, a procedure to evaluate the stresses arising from water immersion is presented. It considers the simultaneous competition of matrix swelling and viscoelastic relaxation.

6.1 Introduction

For marine composites, water exposure remains to be one of the leading challenges since it can cause adverse long-term effects. Previous research has found that water

absorption can affect the mechanical performance of composites. It can decrease the strength [152], the interlaminar shear strength [7, 6], the flexural strength [153] and the modulus [82], or affect the impact behaviour [85]. Because of practical reasons in the laboratory, realistic immersion times cannot be replicated; therefore, acceleration of water absorption must be forced by immersing composites in a water bath at elevated temperature [51].

Experimental data in literature is very diverse, and the water absorption effects in composites seems to be dependent on the material, it configuration, and water immersion methodology. Water diffusion in composites can be Fickian [6, 154, 152] or non Fickian [54]. Moreover, while some studies found saturation after certain immersion time [6], others showed continuous weight increase or even weight loss due to leaching of low weight molecules [154, 80]. Water molecules within the composite can occupy free volumes in the matrix [55], bond to resin matrix [2], or even occupy matrix-fibre interface [6].

Polymer-based composites are rate dependent, mainly due to rate-dependent nature of the polymeric matrix. However, to the best of our knowledge, research into the influence of the water absorption upon the strain rate sensitivity of composites has been limited to compression and with no recoverability of properties study [85].

Finally, it is also known that water absorption induces swelling of the polymer [82, 51, 53, 80, 155], creating hydrostatic stresses within the composite matrix [156]. Derrien and Gilormini [156] developed analytical solutions for stresses induced by matrix swelling in the long term, neglecting viscous flow. During water absorption, swelling and viscous relaxation occur simultaneously. Therefore in this Chapter, we present a method to evaluate the water-induced stresses that involve the competition between swelling and viscous relaxation of the matrix until complete relaxation occurs.

6.2 Experimental methods

6.2.1 Material description and samples

Specimens were machined from $600 \times 600 \times 2.6\,\text{mm}^3$ composites panels prepared by the industrial partner BAE Systems. The resin matrix in the composite was the Prime 20 ULV system from Gurit. The reinforcement was the E-glass FGE238 non-woven unidirectional fabric from Formax (owned by Hexcel from 2016). This fabric contains 95% of its areal weight of untwisted *tex* 1200 fibre bundles oriented in the 0° direction, and 5% of its aerial weight consists of untwisted *tex* 300 bundles on the 90° orientation. Texturized polyester yarns keep all bundles stitched together as a fabric. Panels were prepared by resin transfer moulding (RTM) and cured for 16 hours at 50°C. Two stacking sequences were available: $[0]_8$ and $[90, 0]_{2s}$.

The volume fractions v_f of the unidirectional and bidirectional composites were calculated from their weight according to Equation 6.1.

$$v_f = \frac{\rho_c - \rho_r}{\rho_g - \rho_r}, \tag{6.1}$$

where ρ_c, ρ_r, ρ_g, are the densities of the composite, resin, and E-glass fibre respectively. The densities of the resin and composite were obtained from the measurements of weight (with 0.001 g precision) and volume (with 0.05 mm precision) of tensile and three point bending specimens. The density of E-glass fibre $\rho_g = 2.62\,\text{g/cm}^3$ was taken from literature [157].

The resulting values of v_f obtained by this method varied between 0.53 and 0.6 for both unidirectional and bidirectional specimens. This oscillation is due to the uneven microscopic distribution of fibres with resin rich areas, especially in between the fibre fabrics and in between the bundles of the same fabric (Figure 6.1). In the rest of the document, an average volume fraction of 0.56 will be assumed.

For quasi-static (QS) characterisation, the following types of coupons were fabric-

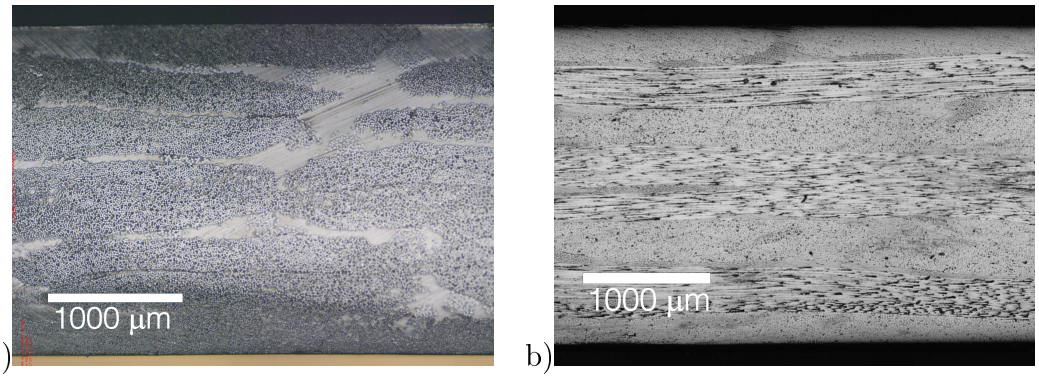

Figure 6.1: Microscopy of the composite material: a) Unidirectional laminate, b) Bi-directional laminate.

ated: $[90°]_8$ tensile specimens (QS90), $[45°]_8$ tensile specimens (QS45), and $[90°, 0°]_{2s}$ short three point bending specimens (sTPB). The QS90, QS45 and sTPB specimens were manufactured by diamond saw cutting, with dimensions as per recommendations of the standard ASTM D3039 [158], and standard ASTM D2344 [159] (Figure 6.2).

For high strain-rate experiments, $[45°]_8$ grinded dogbone tensile specimens were manufactured. No grinded was practiced in the thickness direction as it would make it difficult to ensure the integrity of all the fibres near the ground faces. The design of the specimens considered two steel M12 threaded shoulders glued to their ends with the epoxy based structural adhesive 3M DP 490. Threads allowed fastening to the split Hopkinson bar system. Details of the specimen can be seen in Figure 6.3. The dimmensions chosen were optimised by trial and error in order to reach equilibrium during the test as well as to consistently obtain failure within the cross section.

6.2.2 Water absorption

Marine composite structures can be in wet working conditions for up to several years. To accelerate water absorption, specimens were immersed in distilled water at 50°C. The sides of the coupons were protected with aluminium tape to prevent water from entering the composite through the sides [154], ensuring unidirectional through-

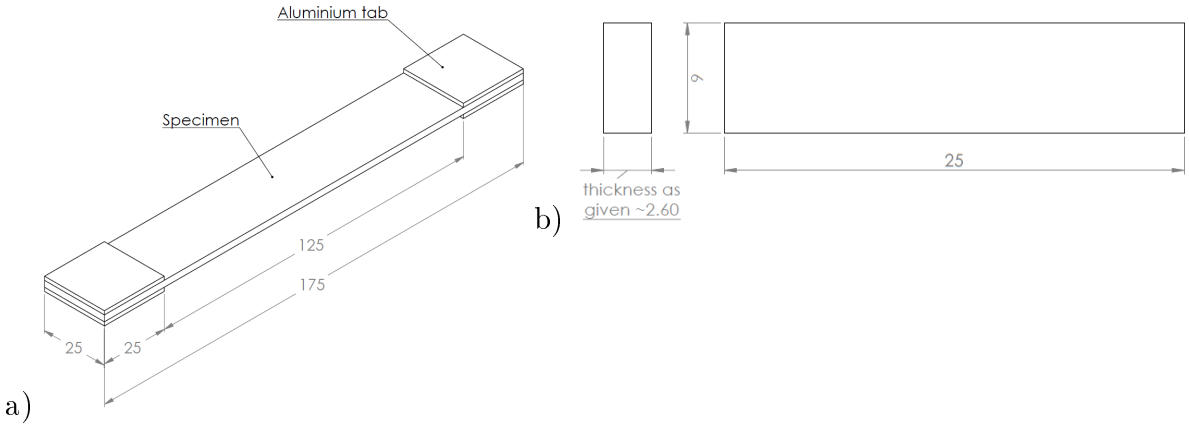

Figure 6.2: Schematic of specimens for QS experiments: a) QS90 and QS45, b) sTPB

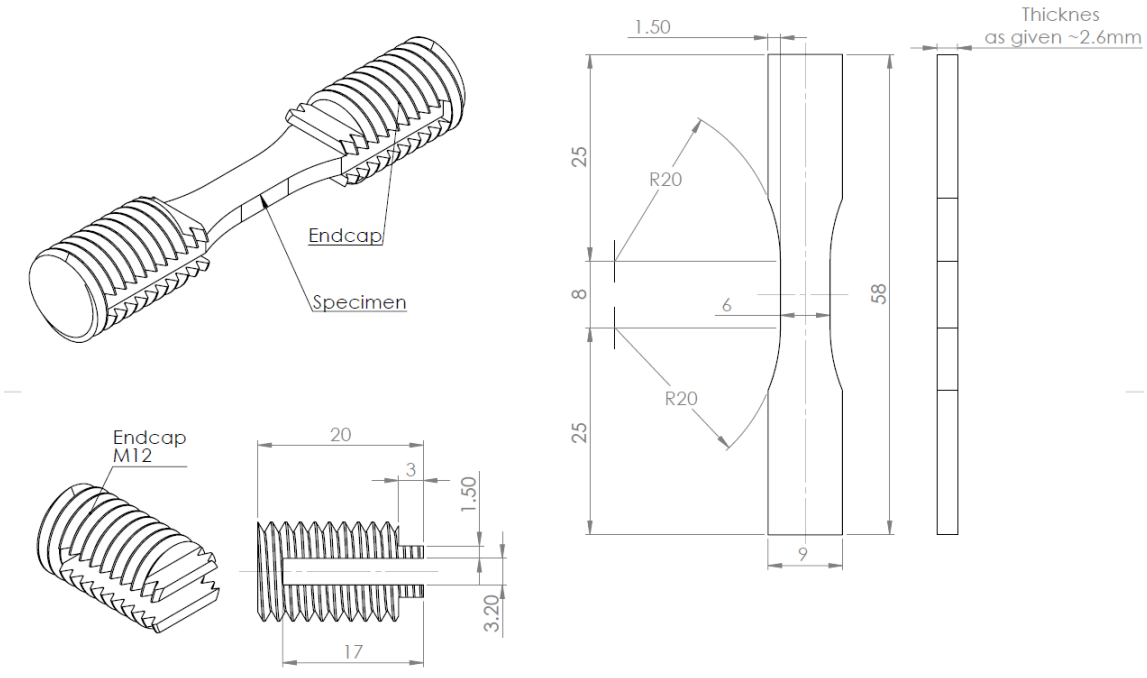

Figure 6.3: Geometry of tensile specimens for high strain rate experiments.

thickness diffusion only. Diffusion in directions different from the through thickness, like fibres direction, may lead to capillarity effects [51]. However, the gravimetric analysis was done with the weight measurements on a non-taped sTPB specimen because measurements on taped specimens suggested unrealistic excessive weight gains, possibly coming from the formation of aluminium oxide or the water intake of the adhesive.

Samples were dried in a Binder FED series oven at 50°C prior to immersion in the water bath. The weight was periodically monitored with the OHAUS DV215 balance (with 0.01 mg precision), to determine when the specimens reached equilibrium.

The measured weight was used to determine the percent water content $\%\Delta w_t$:

$$\%\Delta w_t = \frac{(w_t - w_{dry})}{w_{dry}} \times 100\%, \tag{6.2}$$

where w_t is the weight at the monitoring time t, and w_{dry} is the weight of the fully dry specimen ($\%\Delta w_t = 0$). Complete drying was identified by the stabilisation of percent water content, achieved after approximately 500 hours. Dry specimens (Dry) were tested to have a baseline value of the composites properties.

The dry specimens were later immersed in the water bath. Water absorption was again measured by Equation 6.2, reaching saturation after 1200 hours with a maximum percent water content of $\%\Delta w_s^{comp} = 0.71\%$. Saturated specimens (W-Sat) were tested after a total of approximately 2500 hours of immersion, to observe the effects of water saturation.

To verify if the effects caused by water absorption were recoverable, fully saturated specimens were re-dried in the oven at 50°C until no significant change in weight was measured. Specimens reached this condition in approximately 300 hours, and are identified with the label W-RD.

The time histories of the percent water content during drying, immersion, and re-drying processes are presented in Figure 6.4.

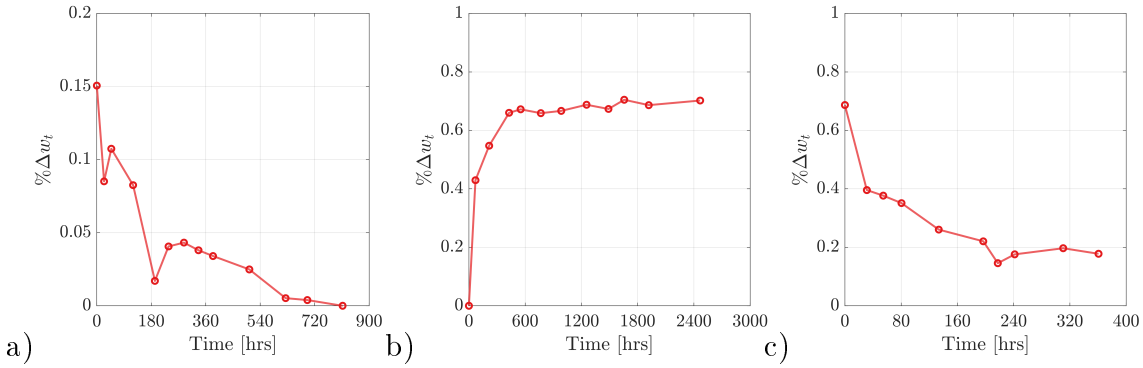

Figure 6.4: Time histories of water content of composites: a) Drying, b) Water immersion and c) Re-drying.

It is possible to analytically calculate a priori an estimation of $\%\Delta w_s^{comp}$ if we considered the existence of water only in the fully saturated resin matrix. The expected percent water content in the saturated composite should be:

$$\%\Delta w_{sat-comp}^{exp} = \frac{w_w}{w_c} \cdot 100\%, \tag{6.3}$$

where $w_c = V_r \cdot \rho_r + V_f \cdot \rho_f$ is the total weight of the composite, and w_w is the weight of the water contained within the fully saturated resin matrix of weight w_r, hence:

$$w_w = \frac{w_r \cdot \%\Delta w_s}{100}, \tag{6.4}$$

where $\%\Delta w_s^r$ is the resin maximum percent water content measured in Chapter 3. Replacing w_c and w_w in Equation 6.3:

$$\%\Delta w_{sat-comp}^{exp} = \frac{V_r \cdot \rho_r \cdot \%\Delta w_s}{V_r \cdot \rho_r + V_f \cdot \rho_f} \tag{6.5}$$

From the definition of volume fraction: $V_f/V_r = v_f/(1-v_f)$. Therefore, Equation 6.5 can be simplified to:

$$\%\Delta w_{sat-comp}^{exp} = \frac{\%\Delta w_s}{1 + \frac{v_f \cdot \rho_g}{(1-v_f)\cdot \rho_r}} \tag{6.6}$$

This expression depends only on the volume fraction, the densities of the con-

stituents and the maximum water percent weight gain of the resin. Upon replacing $\%\Delta w_s^r = 2.81$, $v_f = [\![0.53; 0.60]\!]$, $\rho_g = 2.62\,\mathrm{g/cm^3}$, $\rho_r = 1.14\,\mathrm{g/cm^3}$ in Equation 6.6, we obtain the interval $\%\Delta w_{sat-comp}^{exp} = [\![0.63; 0.78]\!]\,\%$.

6.2.3 Mechanical characterisation

All tests were performed in the lab conditions with 40±8% relative humidity and at 20±3°C. The time for extracting the specimen from its conditioning environment, including its handling and testing, was always under 25 minutes to prevent significant moisture loss or gain due to interaction with the air in the room. This time was also long enough to reach thermal equilibrium.

In quasi-static regime, all tests were performed in the Zwick Z250 screw-driven universal testing machine. QS90 and QS45 specimens were tested following the recommendations of the standard ASTM D3039 [158]. The specimens were clamped from their aluminium end tabs with wedge grips moving at a prescribed displacement rate of 0.0125 mm/s. The force was measured with a load cell of 250 kN, while the strains were obtained from the DIC analysis of photos taken with a JAI camera obtained at 1 fps (frames per second).

For the sTPB tests, recommendations of the standard ASTM D2344 [159] were followed. The specimens were symmetrically placed on top of two side supports of 1.5 mm radius, with a span length of 12.5 mm. The load was applied on the top midpoint of the coupons with a 3mm radius loading nose moving at a prescribed speed of 0.0166 mm/s. The applied force was measured with a load cell of 20 kN mounted on the crosshead. The displacements of the midpoint were computed from the DIC analysis of the pictures obtained from the JAI camera at a rate of 1 fps. The short beam strength F^{sbs} in sTPB tests is obtained from the maximum force during the test:

$$F^{sbs} = 0.75 \cdot \frac{P_m}{b \cdot q}, \tag{6.7}$$

Table 6.1: Label convention for all tested composite specimens.

Specimen\Conditioning	Dry	W-Sat	W-RD
QS - Tension 45°	QS45-Dry	QS45-W-Sat	QS45-W-RD
QS - Tension 90°	QS90-Dry	QS90-W-Sat	QS90-W-RD
HR - Tension 45°	HR45-Dry	HR45-W-Sat	HR45-RD
QS - short three point bending	sTBP-Dry	sTPB-W-Sat	sTPB-RD

where b and q are the width and thickness of the specimen.

At high strain rates, dogbone specimens were tested in the split Hopkinson pressure bar, with a configuration similar to the one described in Section 3.5. The stress versus time history was calculated with one-dimensional wave theory, using the measurements from the three sets of strain gauges. The history of strains were measured via DIC analysis of the high-speed pictures taken at a framerate of 200000 fps with the Kirana camera from Specialised Imaging. Validation of these tests was performed by measuring the force equilibrium at the ends of the specimen, which was obtained after approximately 700 μs, followed by an approximately constant strain rate.

At least three of the tests described above were conducted for each conditioning state described in the previous section. Table 6.1 summarises the types of tests, conditioning environments, and the labels that will be used to identify every case.

Direct measurements of matrix swelling in the composite are experimentally challenging to obtain. Therefore a neat resin specimen $30 \times 50 \times 2.4\,\text{mm}^3$ was immersed in the bath for the same time as the composites were exposed to water (2500 hours). Measurements with a micrometre (0.01 mm resolution) prior and after immersion showed an average linear expansion of 0.0066.

Finally, the viscoelastic properties of the composite matrix were characterised by DMA on a $35 \times 10 \times 2.65\,\text{mm}^3$ neat resin specimen in tension. The coupon was subjected to a frequency and temperature sweep from 0.001 to 30 Hz, and from 10-110°C in steps of 5°C.

6.3 Modelling framework

6.3.1 Homogenisation

The effective modulus or Hill-Mandel homogenisation method was used to obtain the homogenised properties of the composites at three different states: Dry, Saturated (W-Sat), and Re-dry (RD). It is based on the microstructural analysis of a unitary cell. The method relies on the Hill-Mandel condition, *i.e.* the consistency between the strain energy at micro and macro-scale. To solve the problem by the kinematic approach of this method, a uniform strain field $\underline{\underline{\epsilon}}$ is prescribed in the periodic boundary of the unit cell. The resulting stresses are then averaged over the domain, obtaining the elements of the stiffness matrix from constitutive relationships.

In this case, the problem was implemented in COMSOL Multiphysics v4.4 [99]. A hexagonal unit cell Ω of volume fraction $v_f = 0.56$ and fibres oriented in the 3-direction were modelled (Figure 6.5). The properties of resin and E-glass fibres, measured in Chapters 3 and 5, were used to compute the homogenised properties of the composite. For the resin, the elastic modulus $E_r^{Dry} = 2.6$ GPa, $E_r^{Sat} = 2.0$ GPa, $E_r^{RD} = 2.4$ GPa; and the Poisson's ratio $\nu_r^{Dry} = \nu_r^{Sat} = \nu_r^{RD} = 0.4$. The properties of the E-glass fibres are indifferent to water exposure: $E_g = 60$ GPa (experimentally measured); and Poisson's ratio $\nu_g = 0.18$ taken from literature [160].

For nodes P and M in opposite sides of the unit cell, and displacements vectors $\underline{u}_P$ and $\underline{u}_M$ respectively, the following boundary condition was prescribed:

$$\underline{u}_P = \underline{u}_M + \underline{\underline{\epsilon}} \cdot \underline{PM} \tag{6.8}$$

The constitutive relationship in Voigt notation for the homogenised material is shown in Equation 6.9.

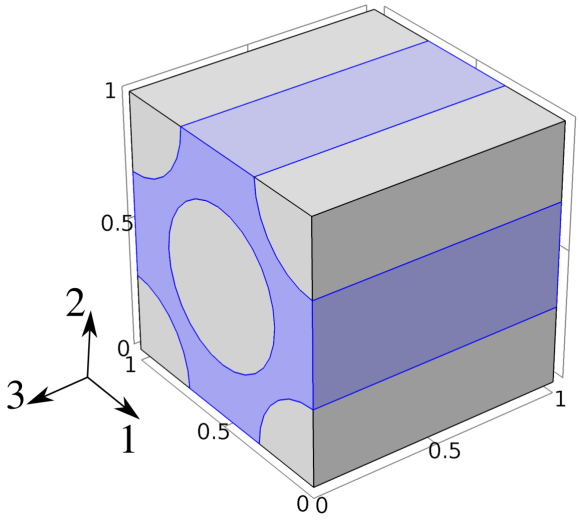

Figure 6.5: Hexagonal unit cell used for the Hill-Mandel homogenisation.

$$\begin{bmatrix} \bar{\sigma}_{11} \\ \bar{\sigma}_{22} \\ \bar{\sigma}_{33} \\ \bar{\sigma}_{12} \\ \bar{\sigma}_{13} \\ \bar{\sigma}_{23} \end{bmatrix} = \begin{bmatrix} C_{11} & C_{12} & C_{13} & 0 & 0 & 0 \\ C_{12} & C_{22} & C_{23} & 0 & 0 & 0 \\ C_{13} & C_{23} & C_{33} & 0 & 0 & 0 \\ 0 & 0 & 0 & C_{44} & 0 & 0 \\ 0 & 0 & 0 & 0 & C_{55} & 0 \\ 0 & 0 & 0 & 0 & 0 & C_{66} \end{bmatrix} \begin{bmatrix} \epsilon_{11} \\ \epsilon_{22} \\ \epsilon_{33} \\ \epsilon_{12} \\ \epsilon_{13} \\ \epsilon_{23} \end{bmatrix}, \tag{6.9}$$

where ϵ_{ij} are the components of the Voigt representation $\underline{\epsilon}$ of the strain field $\underline{\underline{\epsilon}}$, C_{ij} are the components of the homogenised stiffness tensor of the composite, and $\bar{\sigma}_{ij}$ are the average σ_{ij} stress over the volume V of the unit cell calculated as:

$$\bar{\sigma_{ij}} = \frac{1}{V} \int_{\Omega} \sigma_{ij} \partial\Omega \tag{6.10}$$

The prescribed field of strains $\underline{\epsilon}$ is conveniently chosen to allow for easy characterisation of the C_{ij} components:

$$\underline{\epsilon}^1 = \begin{bmatrix} 1 \\ 0 \\ 0 \\ 0 \\ 0 \\ 0 \end{bmatrix}; \underline{\epsilon}^2 = \begin{bmatrix} 0 \\ 1 \\ 0 \\ 0 \\ 0 \\ 0 \end{bmatrix}; \underline{\epsilon}^3 = \begin{bmatrix} 0 \\ 0 \\ 1 \\ 0 \\ 0 \\ 0 \end{bmatrix}; \underline{\epsilon}^4 = \begin{bmatrix} 0 \\ 0 \\ 0 \\ 1 \\ 0 \\ 0 \end{bmatrix}; \underline{\epsilon}^5 = \begin{bmatrix} 0 \\ 0 \\ 0 \\ 0 \\ 1 \\ 0 \end{bmatrix}; \underline{\epsilon}^6 = \begin{bmatrix} 0 \\ 0 \\ 0 \\ 0 \\ 0 \\ 1 \end{bmatrix} \quad (6.11)$$

The first simulation with prescribed strain $\underline{\epsilon}^1$, allows to solve for the components $C_{11} = \bar{\sigma}_{11}$; $C_{22} = \bar{\sigma}_{22}$; $C_{13} = \bar{\sigma}_{33}$. Note that the unit cell is transversely isotropic, hence only five simulations with five values of $\underline{\epsilon}$ are required.

Once the components of the stiffness tensor $\underline{\underline{C}}$ are found, the five homogenised independent elastic properties can be identified: E_3, E_2, G_{12}, v_{12}, v_{23}. E_2 should be similar to the value measured in the QS90 experiment. $\underline{\underline{C}}$ can then be rotated 45° to obtain the expected homogenised value of the elastic modulus on QS45 specimens.

6.3.2 Matrix swelling

As water diffuses into the composite, it induces swelling of the matrix. Glass, on the other hand, does not expand. This mismatch in water-induced expansion leads to stresses in the matrix that can be evaluated in a unit cell analysis. Water-induced expansion contributes to the stresses in a similar way thermal stresses ($\xi\delta_{ij}\Delta\theta$) do. Their contribution in the constitutive relationship can be expressed by the term $\eta\delta_{ij}\Delta\psi$ as:

$$\sigma_{ij} = 2G\varepsilon_{ij} + \lambda\varepsilon_{kk}\delta_{ij} + \xi\delta_{ij}\Delta\theta + \eta\delta_{ij}\Delta\psi, \quad (6.12)$$

where G and λ are the Lame's parameters, ξ is the linear thermal expansion coefficient, $\Delta\theta$ is the variation temperature, η the water-induced linear expansion coefficient,

$\Delta\psi$ is the variation of water weight gain, and δ_{ij} is the Kronecker delta function. This means that without implementing any additional subroutine, the water-induced stresses can be modelled as a thermal expansion.

The simulation was set up in Abaqus [115] with symmetric boundary conditions to calculate the stresses that arise from this matrix swelling. The model of a centered hexagonal unit cell of $v_f = 0.56$ was setup with fully elastic materials and dry properties of the constituents: $E_r^{Dry} = 2.6$ GPa, $\nu_r^{Dry} = 0.4$, $E_g = 60$ GPa, and $\nu_g = 0.18$. Matrix expansion was emulated with $\xi = 0.0066$ and a fictitious increment of temperature of $\Delta T = 1°$ C, which would provide the experimentally measured linear expansion in the neat resin.

6.3.3 Matrix viscoelasticity

The raw data of storage and loss Young's moduli (E' and E'' respectively) was post-processed using the time-temperature equivalence and superposition method described in [161]. This meant that a much broader frequency domain of the viscoelastic properties could be utilised.

Assuming Poisson's ratio real and constant over the frequency range, the following relationships for the complex shear modulus G^* and bulk modulus K^* should hold:

$$G^* = \frac{E^*}{2(1+\nu)}, \tag{6.13}$$

$$K^* = \frac{E^*}{3(1-2\nu)}. \tag{6.14}$$

E^*, G^* and K^* can be decomposed in their imaginary and real parts. Therefore the real component of $G^*$and K^* would be:

$$G' = \frac{E'}{2(1+\nu)}, \tag{6.15}$$

$$K' = \frac{E'}{3(1-2\nu)}, \tag{6.16}$$

which are known as storage shear modulus G' and storage bulk modulus K' respectively. Similarly, their complex component, named loss shear modulus and loss bulk modulus respectively:

$$G'' = \frac{E''}{2(1+\nu)}, \tag{6.17}$$

$$K'' = \frac{E''}{3(1-2\nu)}. \tag{6.18}$$

Viscoelastic materials can be modelled by a Prony series. Abaqus can handle the input of tabular experimental data in frequency domain to fit a Prony series of up to 13 elements to its built-in viscoelastic material. The tabular data requires the real $\Re$ and imaginary part $\Im$ of ωg^* an ωk^*; where g^* and k^* are the non-dimensional shear and bulk modulus respectively. They can be calculated from the experimentally obtained values of the loss and storage bulk and shear moduli [115]:

$$\omega\Re(g^*) = \frac{G''}{G_\infty},\ \omega\Im(g^*) = 1 - \frac{G'}{G_\infty},\ \omega\Re(k^*) = \frac{K''}{K_\infty},\ \omega\Im(k^*) = \frac{K'}{K_\infty}, \tag{6.19}$$

where K_∞ and G_∞ are the long-term bulk and shear moduli.

The model of the centered hexagonal unit cell used for the matrix swelling analysis was modified by adding the viscoelastic properties to the matrix, using the tabular data obtained from Equation 6.19. Four simulation cases were run to explore the effects of the viscoelastic relaxation and water-induced expansion:

a) 2-step simulation with relaxation starting after full matrix expansion;

b) 1-step relaxation and expansion taking place simultaneously during a period of 2800 hours;

c) 1-step 2800 hours of simultaneous relaxation and swelling, with maximum swelling being reached in 500 hours; and

d) 1-step 2800 hours of simultaneous relaxation and swelling, with complete swelling in 1000 hours.

6.4 Results

6.4.1 Mechanical characterisation

Results are displayed according the label scheme introduced in Table 6.1. In some cases, the number at the end of the label indicates the strain rate of the test in s^{-1}.

Figure 6.6 shows typical strain versus stress curves observed in QS90 tests, for all conditioning cases. Figure 6.7 displays representative strain versus stress curves of experiments on QS45 and HR45 specimens at all conditioning environments.

The strength of the specimens is the maximum stress σ_u measured in the experiment. In both QS45 and QS90 tests, there is a linear region at the beginning of the loading curve, where the Young's modulus E is measured. At high strain rate, the initial part of the strain-stress curve cannot be used to obtain E because the specimen is not in equilibrium; however there is equilibrium by the time it reaches its maximum stress.

Figure 6.8 displays the typical displacement versus force curves in short three point bending tests. After an initial elastic response, a maximum load P_m is attained, followed by damage and inelastic deformation of the matrix.

Figures 6.9a and 6.10a show the effects of the conditioning procedures upon the Young's modulus E of QS90 and QS45 specimens. The homogenised elastic modulus obtained by the periodic homogenisation (described in Section 6.3.1), are included in both plots for comparison with the experimental measurements.

Figure 6.9b displays the strengths σ_u of QS90 specimens. For reference, the strengths of the neat resin are also plotted. Figure 6.10b portraits the effects of

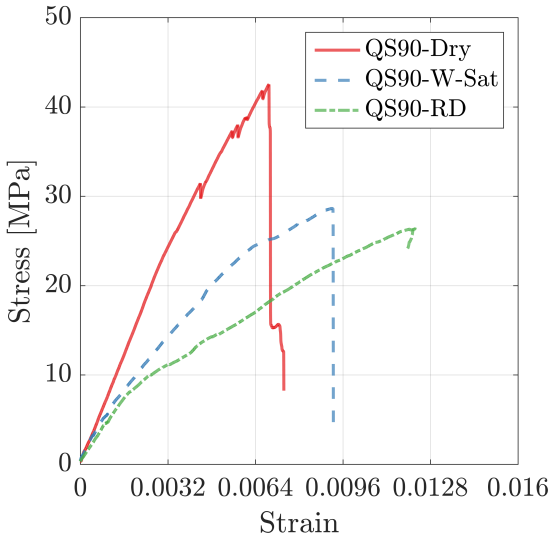

Figure 6.6: Typical Strain Stress Curves for QS90 tests.

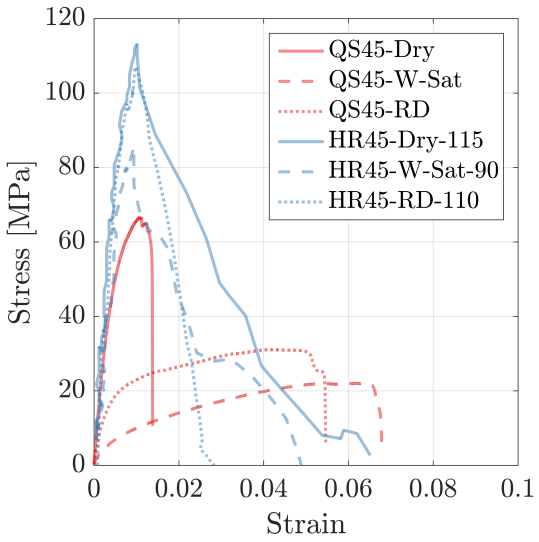

Figure 6.7: Typical Strain stress curves for 45° oriented coupons (quasi-static and high rate).

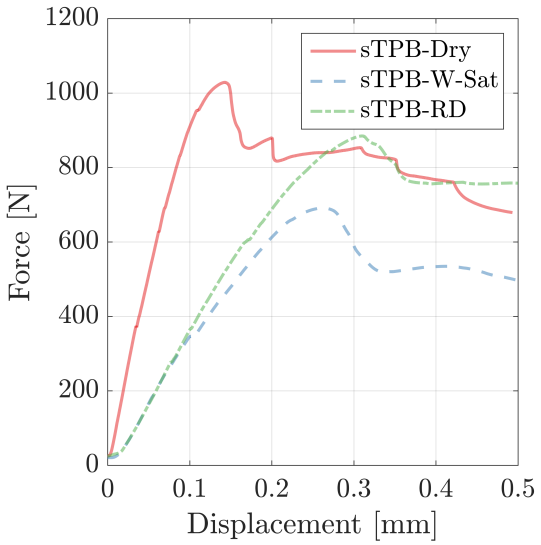

Figure 6.8: Typical loading curves in composite short 3PB tests.

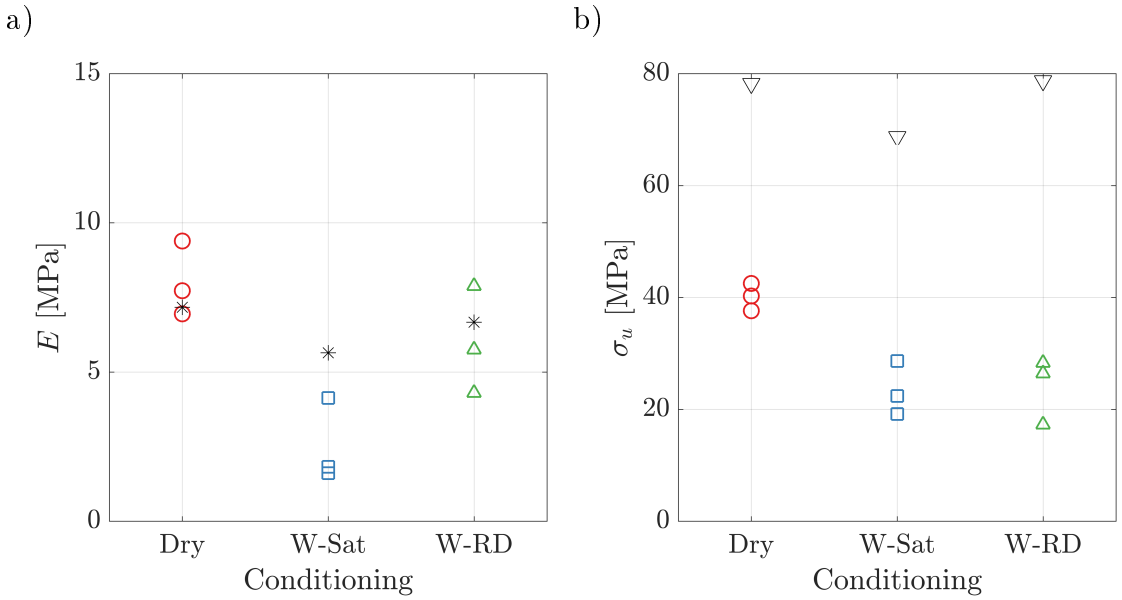

Figure 6.9: Mechanical properties of Dry ($\circ$), W-Sat ($\square$), W-RD ($\triangle$) QS90 specimens: a) Experimental and homogenised modulus ($*$), b) Strengths of the composite and the neat resin (∇).

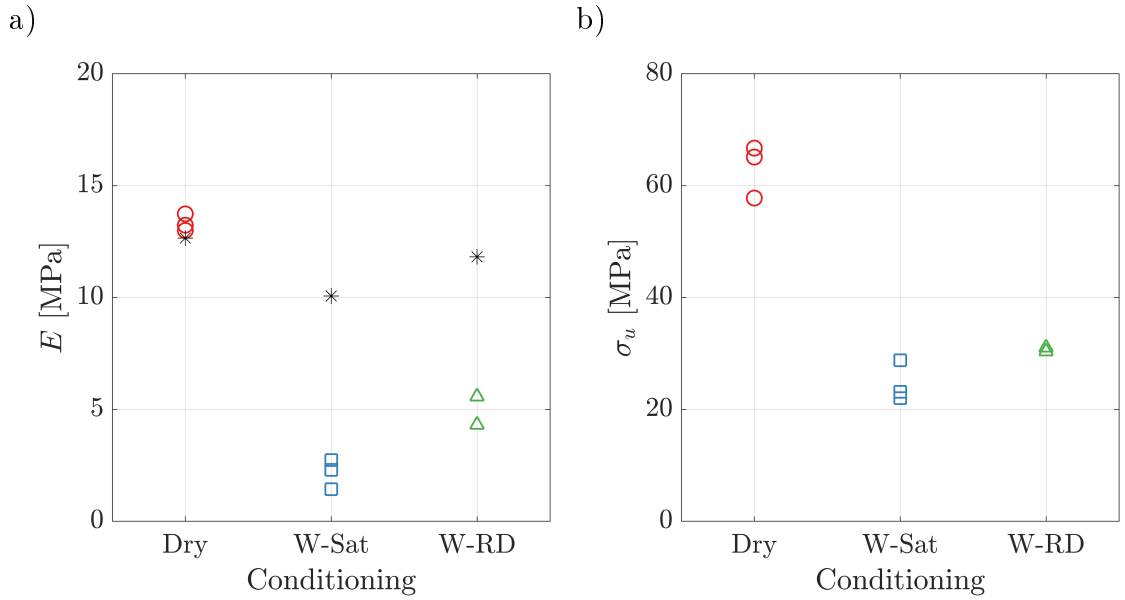

Figure 6.10: Mechanical properties of Dry (○), W-Sat (□), and W-RD (△) QS45 coupons: a) Young's modulus and expected values by homogenisation (∗), b) Strengths.

the conditioning environments upon strength σ_u obtained in QS45 tests.

Figure 6.11 summarises the effects of water saturation and post re-dry upon the short beam strength obtained in the sTPB tests.

To highlight the influence of strain rate and the conditioning procedures, tensile strengths of QS45 and HR45 coupons are shown in Figure 6.12.

The raw storage and loss Young's moduli obtained in DMA tests are shown in Figures 6.13 and 6.14 respectively. Figure 6.15 displays the shifted storage and loss Young's moduli after applying the principle of time-temperature equivalence and superposition, with a reference temperature of 50°C.

The loss and storage shear and bulk moduli, shown in Figures 6.16-6.17, were calculated with Equations 6.15-6.18 using the values of E' and E'' from Figure 6.15. The tabular data described in 6.19 required for setting up the viscoelastic material in Abaqus was calculated with Equation 6.19 and $G_\infty = 1.75 \times 10^5$ Pa, $K_\infty = 10^6$ Pa.

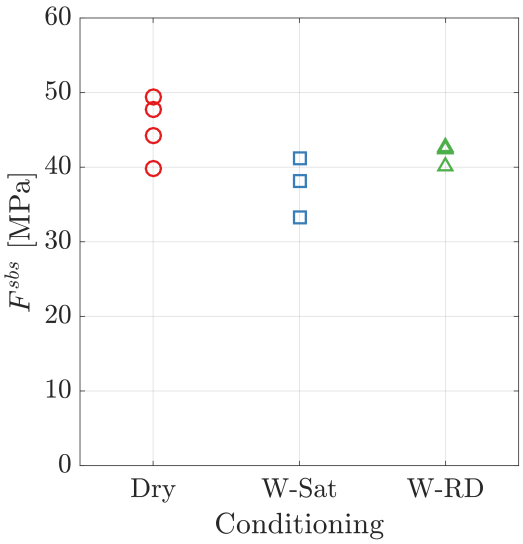

Figure 6.11: Effects of pre-conditioning on the short beam strength.

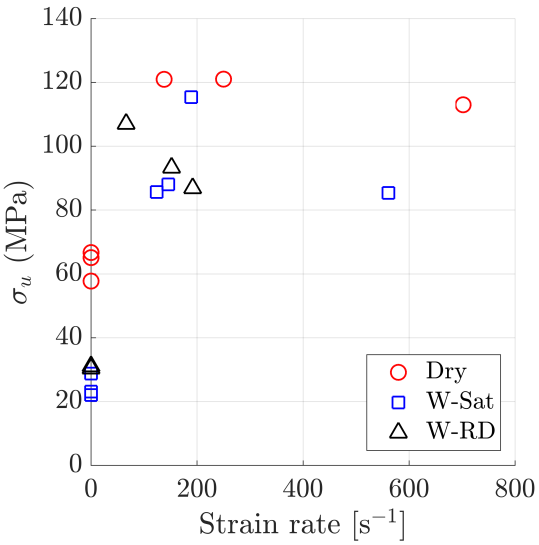

Figure 6.12: Tensile strength of QS45 and HR45.

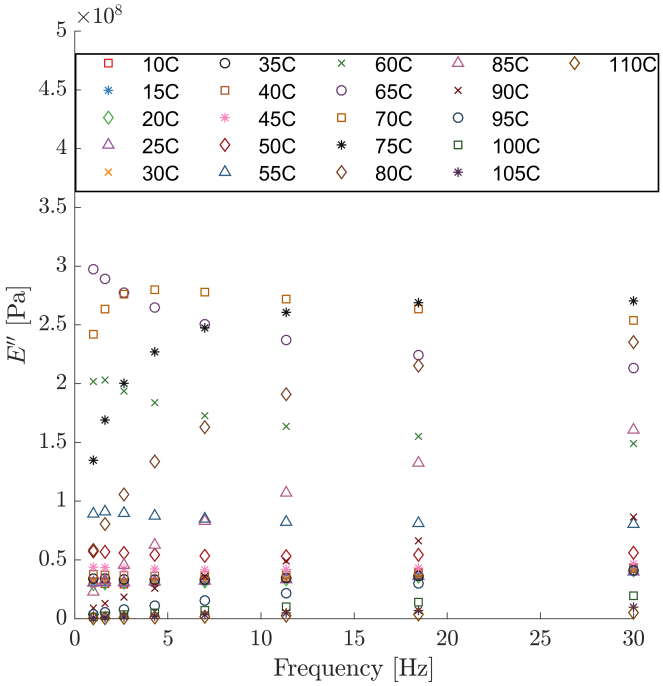

Figure 6.13: Storage elastic modulus E'.

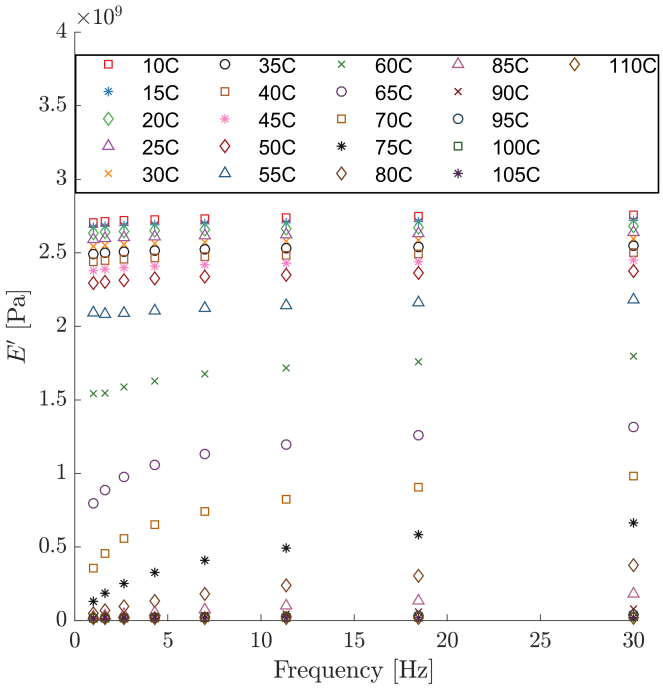

Figure 6.14: Loss elastic modulus E''.

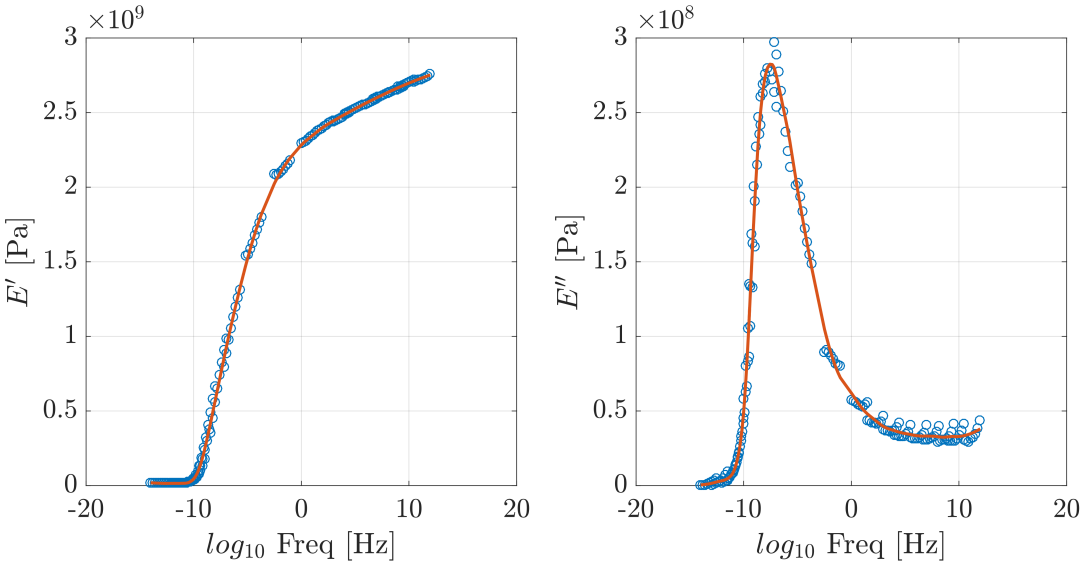

Figure 6.15: Storage and loss Young's moduli E' and E''.

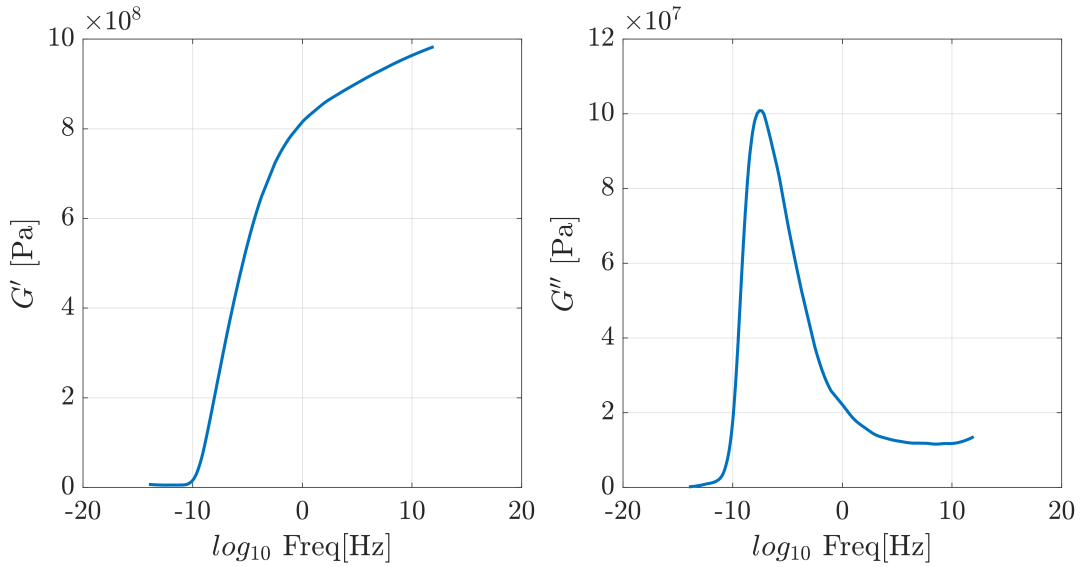

Figure 6.16: Storage and loss shear moduli G' and G''.

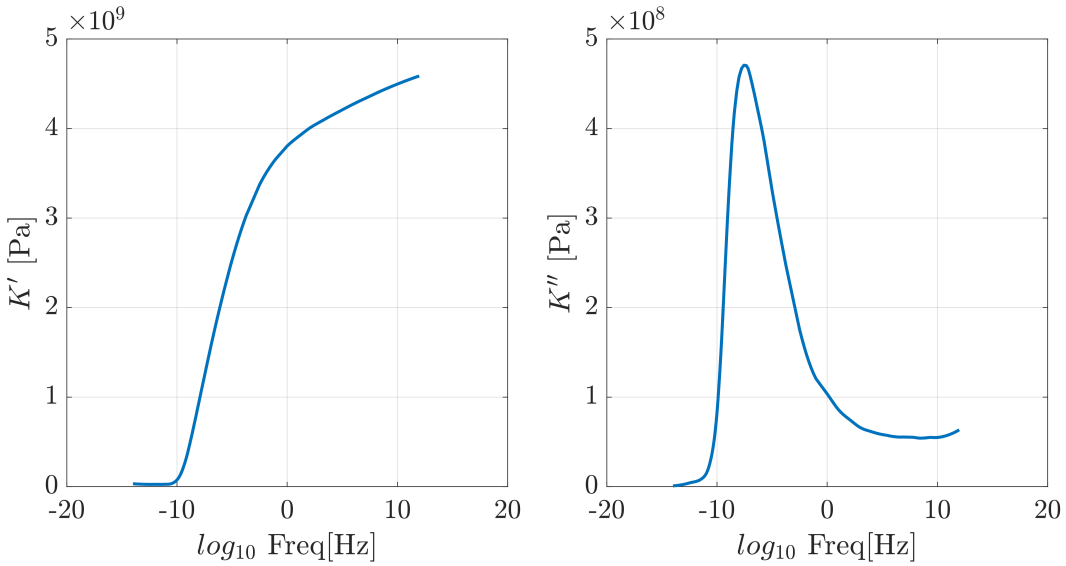

Figure 6.17: Storage and loss bulk moduli K' and K''.

6.4.2 Matrix swelling and relaxation

Figure 6.18 shows the resulting Von Misses stresses in the unit cell after matrix swelling. It shows that matrix reaches stresses of up to 52 MPa.

For the element with higher Von Misses stress σ_{vm}^{EH} (Figure 6.18), the resulting σ_{vm}^{EH} vs. time found in the simulations described in Section 6.3.3 are plotted in Figure 6.19.

6.5 Discussion

6.5.1 Water absorption in composites

The measured percent water content at saturation $\%\Delta w_s^{comp} = 0.71\%$ falls within the limits of the interval $\%\Delta w_{sat-comp}^{exp} = [\![0.63;\ 0.78]\!]\,\%$ that were analytically calculated with the assumption that water is only contained in the resin. This suggests that the major contribution of water uptake came from water absorbed by the resin matrix; furthermore, water occupying the fibre-matrix interface could not be measured or detected solely by gravimetric analysis. During immersion, no weight loss was observed,

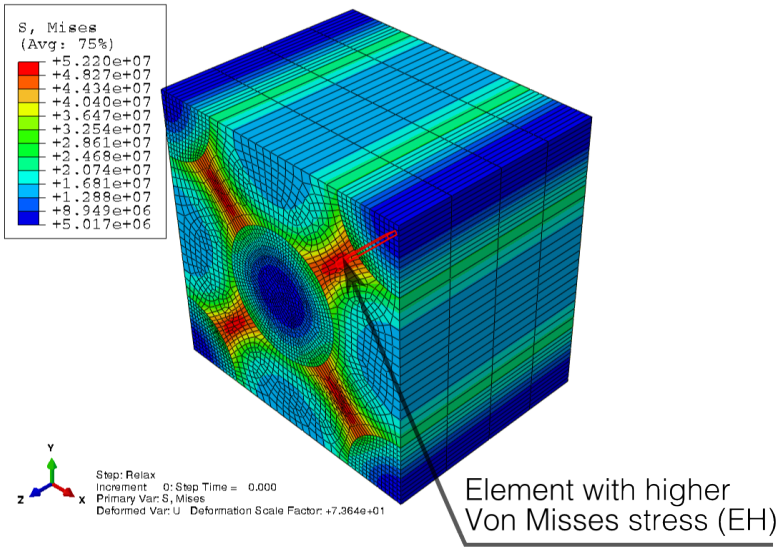

Figure 6.18: Von Misses stresses after matrix swelling.

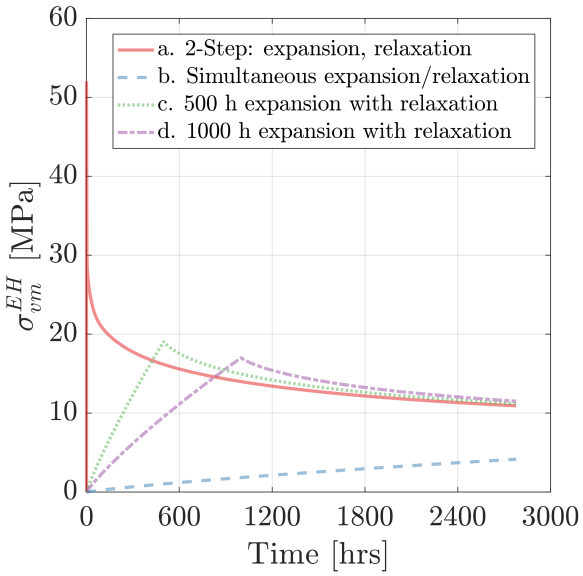

Figure 6.19: History of Von Misses stress in the element with higher stress.

indicating that leaching is not noticeable during the 2500 hours of immersion at 50°C.

6.5.2 Effects of water absorption

Water absorption caused negative effects on the mechanical properties of composites at all testing modes and strain rates (Figures 6.9-6.12). The tensile strength, elastic modulus, and short beam strength decreased with water saturation. These results are opposed to the findings of Woldesenbet *et al.* [85] in unidirectional compression specimens. They reported that at high strain rate, the strength of water saturated specimens was higher than the strength of dry specimens. They attributed such effect to the rate sensitivity of the matrix, disregarding the strain-rate sensitivity of fibres and the fact that in compression, fibre-matrix interface damage do not prevent the fibres from contributing to the strength.

Water exposure reduced the Young's modulus by 80%, and the strength by 50% on QS90 specimens. For QS45, reductions of 80% and 58% on E and σ_u were observed respectively.

The effects of water upon the strength of QS90 specimens would be expected to agree with the reduction in strength of the neat resin (12% drop, Figure 6.9b). However, there is a more pronounced drop in strength in the composite specimens, suggesting that the matrix-fibre interface must have also suffered damage from water interaction.

QS45-W-Sat and QS90-W-Sat specimens (Figures 6.7 and 6.6 respectively) show a higher strain to failure, indicating ductilisation of the matrix, as water allows for easier flow of the polymer chains.

6.5.3 Effects of strain rate

Figure 6.12 shows that the composite is clearly rate sensitive regardless of the conditioning the specimen has gone through. The ratio W-Sat to Dry strength is not the

same at different strain rates: for 58% for 0.001 s^{-1}, and 30% for 100 s^{-1}. The material seems to be less affected by water degradation at higher strain rates; this is the same trend that was observed in pure epoxy by Quino *et al.* [13]. This signifies the higher strain rate sensitivity on conditioned specimens with respect to dry specimens.

6.5.4 Effects of re-drying

During re-drying, it was not possible to eliminate all the water absorbed by composite, in line with observations in previous studies of neat resin [2]. In Figures 6.9 and 6.10 the re-drying process slightly recovers the Young's modulus up to 38% of the initial value. Despite the clearly high recoverability of the resin strength (Chapter 3), the strength of the composites, as seen in Figs 6.9-6.12, show little or no recovery. This gives further evidence for fibre-matrix interface damage or fibre debonding [162], as this type of effect cannot be reversed by the removal of water.

6.5.5 Homogenisation

The chosen homogenisation approach greatly simplified the microstructure of the composite, ignoring resin rich areas. However, it proved to accurately estimate the The Young's modulus in the QS90-Dry case (Figure 6.9a) and in the QS45-Dry (Figure 6.10a) cases. In Figure 6.10a, the overestimation of the homogenised Young's modulus of QS45-W-Sat, and QS45-W-RD show that apart from the changes in the bulk matrix, there must be other mechanisms of degradation such as fibre debonding.

6.5.6 Swelling and relaxation of the matrix

The simulations showed the importance of taking into account both expansion and relaxation, as simultaneous phenomena during water absorption. The maximum Von Misses stress in the unit cell after applying only matrix expansion is 52 MPa (Figure 6.18), which is 60% of the strength of the resin. After full relaxation, the stress

decreases up to only 12 MPa. Simulations also show that the smaller the time to reach saturation, hence full matrix expansion, the higher the stress in the matrix during the process. This gives evidence that there are risks to be considered when accelerating water absorption. A smaller time to reach water saturation or a highly accelerated water absorption will not allow enough time to relax, and high stresses may cause damage in the composite that would never occur in a real application.

6.6 Conclusions

The results of this extensive experimental campaign showed the detrimental effects of water upon the properties of marine laminate composites, over a range of strain rates, and configurations. Results of the mechanical characterisation were contrasted with the expected values by periodic homogenisation. Finally simulations of swelling and relaxation were presented. The main conclusions of this Chapter are the following:

- The composite mainly absorbs water within the matrix, which is not fully removable after re-drying.
- It was not possible to remove the water absorbed by the composite.
- Water reduces the stiffness, tensile strength, and the short beam strength, at all strain rates.
- Water absorption ductilises the composite.
- Re-drying partially recovers the Young's modulus of the composite, but the strength is little or non-recoverable.
- In order to calculate the stresses induced after water exposure, swelling and relaxation must be taken into account as simultaneous phenomena.

Chapter 7

Conclusions

In this investigation, the aim was to examine the effects of wet environments upon the strain rate dependent properties of composites and their constituents. Extensive experimental campaigns were conducted, and modelling strategies were developed. This work provided the first comprehensive study of the effects of water on the strain rate dependent behaviour of composites and each of their constituents. This thesis established a quantitative, qualitative, experimental, and modelling framework for capturing such effects. The main conclusions drawn from this investigation are discussed below.

7.1 Resin

Pure water and salt water transport within epoxy resin followed Fick's laws of diffusion, with higher diffusivity in the case of pure water. All the water absorbed by the polymer during immersion could not be extracted with re-drying at 50°C and explains the non-recoverable changes in the properties of the polymer.

It was shown that epoxy resin is strain rate dependent regardless the water treatment. Water saturation led to lower values of modulus and yield stress at all strain rates.

It was possible to tune and modify the Arruda-Boyce model to fit the experiments from $0.001-0.1\text{s}^{-1}$ for three different pre-conditioning states: fully dry, fully saturated and 1% water. Only some material model parameters exhibited a piecewise linear evolution with water content.

7.2 Fibres

The experiments involving single fibres suggested that the E-glass fibres were indifferent to wet environments. However, there was a decrease in the strength of fibre bundles after pure water immersion. Bundles were found to be strain rate dependent on any pre-conditioning state, and wet specimens exhibited lower strengths at all strain rates.

The Weibull parameters for all pre-conditioning environments were found. Also, the development of a novel experimental technique, named *Sound Measurements*, proved its application in fibres. Based on sound acquisition, it allowed the generation of a set of "apparent strengths" to model the bundle behaviour in virtual experiments. Furthermore, frequency analysis of the recorded sound signal found some common frequencies that could be associated with the breaking of single E-glass fibres within a bundle.

7.3 Composites

All tested specimens at tension and short three-point bending exhibited water degradation at all strain rates. Properties affected were the modulus, the tensile strength, and the short beam strength. Water absorbed by the composites is not entirely removable by the post-saturation re-drying. The re-drying process did not recover the tensile strength of the specimens, suggesting permanent damage to matrix and interface.

Resin degradation does not entirely explain all the decrease in properties observed in the composite. This is because there was also degradation in the matrix-fibre interface.

A methodology was also shown to calculate the evolution of the water-induced stresses during the water bath, taking into account simultaneous matrix swelling and relaxation.

Chapter 8

Future research

During this thesis new questions have been raised that can lead to future research directions and original research contributions. This section lists some of them.

In general, there is still a gap at medium strain rates ($1 - 100\,\mathrm{s}^{-1}$) that could potentially be filled with tests in a hydraulic testing apparatus. This would be for mere completeness purposes, as an overall trend with quasi-static and high rate results can already be established.

8.1 Resin

A study into thinner specimens would allow having less heterogeneity across the volume. This would lead to a more accurate evolution law of the material properties with respect to the water content.

The modified Arruda-Boyce model could be expanded with a phenomenological approach to be able to simulate polymer behaviour up to higher strain rates, without the need of more complexity [27]. Another additional modification to the model would be the implementation of damage evolution based on the evolution of parameters with respect to water content.

8.2 Fibres

In the same way quasi-static properties of single fibres were used to model fibre bundles, HR properties of individual fibres could be correlated to the dynamic behaviour of fibre bundles. A campaign with single fibres at a high rate would be challenging but would be beneficial to better model the dynamic behaviour of E-glass fibre bundles. The water immersion time could also be extended to observe the effects of more prolonged exposure to wet environments.

With regards to the sound measurements technique, it would be of interest to explore the ability of the method to count the exact amount of fibres within a bundle. To do so, a new set of experiments could be set up using a smaller number of fibres. Also, the technique should be expanded to provide a set of Weibull parameters corresponding to the tested fibre bundle.

8.3 Composites

Enough experimental data has been generated to build a damage-based model as a function of water content and to explore the onset of failure.

Furthermore, the interface should be investigated further experimentally, as damage in this region was detected. A possible strategy could be a pull-out test to study the interface.

The model of unit cells ignored the effects of uneven and random fibre distribution, as it was simplified in a hexagonal centred unit cell. A statistical distribution of the fibres over a larger unit cell could be set up, with fibre properties that follow Weibull distributions as found in Chapter 5. Hence, the consequences upon the laminates and the expected scatter in tests could be assessed a priori.

References

[1] U. Lindholm, in *Interscience*, edited by R.F. Bunshah (Interscience, 1971), vol. 5, chap. 4, p. Part 1.

[2] J. Zhou and J. P. Lucas, Polymer **40**, 5505 (1999).

[3] G. Z. Xiao, M. Delamar, and M. Shanahan, Journal of Applied Polymer Science **65**, 449 (1997).

[4] G. Alawsi, S. Aldajah, and S. A. Rahmaan, Materials & Design **30**, 2506 (2009).

[5] V. A. Guzman and P. Brøndsted, Journal of Composite Materials **49**, 911 (2015).

[6] E. Gellert and D. Turley, Composites Part A: Applied Science and Manufacturing **30**, 1259 (1999).

[7] L. Bian, J. Xiao, J. Zeng, and S. Xing, Journal of Composite Materials **46**, 3151 (2012).

[8] H. Gu, Materials & Design **29**, 1476 (2008).

[9] B. G. Kumar, R. P. Singh, and T. Nakamura, Journal of Composite Materials **36**, 2713 (2002).

[10] K. B. Mahat, I. Alarifi, A. Alharbi, and R. Asmatulu, Macromolecular Symposia **365**, 157 (2016).

[11] S. A. Grammatikos, R. G. Jones, M. Evernden, and J. R. Correia, Composite Structures **153**, 297 (2016).

[12] T. Shimokawa, H. Katoh, Y. Hamaguchi, S. Sanbongi, H. Mizuno, H. Nakamura, R. Asagumo, and H. Tamura, Journal of Composite Materials **36**, 885 (2002).

[13] G. Quino, A. Pellegrino, V. L. Tagarielli, and N. Petrinic, Composites Part B: Engineering **146**, 213 (2018).

[14] T. Gómez-del Río and J. Rodríguez, Materials & Design **35**, 369 (2012).

[15] T. Gómez-del Río, J. Rodríguez, and R. Pearson, Composites Part B: Engineering **57**, 173 (2014).

[16] T. Gómez-del Río, A. Salazar, and J. Rodríguez, Materials & Design **42**, 301 (2012).

[17] M. F. Omar, H. M. Akil, and Z. A. Ahmad, Materials & Design **32**, 4207 (2011).

[18] R. Gerlach, C. R. Siviour, N. Petrinic, and J. Wiegand, Polymer **49**, 2728 (2008).

[19] D. Mohotti, M. Ali, T. Ngo, J. Lu, and P. Mendis, Materials & Design **53**, 830 (2014).

[20] A. Gilat, R. K. Goldberg, and G. D. Roberts, Journal of Aerospace Engineering **20**, 75 (2007).

[21] K. Hollmann and H. T. Hahn, Polymer Engineering and Science **29**, 523 (1989).

[22] G. Quino, Master's thesis, King Abdullah University of Science and Technology (2013).

[23] W. Chen and B. Zhou, Mechanics of Time-Dependent Materials **2**, 103 (1998).

[24] M. C. Boyce, D. M. Parks, and A. S. Argon, Mechanics of Materials **7**, 15 (1988).

[25] E. M. Arruda and M. C. Boyce, International Journal of Plasticity **9**, 697 (1993).

[26] M. C. Boyce and E. M. Arruda, Polymer Engineering and Science **30**, 1288 (1990).

[27] A. Mulliken and M. Boyce, International Journal of Solids and Structures **43**, 1331 (2006).

[28] J. Lim, J. Q. Zheng, K. Masters, and W. W. Chen, International Journal of Impact Engineering **38**, 219 (2011).

[29] D. R. Drodge, B. Mortimer, C. Holland, and C. R. Siviour, Journal of the Mechanics and Physics of Solids **60**, 1710 (2012).

[30] Y. Arao, N. Taniguchi, T. Nishiwaki, N. Hirayama, and H. Kawada, Journal of Materials Science **47**, 4895 (2012).

[31] N. Taniguchi, Y. Arao, T. Nishiwaki, N. Hirayama, K. Nakamura, and H. Kawada, Advanced Composite Materials **21**, 165 (2012).

[32] X. Yuanming, J. Yuan, and B. Yang, Composites Science and Technology **52**, 499 (1994).

[33] Y. Wang and Y. Xia, Journal of Materials Science Letters **19**, 583 (2000).

[34] D. Zhu, B. Mobasher, J. Erni, S. Bansal, and S. D. Rajan, Composites Part A: Applied Science and Manufacturing **43**, 2021 (2012).

[35] Z. Wang, Y. Xia, and B. Yang, Applied Composite Materials **3**, 89 (1996).

[36] Z. Wang and Y. Xia, Composites Science and Technology **57**, 1599 (1998).

[37] Y. Wang and Y. Xia, Composites Part A: Applied Science and Manufacturing **30**, 1251 (1999).

[38] O. I. Okoli and G. F. Smith, Journal of Reinforced Plastics and Composites **18**, 606 (1999).

[39] O. Okoli and G. Smith, Composite Structures **48**, 157 (2000).

[40] G. H. Staab and A. Gilat, Journal of Composite Materials **29**, 1308 (1995).

[41] J. Harding and L. M. Welsh, Journal of Materials Science **18**, 1810 (1983).

[42] R. Gerlach, C. R. Siviour, J. Wiegand, and N. Petrinic, Mechanics of Advanced Materials and Structures **20**, 505 (2013).

[43] O. Okoli and G. Smith, Journal of Composites Technology and Research **22**, 3 (2000).

[44] S. V. Hayes and D. F. Adams, Journal of testing and evaluation **10**, 61 (1982).

[45] A. E. Armenàkas and C. A. Sciammarella, Experimental Mechanics **13**, 433 (1973).

[46] J. M. Lifshitz, Journal of Composite Materials **10**, 92 (1976).

[47] H. Cui, D. Thomson, A. Pellegrino, J. Wiegand, and N. Petrinic, Composites Science and Technology **135**, 106 (2016).

[48] M. Guden, U. Yildirim, and I. W. Hall, Polymer Testing **23**, 719 (2004).

[49] R. A. Govender, L. a. Louca, A. Pullen, A. S. Fallah, G. N. Nurick, and R. Gerlach, Journal of Composite Materials **46**, 1219 (2011).

[50] X. Fan, S. Lee, and Q. Han, Microelectronics Reliability **49**, 861 (2009).

[51] B. Dewimille and A. Bunsell, Composites **14**, 35 (1983).

[52] M. Arhant, P.-Y. Le Gac, M. Le Gall, C. Burtin, C. Briançon, and P. Davies, Polymer Degradation and Stability **133**, 404 (2016).

[53] G. Xiao and M. Shanahan, Polymer **39**, 3253 (1998).

[54] J. El Yagoubi, G. Lubineau, F. Roger, and J. Verdu, Polymer **53**, 5582 (2012).

[55] A. Apicella, R. Tessieri, and C. de Cataldis, Journal of Membrane Science **18**, 211 (1984).

[56] Y. He, in *2011 IEEE 61st Electronic Components and Technology Conference (ECTC)* (IEEE, 2011), pp. 375–386, ISBN 978-1-61284-497-8.

[57] H. Ardebili and M. Pecht, IEEE Transactions on Components and Packaging Technologies **26**, 206 (2003).

[58] B. De'Nève and M. Shanahan, Polymer **34**, 5099 (1993).

[59] ASTM International, *ASTM D5229, 2012, Standard Test Method for Moisture Absorption Properties and Equilibrium Conditioning of Polymer Matrix Composite Materials* (2012).

[60] C.-H. Shen and G. S. Springer, Journal of Composite Materials **10**, 2 (1976).

[61] I. Merdas, F. Thominette, and J. Verdu, Journal of Applied Polymer Science **77**, 1439 (2000).

[62] D. N. Dang, S. Cohendoz, S. Mallarino, X. Feaugas, and S. Touzain, Journal of Applied Polymer Science **129**, 2451 (2013).

[63] Y. Lin and X. Chen, Polymer **46**, 11994 (2005).

[64] I. Merdas, F. Thominette, A. Tcharkhtchi, and J. Verdu, Composites Science and Technology **62**, 487 (2002).

[65] M. Lai, J. Botsis, J. Cugnoni, and D. Coric, Composites Part A: Applied Science and Manufacturing **43**, 1053 (2012).

[66] P. Scott and J. M. Lees, Journal of Applied Polymer Science **130**, 1898 (2013).

[67] S. M. Wiederhorn and L. H. Bolz, Journal of the American Ceramic Society **53**, 543 (1970).

[68] R. J. Charles, Journal of Applied Physics **29**, 1549 (1958).

[69] N. Cameron, Glass Technology **9**, 14 (1968).

[70] M. L. KorwinEdson, D. A. Hofmann, and P. B. McGinnis, International Journal of Applied Glass Science **3**, 107 (2012).

[71] C. Kurkjian and M. Matthewson, Electronics Letters **32**, 761 (1996).

[72] L. Prian and A. Barkatt, Journal of Materials Science **34**, 3977 (1999).

[73] V. V. Rondinella, M. J. Matthewson, and C. R. Kurkjian, Journal of the American Ceramic Society **77**, 73 (1994).

[74] G. Camino, A. Polishchuk, M. Luda, M. Revellino, R. Blancon, and J. Martinez-Vega, Polymer Degradation and Stability **61**, 53 (1998).

[75] A. Zafar, F. Bertocco, J. Schjødt-Thomsen, and J. Rauhe, Composites Science and Technology **72**, 656 (2012).

[76] K. Liao, C. Schultheisz, and D. Hunston, Composites Part B: Engineering **30**, 485 (1999).

[77] K. Liao, Journal of Materials Science Letters **18**, 763 (1999).

[78] U. Gaur, C. Chou, and B. Miller, Composites **25**, 609 (1994).

[79] H. Wagner and A. Lustiger, Composites **25**, 613 (1994).

[80] A. Kootsookos and A. Mouritz, Composites Science and Technology **64**, 1503 (2004).

[81] D. E. Mouzakis, H. Zoga, and C. Galiotis, Composites Part B: Engineering **39**, 467 (2008).

[82] S. Aldajah, G. Alawsi, and S. A. Rahmaan, Materials & Design **30**, 1835 (2009).

[83] E. Vauthier, J. Abry, T. Bailliez, and A. Chateauminois, Composites Science and Technology **58**, 687 (1998).

[84] V. Pauchard, International Journal of Fatigue **24**, 447 (2002).

[85] E. Woldesenbet, N. Gupta, and J. R. Vinson, Journal of Materials Science **37**, 2693 (2002).

[86] S. Alessi, D. Conduruta, G. Pitarresi, C. Dispenza, and G. Spadaro, Polymer Degradation and Stability **95**, 677 (2010).

[87] G. Quino, J. El Yagoubi, and G. Lubineau, Polymer Degradation and Stability **109**, 319 (2014).

[88] Vuoristo, T. and V.-T. Kuokkala, Experimental Mechanics **44**, 313 (2004).

[89] E. Kontiou, G. Spathis, and C. Kavadias, Journal of Reinforced Plastics and Composites **16**, 306 (1997).

[90] J. Zhou and J. P. Lucas, Polymer **40**, 5513 (1999).

[91] C. Grave, I. McEwan, and R. A. Pethrick, Journal of Applied Polymer Science **69**, 2369 (1998).

[92] S. Sugiman, A. Crocombe, and I. Aschroft, International Journal of Adhesion and Adhesives **40**, 224 (2013).

[93] A. Boubakri, K. Elleuch, N. Guermazi, and H. Ayedi, Materials & Design **30**, 3958 (2009).

[94] P. Le Gac, D. Choqueuse, and D. Melot, Polymer Testing **32**, 1588 (2013).

[95] S. Alessi, D. Conduruta, G. Pitarresi, C. Dispenza, and G. Spadaro, Polymer Degradation and Stability **96**, 642 (2011).

[96] E. L. McKague, J. D. Reynolds, and J. E. Halkias, Journal of Applied Polymer Science **22**, 1643 (1978).

[97] J. El Yagoubi, G. Lubineau, S. Saghir, J. Verdu, and A. Askari, Polymer Degradation and Stability **99**, 146 (2014).

[98] D. A. Gorham, Journal of Physics D: Applied Physics **22**, 1888 (1989).

[99] COMSOL AB, *COMSOL Multiphysics v. 4.4. www.comsol.com* (2013).

[100] ASTM International, *ASTM D618, 2008, Standard Practice for Conditioning Plastics for Testing* (2008).

[101] C. Buckley, J. Harding, J. Hou, C. Ruiz, and A. Trojanowski, Journal of the Mechanics and Physics of Solids **49**, 1517 (2001).

[102] A. Pellegrino, V. Tagarielli, R. Gerlach, and N. Petrinic, International Journal of Impact Engineering **75**, 214 (2015).

[103] S. Iliev, X. Chen, M. Pathan, and V. Tagarielli, Materials Science and Engineering: A **683**, 244 (2017).

[104] R. C. L. Tai and Z. Szklarska-Smialowska, Journal of Materials Science **28**, 6199 (1993).

[105] E. M. Arruda, M. C. Boyce, and R. Jayachandran, Mechanics of Materials **19**, 193 (1995).

[106] M. Boyce and E. Arruda, Polymer Engineering & Science **30** (1990).

[107] C. P. Buckley, P. J. Dooling, J. Harding, and C. Ruiz, Journal of the Mechanics and Physics of Solids **52**, 2355 (2004).

[108] J. Bouvard, D. Francis, M. Tschopp, E. Marin, D. Bammann, and M. Horstemeyer, International Journal of Plasticity **42**, 168 (2013).

[109] J. Wang, Y. Xu, W. Zhang, and Z. Moumni, Materials & Design **97**, 519 (2016).

[110] K. R. Rajagopal, Materials Science and Technology **19**, 1175 (2003).

[111] X. Fan, J. Zhou, and G. Zhang, Microelectronics Reliability **44**, 1967 (2004).

[112] E. M. Arruda and M. C. Boyce, Journal of the Mechanics and Physics of Solids **41**, 389 (1993).

[113] V. Tømmernes, Master's thesis, Norwegian University of Science and Technology (2014).

[114] V. Tømmernes, *Arruda-Boyce VUMAT (Abaqus user subroutine)* (Retrieved from https://daim.idi.ntnu.no/masteroppgaver/011/11935/ on April 2018, 2014).

[115] Dassault Systèmes, *Abaqus version 6.14 (Computer application)* (ABAQUS Inc., 2014).

[116] S. Rabinowitz, I. M. Ward, and J. S. C. Parry, Journal of Materials Science **5**, 29 (1970).

[117] John D'Errico, *fminsearchbnd* (retrieved from: https://uk.mathworks.com/matlabcentral/fileexchange/8277-fminsearchbnd–fminsearchcon, 2006).

[118] J. C. Lagarias, J. A. Reeds, M. H. Wright, and P. E. Wright, SIAM Journal on Optimization **9**, 112 (1998).

[119] A. Boisseau, P. Davies, and F. Thiebaud, Applied Composite Materials **19**, 459 (2012).

[120] R. E. Mould, Journal of the American Ceramic Society **43**, 160 (1960).

[121] C. R. Kurkjian, P. G. Simpkins, and D. Inniss, Journal of the American Ceramic Society **76**, 1106 (1993).

[122] M. J. Matthewson and C. R. Kurkjian, Journal of the American Ceramic Society **71**, 177 (1988).

[123] N. S. E.N. Brown, A.K. Davis, K.D. Jonnalagadda, Composites Science and Technology **65**, 129 (2005).

[124] L. Mišíková, M. Liška, and D. Galusková, Ceramics - Silikaty **51**, 131 (2007).

[125] S. Ito and M. Tomozawa, Journal of the American Ceramic Society **65**, 368 (1982).

[126] S. M. Wiederhorn, T. Fett, G. Rizzi, S. Fünfschilling, M. J. Hoffmann, and J.-P. Guin, Journal of the American Ceramic Society **94**, s196 (2011).

[127] M. R'Mili, N. Godin, and J. Lamon, Physical Review E **85**, 051106 (2012).

[128] Y. Zhou, Y. Wang, Y. Xia, and S. Jeelani, Materials Letters **64**, 246 (2010).

[129] C. Marston, B. Gabbitas, and J. Adams, Journal of Materials Science **32**, 1415 (1997).

[130] V. Calard and J. Lamon, Composites Science and Technology **64**, 701 (2004).

[131] H. N. G. Wadley, C. B. Scruby, and J. H. Speake, International Metals Reviews **25**, 41 (1980).

[132] Caicedo B, Martinez A, and Vallejo L, in *14th Pan-American Conference on Soil Mechanics and Geotechnical Engineering* (Toronto, 2011).

[133] W. Mao and I. Towhata, Applied Acoustics **94**, 39 (2015).

[134] F. Dahmene, S. Yaacoubi, and M. E. Mountassir, Physics Procedia **70**, 599 (2015).

[135] R. Hill and E. Okoroafor, Composites **26**, 699 (1995).

[136] M. R'Mili, M. Moevus, and N. Godin, Composites Science and Technology **68**, 1800 (2008).

[137] E. Maillet, N. Godin, M. R'Mili, P. Reynaud, G. Fantozzi, and J. Lamon, Composites Part A: Applied Science and Manufacturing **57**, 8 (2014).

[138] F. De Cola, G. Quino, K. Dragnevski, and P. Nik, European Journal of Mechanics - A/Solids [Submitted] (2018).

[139] F. T. Wallenberger, J. C. Watson, and L. Hong, ASM Hanbook **21**, 27 (2001).

[140] H. Scholze, Journal of Non-Crystalline Solids **102**, 1 (1988).

[141] ASTM International, *ASTM C1557, 2003, Standard Test Method for Tensile Strength and Young's Modulus of Fibres* (2013).

[142] V. M. Sglavo, E. Mura, D. Milanese, and J. Lousteau, International Journal of Applied Glass Science **5**, 57 (2014).

[143] C. Eberl, R. Thompson, D. Gianola, and S. Bundschuh, *Digital Image Correlation and Tracking version 1.2* (Retrieved from https://uk.mathworks.com/matlabcentral/fileexchange/12413-digital-image-correlation-and-tracking, 2010).

[144] The Audacity Team (2017), *Audacity (R) version 2.1.3 : Free Audio Editor and Recorder (Computer application)* (Retrieved from http://audacityteam.org/, 2017).

[145] Audacityteam, *Audacity: Noise reduction (web reference)* (Retrieved frrom: http://wiki.audacityteam.org/wiki/Noise_Reduction, 2018).

[146] MATLAB, *version 8.6 (R2015b)* (The MathWorks Inc., Natick, Massachusetts, 2015).

[147] MATLAB, *periodogram (Matlab function)* (The MathWorks Inc., Retrieved from: https://uk.mathworks.com/help/signal/ref/periodogram.html, 2018).

[148] B. Boashash, *Time frequency signal analysis and processing : a comprehensive reference* (Academic Press, 2015), ISBN 9780123985255.

[149] MATLAB, *spectrogram (Matlab function)* (The MathWorks Inc., Retrieved from: https://uk.mathworks.com/help/signal/ref/spectrogram.html, 2018).

[150] MATLAB, *Weibull random numbers - wblrnd* (Retrieved frrom: https://uk.mathworks.com/help/stats/wblrnd.html, 2018).

[151] S. K. Garg, V. Svalbonas, and G. A. Gurtman, *Analysis of structural composite materials* (M. Dekker, 1973), ISBN 0824760506.

[152] A. Avena and A. Bunsell, Composites **19**, 355 (1988).

[153] G. Steinbrecher, B. Cohen, and E. Altus, Composites Part A: Applied Science and Manufacturing **84**, 123 (2016).

[154] S. Grammatikos, B. Zafari, M. Evernden, J. Mottram, and J. Mitchels, Polymer Degradation and Stability **121**, 407 (2015).

[155] M. J. Adamson, Journal of Materials Science **15**, 1736 (1980).

[156] K. Derrien and P. Gilormini, International Journal of Solids and Structures **46**, 1547 (2009).

[157] J. E. Shelby, *Introduction to Glass Science and Technology* (Royal Society of Chemistry, 2015), 2nd ed., ISBN 9781782625117.

[158] ASTM International, *ASTM D3039, Standard Test Method for Tensile Properties of Polymer Matrix Composite Materials* (2008).

[159] ASTM International, *ASTM D2344, Standard Test Method for Short-Beam Strength of Polymer Matrix Composite Materials* (2011).

[160] R. T. Brannan, Journal of the American Ceramic Society **36**, 230 (1953).

[161] I. M. Ward and J. Sweeney, *An introduction to the mechanical properties of solid polymers* (Wiley, 2004), 2nd ed., ISBN 9780471496267.

[162] T. Morii, H. Hamada, Z.-i. Maekawa, T. Tanimoto, T. Hirano, K. Kiyosumi, and T. Tsujii, Composites Science and Technology **50**, 373 (1994).